A Novel Method of Sub-milimeter Range Verification for Hadron Therapy using a Tumour Marker

by

Eva Kasanda

A Thesis

Presented to

The University of Guelph

In partial fulfilment of requirements

for the degree of

Doctor of Philosophy

in

Physics

Guelph, Ontario, Canada

ABSTRACT

A Novel Method of Sub-milimeter Range Verification for Hadron Therapy using a Tumour Marker

Eva Kasanda
University of Guelph, 2023

Advisors:
Professor Dr. Carl Svensson

In this work, we present a novel technique for in-vivo proton therapy range verification, and share the results of multiple experiments to determine its feasibility. This technique makes use of a hadron tumour marker (HTM), implanted at a short distance from the clinical treatment volume. Signals emitted from the marker during treatment can provide a direct measurement of the proton beam energy at the marker's position. The method was initially investigated through a Monte Carlo simulation, followed by two experiments at TRIUMF, in which candidate markers were activated with a variety of proton energies. Finally, the method was extended to heavy-ion therapy in an experiment using a ^{16}O beam. In all these investigations, the range uncertainty obtained using the HTM was consistently on a sub-milimeter scale. Range uncertainty in proton and heavy ion therapy limits the prescribed treatment plan for cancer patients with large safety margins and constrains the direction of the beam in relation to any organ at risk. An easy to implement range-verification technique which can be utilized during clinical treatment would allow treatment plans to take full advantage of the sharp fall-off of the Bragg peak without the risk of depositing excessive dose into healthy tissue. This will lead to a better clinical outcome of cancer patients undergoing hadron therapy

Acknowledgements

I would first like to thank Prof. Dr. Dennis Muecher, who initially pitched the topic of this thesis to me in his office as a "crazy idea", and has been a dedicated and enthusiastic advisor throughout my graduate degree, continuing to support me remotely even after moving away.

Second, I would like to thank Dr. Cornelia Hoehr, who was instrumental in the compilation and publication of all the works adapted in this thesis, and who has been incredibly kind and compassionate towards me from the very first time I met her at TRIUMF. Conny, you have gone above and beyond to help me, time and time again, and I will be forever grateful to you.

To Christina: my paper writing, German studying, medical physics researching, hiking, weightlifting, and traveling buddy, and one of the closest friends I've ever had. You were such a big part of this project, and finishing it without you was difficult on many levels, to say the least. You taught me more than you know, and you are sorely missed.

To my parents, Paul and Elke, thank you for always supporting all your children to follow their passions and to chase the things that bring them joy. Your love and your trust has led me down this wonderful path, and I have no regrets.

To Deyvid, my loving partner and best friend of 9 years and counting. Thank you for being there for me and with me in through the ups and downs we've experienced on this journey, and for supporting my ambitions wholeheartedly. I love you very much, and I can't wait to find out what the next chapter has in store for us.

Contents

Abstract **ii**

Acknowledgements **iii**

List of Tables **viii**

List of Figures **ix**

Foreword **1**

1 Introduction **2**

1.1 Proton Therapy 2

1.2 Heavy Ion Therapy 5

1.3 Range Verification 6

1.4 Clinical Range Verification Techniques 7

1.5 Hadron Tumour Marker Range Verification 9

1.6 Hadron Tumour Marker Selection Criteria 10

2 GEANT4 Simulations **14**

2.1 Introduction 14

2.2 Materials and Methods 14

2.2.1 Hadron Tumour Markers . . . 14
2.2.2 Simulation geometry . . . 17
2.2.3 Simulation physics . . . 19
2.2.4 Implementation of proton activation cross sections . . . 21
2.2.5 Beam time structure . . . 21
2.3 Results . . . 22
2.3.1 Impact of offline spectroscopy . . . 22
2.3.2 Dependence of characteristic gamma rays on beam energy . . . 23
2.3.3 Conversion of beam energy to range . . . 25
2.3.4 Range sensitivity . . . 25
2.3.5 Impact of energy and range straggling . . . 28
2.4 Discussion . . . 31
2.4.1 Precision and limitations of technique . . . 31
2.4.2 Proposed clinical application . . . 33
2.5 Conclusion . . . 35

3 First Proof of Principle Experiment with protons 36

3.1 Introduction . . . 36
3.2 Materials and Methods . . . 36
3.2.1 Experimental Setup . . . 38
3.2.2 Peak Fitting Procedure . . . 41
3.2.3 Range Determination . . . 41
3.3 Results . . . 42
3.3.1 Beam Pulsing Technique . . . 42
3.3.2 Off-Beam γ-Ray Spectra . . . 43
3.3.3 γ-Ray Intensity Ratios . . . 43

3.3.4 Half-Life Measurement . . . 44
3.4 Discussion . . . 46
3.4.1 Precision of HTM RV using a Mo Marker . . . 46
3.4.2 Effect of Detector Resolution . . . 48
3.4.3 Effect of Tissue . . . 49
3.4.4 Effect of Range Straggling . . . 51
3.4.5 Comparison to clinical RV methods . . . 52
3.5 Conclusions . . . 53

4 Follow-Up Experiment with protons in a phantom 55

4.1 Introduction . . . 55
4.2 Materials and Methods . . . 56
4.2.1 Hadron Tumour Markers . . . 56
4.2.2 Experimental Setup . . . 57
4.3 Results . . . 62
4.3.1 Data rates . . . 62
4.3.2 Experimental Gamma spectra . . . 64
4.3.3 Background Subtraction and Normalization . . . 64
4.3.4 Peak Fitting . . . 65
4.3.5 Calculation of Peak Ratio . . . 65
4.4 Discussion . . . 69
4.4.1 Range Reconstruction and Sensitivity of Method . . . 69
4.5 Conclusion . . . 72

5 Extension to Heavy-Ion Therapy 73

5.1 Introduction . . . 73

5.2 Materials and Methods . . . 74
5.2.1 Hadron Tumour Marker . . . 74
5.2.2 Experimental Facility . . . 75
5.2.3 Experimental Setup . . . 75
5.3 Results . . . 78
5.3.1 Data rates . . . 78
5.3.2 Experimental spectra . . . 80
5.3.3 Normalization . . . 82
5.4 Discussion . . . 84
5.4.1 Range Verification through Peak Identification . . . 84
5.4.2 Range Verification using intensity of single peak . . . 87
5.4.3 Range verification using ratio of two peaks . . . 89
5.4.4 Impact of realistic marker dimensions . . . 91
5.5 Conclusion . . . 95

6 Outlook of Clinical Translation **96**

7 Summary of Research to Date **102**

Bibliography **105**

List of Tables

2.1 Reference table for modules used in Geant4 simulation 20

3.1 Parameters used for fitting the peaks at 653 keV and 773 keV, respectively. The colors refer to the resulting R_{Mo} lines in Figure 3.6 46

4.1 γ rays of interest originating from interactions between the composite HTM target and the proton beam. 56

4.2 Settings for Range Shifter runs 60

4.3 Settings for PMMA runs 61

4.4 Measured peak ratio for PMMA runs 69

5.1 Summary of γ rays of interest in $^{\mathrm{nat}}$Ag target 74

5.2 Summary of degrader configurations used for individual runs 78

5.3 Summary of normalized and fitted peak areas 84

List of Figures

1.1 Illustration of dose-depth curve for selected modalities of radiation therapy 5

1.2 Diagram illustrating different outcomes during irradiation of an HTM implanted near a tumour. 11

2.1 TALYS cross sections for ^{92}Mo target 15

2.2 Reaction pathways and partial level schemes for reactions of interest in ^{92}Mo 16

2.3 Simulation Geometry 19

2.4 Simulated gamma intensity using a pulsed beam 22

2.5 Simulated γ-ray spectrum illustrating the benefit of measuring delayed γ-rays 24

2.6 Simulated counts of γ-rays of interest and peak ratio, R_{Mo} 26

2.7 Simulation for conversion of proton energy to range 27

2.8 Definition of true beam range in simulation 28

2.9 Simulated sensitivity of HTM RV 29

2.10 R_{Mo} dependence on HTM depth 30

2.11 Proposed clinical application 34

3.1 Reaction channels of interest for ^{92}Mo 38

3.2 Photo of experimental setup 39

3.3 Experimental count rates in a single detector 42

3.4 Experimental $LaBr_3$ γ-ray spectra at various beam energies 44

3.5 Illustration of sample fitting technique 45
3.6 Relationship between R_{Mo} and the average proton energy in the HTM 47
3.7 The sensitivity of R_{Mo} to the beam's range for a single fitting technique. 49
3.8 Uncertainty in the remaining range of the beam as a function of R_{Mo} 50

4.1 PACE cross sections for composite HTM 57
4.2 Sketch of experimental setup at the PIF/NIF facility. 58
4.3 Sketch and photos of composite HTM target 59
4.4 Experimental γ-ray intensity as a function of time 63
4.5 Experimental γ-ray spectrum 64
4.6 Example of fitting procedure for γ-ray peak of interest 66
4.7 Experimental peak areas for RS and PMMA runs 67
4.8 Peak ratios for RS runs 68
4.9 Demonstration of the range reconstruction procedure 70
4.10 Results of range reconstruction compared with the theoretical remaining range of the beam 71

5.1 Sketch of experimental setup in the SEETF vault 76
5.2 Gamma intensity as a function of time 79
5.3 Decay of two peaks of interest as a function of time 80
5.4 Experimental γ spectrum 81
5.5 Comparison of fitted peaks for two neighbouring beam energy settings 83
5.6 Measured neutron flux as a function of time 85
5.7 Experimentally measured cross sections and normalized peak intensities 86
5.8 Calculation of cross sections for reactions of interest in a 50 µm-thick foil of natural silver 87
5.9 Sketch of method for estimating range uncertainty with a single peak. 89

5.10 Uncertainties in range for several assumed uncertainties in peak area. 90

5.11 Peak ratio, R_{Ag} for all Ag+PMMA runs 91

5.12 Calculation of cross sections for reactions of interest in a 1 mm-thick fiducial marker 92

5.13 Illustration of sensitivity limit of range verification method 94

Foreword

The work presented in this thesis covers simulation and experimental work performed in the development of a novel in-vivo range verification method for proton and heavy ion therapy that makes use of a Hadron Tumour Marker (HTM). Much of the material presented in this thesis has been adapted from publications produced by the author within the span of the Ph.D (1; 2; 3; 4), in accordance with the IOP Publishing Author Rights Policy for subscription articles. A decision was made to include within this thesis the contents of a second-author paper(2), as the author of this thesis worked in close collaboration with the primary author, Dr. Christina Burbadge, to prepare, execute, and analyze the work in question. Dr. Burbadge was a close collaborator in much of the work presented here and was awarded a Ph.D in Physics posthumously for her significant contributions to this work.

Chapter 1

Introduction

1.1 Proton Therapy

Despite the steady decline in cancer-related death rates for the past 30 years, cancer remains the leading cause of death in Canada. It accounts for nearly 10 million deaths annually (5), and is the second leading cause of death worldwide (6), affecting nearly 1 in 2 people in their lifetime (7). Approximately 50% of all cancer patients undergo radiation therapy as a part of their treatment (8; 9), often in combination with other methods such as surgery and chemotherapy.

Radiation therapy is a generalized term for cancer treatment techniques which make use of ionizing radiation to destroy or shrink tumour cells without the need for invasive surgeries. The methods in which this radiation can be most optimally delivered are an active area of research and have undergone many improvements over the years (10). Conventional radiation therapy with an external beam, which was first implemented shortly after the discovery of X rays in 1895, makes use of a beam of high energy photons to deposit ionizing radiation directly to the tumour volume (10; 11). This type of radiation refers to particles or electromagnetic waves whose energy is sufficient to result in the ejection of an electron, effectively ionizing atoms and molecules with which they

interact. This ionization is severely damaging to cells, either directly damaging the DNA backbone by breaking crucial hydrogen bonds, or indirectly leading to cell death due to the formation of free radicals which cause cell injury when present in large numbers (10). This damage affects healthy and malignant cells within the patient, but small favourable differences in the damage and repair of healthy cells with respect to malignant ones contribute to the preservation of healthy tissue following treatment. The mechanism of X-ray absorption in the tissue is such that the highest dose from a single treatment beam is delivered near the surface, with an exponential decrease in dose as a function of depth in tissue, as shown in Figure 1.1. Modern radiation therapy techniques make use of a photon gantry which can deliver an X-ray beam from a continuum of angles around the patient, such that the impact of the entrance dose is lessened by distributing it over a large volume of healthy tissue (11). The current clinical gold standard in conventional radiation therapy is called Intensity Modulated Radiation Therapy (IMRT), and makes use of a series of small "pencil" beams delivered from a multi directional photon gantry. The relative weight of each individual pencil beam in its contribution to the total dose delivered is obtained by a computational optimization algorithm based on patient-specific CT data to deliver a uniform dose to the tumour volume while minimizing the dose delivered to surrounding healthy tissue (11). Many research advancements in the field of radiation oncology today are geared towards improving the ratio of the probability of tumour eradication to the probability of normal tissue complication, a quantity referred to as the therapeutic ratio. The vast majority of research in cancer treatments strives to increase this index, either through more effective neutralization of cancer cells, or through the minimization of damage to healthy tissues.

In the past few decades, proton therapy (PT) has gained popularity as a method of radiation therapy because of the advantage it offers in terms of dose distribution compared to conventional radiation therapy (12; 13; 14). While protons and X rays both cause cell damage through ionizing radiation, a proton beam is favourable for several reasons. First, in collisions with other particles,

heavy charged particles experience very little deflection, and travel in an almost linear fashion through matter. This results in a very focused beam, allowing for more precise targeting of tumors. Second, heavy charged particles such as protons have a fundamentally different way of interacting with matter than photons. Photons of a given energy have a probability of being absorbed that is dependent on the composition of the material through which they are traveling. If they are absorbed in an interaction, they deposit all their energy at once. This mechanism is responsible for the exponentially decaying dose profile that they produce within the patient. In contrast, protons gradually lose energy as they travel through a material, primarily through electromagnetic interactions. Unlike X-rays, the proton fluence along the beam path remains mostly constant (15). The probability of electromagnetic interaction increase as the protons slow along their path (15), resulting in the sharp, non-linear increase in dose deposition as the protons approach the end of their track that can be observed in Figure 1.1. The Linear Energy Transfer (LET) of protons also increases rapidly at lower energies, further contributing to cell damage as the protons approach their end point. This region of high dose with a sharp distal falloff is called the Bragg Peak, and is a reflection of the Bethe equation (16). The characteristic dose profile of protons was first suggested for use in the treatment of tumours by Robert Wilson (14), who is often referred to as the "father" of PT. By varying the energy of the proton beam, the depth of the Bragg peak within the patient can be shifted, and large doses of radiation can be administered to a target deep inside the body, with much less radiation damage imparted on surrounding tissues and organs than with conventional photon therapy. In PT, the treatment beam is stopped completely within the patient, and little-to-no dose is deposited distal to the Bragg Peak, making PT a powerful tool for creating conformal plans that avoid dose to organs at risk. With its localized dose deposition, PT has the potential to reduce the dose delivered to healthy tissues and maintain a higher tumour control probability compared to conventional photon treatments(17; 18; 19).

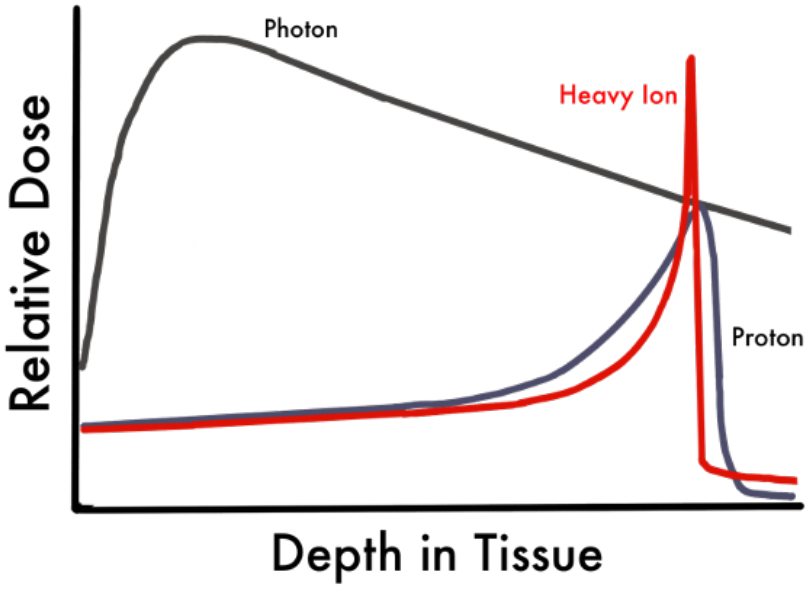

Figure 1.1: Illustration of dose-depth curve for selected modalities of radiation therapy

1.2 Heavy Ion Therapy

The physical advantages of the Bragg Peak are not limited to protons. All heavy charged particles interact through this mechanism and therefore exhibit similar properties. Since the stopping power of ions scales with Z^2 (16), heavier ion beams exhibit a sharper Bragg Peak than lighter ones, as shown in Figure 1.1, as well as a sharper lateral penumbra at greater depths (20). Another feature of the HIT dose profile is the presence of a dose "tail" distal to the Bragg peak. This dose results from fragmentation products that are lighter than the ions in treatment beam traveling beyond the distal penumbra of the Bragg Peak, sometimes exiting the patient entirely. Ions heavier than helium have been shown to exhibit elevated biological effectiveness in the Bragg Peak relative to protons due to their higher LET (20). Heavy-ion therapy (HIT) makes use of these properties in the treatment of certain cancers. The most common treatment beam is ^{12}C, but ^{16}O (21) and ^{4}He (11) have been investigated as well.

1.3 Range Verification

In PT and HIT, since the majority of the dose is deposited in the Bragg peak over the span of a few millimetres, it is crucial that the range of the beam inside the patient is accurately known in order to avoid accidental irradiation of healthy tissue with the Bragg Peak and, consequently, underdosing of the clinical target volume (CTV) (13). Range verification (RV) is an essential tool for characterizing the dose being delivered to the CTV and surrounding tissue during fraction delivery.

Factors such as anatomical changes, organ motion and the uncertainty in converting the CT image data in Hounsfield units (HUs) to tissue stopping power ratios relative to water(22) contribute to an uncertainty in the range of the beam on the order of several millimetres in PT (13). Minimizing these uncertainties remains an active field of study (23). Despite these efforts, to truly exploit the full therapeutic capability of PT and HIT, the range of the beam must be verified in vivo to (24; 12). To account for clinical range uncertainties, current planning target volumes (PTVs) include a safety margin of up to several millimetres, increasing the irradiated volume of healthy tissue in order to avoid underdosing the CTV (12). Range uncertainties in their current state prevent treatment plans from taking full advantage of the distal falloff of the proton beam. Typically, treatment planning optimization algorithms will not consider beam directions that place an organ-at-risk distal to the treatment volume (15). This is because uncertainties in the longitudinal range of the beam are typically larger than uncertainties in the transverse direction. Reducing range uncertainties in PT to the point that the treatment plans can take full advantage of the Bragg Peak will have a significant impact on treatment outcomes, particularly if the range of the beam can be verified in real time.

1.4 Clinical Range Verification Techniques

Without an exit dose to be measured for dose verification purposes, most current RV approaches in PT and HIT rely on the measurement of γ rays produced from proton activation of tissue (25; 23; 26). One of these approaches makes use of β^+-delayed positron annihilation events, which are responsible for the production of 511 keV γ rays in tissue along the beam path (23; 27). These γ rays can be measured with PET detectors to produce a spatial reconstruction of tissue activation induced by the treatment beam (25; 28).

When performed offline, positron emission tomography (PET) RV measurements are taken several minutes after fraction delivery. It has been shown that this time delay can impact the range precision that can be achieved through this method due to the decay of a significant portion of the positron emitters before the PET scan is performed (26). To compensate for this, long acquisition times, typically on the order of 20-30 minutes, are generally required in order to obtain sufficient statistics for accurate range and dose calculation (25). This long time delay leaves room for the blurring effects of biological decay and washout, which are difficult to predict due to the varying perfusion of different tissues (25). Since PET activation is not directly correlated to the dose distribution, to verify the range of the proton beam, the expected dose deposition is often calculated using a Monte Carlo (MC) simulation and compared to the measured PET image to determine the dose fall-off region (26; 23).

Online PET is an alternative RV method in which the PET scanner is located inside the treatment room, incorporated with the proton beam "nozzle" and acquires data during fraction delivery in order to minimize the effects of the time delay present in offline measurements. High background γ rates during fraction delivery and limited angle coverage due to spatial constraints are the main limiting factors of this method (26; 23). Additionally, the spatial resolution of a PET scanner is fundamentally limited by physical effects contributing to an incorrect reconstruction of the PET line of response. Acollinearity of the annihilation γ-rays, positron range in tissue before

an annihilation event occurs, width of the detector element, and penetration of the γ rays into the detector ring are examples of such effects. Careful design of the detector ring can minimize the impact of some of these effects, but the theoretical limit of the spatial resolution for clinical PET scanners is estimated to be 1.83 mm FWHM (29). Typical clinical uncertainties in PET RV are on the order of 3-5 mm (26).

An alternate method of in-vivo RV, which has recently gone into clinical use, is prompt γ-ray (PG) imaging, which makes use of the multitude of prompt characteristic γ rays which are emitted from nuclear interactions between the proton beam and tissue along the beam path (30). Prompt γ radiation from target activation is detected in real time to determine the location of the Bragg peak (31; 32; 33).

The prompt aspect of PG RV reduces the effects of biological washout and signal decay that must be considered in offline PET RV. In addition, the use of characteristic γ rays as opposed to annihilation γ rays minimizes the need to precisely estimate tissue composition (34). Several different imaging configurations have been investigated for PG RV. One basic setup makes use of passive collimation to ensure only γ rays from a small region of the tissue are measured. Due to the high energy (up to 6 MeV) of the γ rays being emitted at high intensities, it is crucial that the collimator is thick enough to sufficiently attenuate γ rays originating from outside the region of interest (34). During treatment, the detector may either be focused on one spatial region, or scan the range of the beam in the patient. The resulting energy and timing distribution of the γ rays produced during treatment is then compared to MC simulations in order to reconstruct the absolute range of the beam in a uniform water-equivalent phantom with an uncertainty of 1.0-1.4 mm (34).

More recently, investigations of actively-collimated PG RV have been making use of a Compton camera, whose position-sensitive detectors are arranged such that the γ-ray angle of incidence can be reconstructed in 3D without the need of a collimator (35). The abundance of γ rays measured by a Compton camera can then be mapped as a function of their origin in the tissue in order to

detect shifts in the range of the proton beam as small as 2 mm (36). This reconstruction is very complex and computationally intensive, and requires high statistics. In addition, the demanding energy, timing, and spatial resolution requirements of the Compton camera detectors make it a costly investment (36). Proton Bragg peak shifts of 2 mm have also recently been measured with PG using a knife-edge slit collimator (33; 32), and statistical uncertainties of 1.1 mm in pencil-beam PT have been measured with a PG RV clinical prototype (37). As with PET, all current PG RV methods rely on comparison to MC simulations for range and dose verification.

An important difference between PT and HIT is the presence of a small exit dose in HIT (depicted in Figure 1.1) that is produced as a result of fragmentation products. This exit dose can be measured and has applications in HIT RV (38).

Current clinical RV techniques all rely on MC simulations to compare against clinical measurements that are indirectly correlated with the beam range (26; 23; 34). These simulations are time-consuming, computationally expensive, require patient CT data, and introduce model-dependency into the range measurement. In both online and offline PET, range uncertainties are typically on the order of several milimeters, and are fundamentally limited in their resolution (29). PG RV has challenging collimation requirements and also yields range uncertainties on the order of milimetres. RV is of particular relevance in FLASH beam delivery (39), in which entire fractions are delivered in a short time frame at very high dose rates.

1.5 Hadron Tumour Marker Range Verification

In the following works, we present the results of the development of a novel technique for PT RV, and its extension to HIT. This technique, hereafter referred to as hadron tumour marker (HTM) RV, involves the implantation of a small, metallic marker, called hadron tumour marker, in the beam path, at a short known distance from the CTV. HTM RV relies on the production of unstable isotopes, from reactions between the HTM and the beam. The cross section for the

production of these isotopes is highly dependent on the energy of the incident beam at the position of the HTM. Consequently, the signal strength for the decay of each of these unstable isotopes is tightly correlated with the remaining range of the beam distal to the HTM. In addition, the unstable isotopes continue to decay some time after the treatment, avoiding the large background of the prompt radiation during treatment. Comparing the signals from multiple reaction channels that are maximized at different energy windows can provide a model-independent indicator of the beam range. By using the ratio of two signals of interest, the need for an absolute measurement is circumvented, making the range measurement independent of beam rate and dose. With an optimal choice of HTM material, HTM RV can be performed in the treatment room, within the time scale of fraction delivery, avoiding the drawbacks of large time-delays and providing near real-time feedback on treatment.

1.6 Hadron Tumour Marker Selection Criteria

We define an HTM to be a small metal marker composed of a material with a favourable response to activation by the treatment beam. Our method takes advantage of the nuclear reactions between the HTM and the proton beam. The produced unstable isotopes emit delayed γ rays whose energy and timing properties are characteristic to the isotope. The yield of the reaction products is heavily dependent on the energy of the incident protons. Due to the non-linear nature of proton stopping powers within the Bragg Peak region, a small, localized HTM marker situated near the distal edge of the treatment field will mostly produce the signal of interest for a small range of beam energies.

By measuring the ratios of the intensities of characteristic γ-ray peaks emitted shortly after proton activation of the HTM, the beam energy at the HTM's position can be determined in real time. Figure 1.2 depicts a schematic diagram of the technique. In principle, one characteristic γ-ray peak is sufficient to determine the beam's energy when used in combination with a calibration of beam intensity, beam energy distribution, γ-ray detection efficiency, dead time of the data

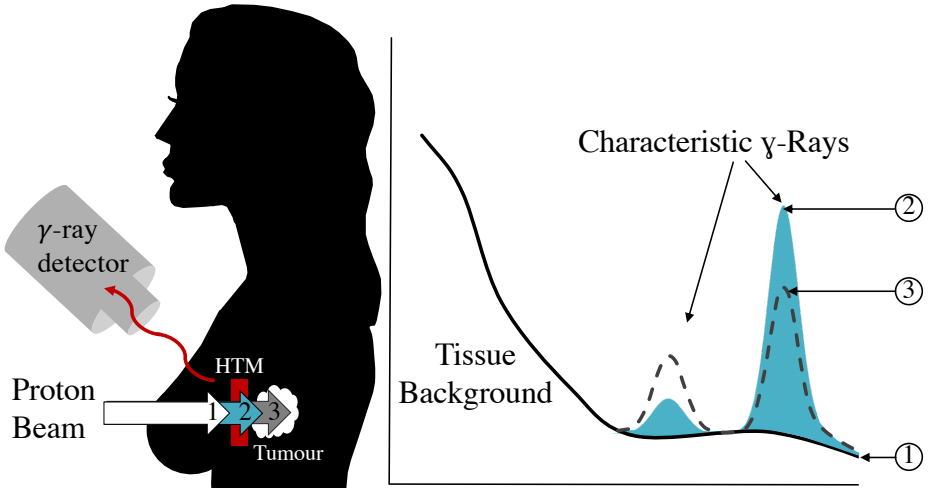

Figure 1.2: Diagram illustrating different outcomes during irradiation of an HTM implanted near a tumour. The HTM is assumed to have two characteristic γ rays originating from different reaction channels. Since the two peaks originate from different reactions, the intensity of each peak will have a different dependency on the proton beam energy at the HTM position. If the proton beam energy is too low (1), only background signal is detected. If the HTM is appropriately irradiated (2), two γ-ray peaks are detected. If the proton beam energy exceeds the intended irradiation energy (3), characteristic peaks are detected, but will have a different relative intensity.

acquisition system, marker thickness and γ-ray absorption in the patient. However, in our method the highest precision of HTM RV is realized by measuring two characteristic γ rays from different reactions on the same HTM, independent of all of the aforementioned absolute measurements.

A candidate material for an HTM must be non-toxic to humans, and must produce a clear and strong signal of interest upon interaction with the Bragg Peak region of the treatment beam, preferably with at least two γ emissions from two different reaction channels with similar signal strength. The cross sections leading to the γ-ray emission need to be maximized at proton energies near the Bragg peak. The γ rays produced from fusion-evaporation reactions are well suited for HTM RV because these reactions generally have cross sections which are maximized near the Bragg peak and fall off quickly as a function of increasing energy (40).

Additionally, the prompt background present during treatment delivery tends to be quite large, but decays very quickly when the beam is stopped. To increase the signal-to-noise ratio (SNR)

of the spectra, measurements should be made off-beam, so the unstable HTM reaction products of interest must have half lives on the order of seconds to minutes to allow most of the prompt background to decay before measurement.

The strength of the signal detected during treatment is impacted by:

- The amount of the isotope of interest within the HTM, either in its natural abundance or in an enriched material, if not too costly,
- the cross section for the reaction of interest in the relevant beam energy range,
- the half-life of the reaction product from which the γ ray of interest originates,
- the energy of the emitted γ rays of interest relative to the sensitive range of the detector, as well as prominent background peaks,
- the γ emission probability following the reaction of interest.

From a clinical perspective the feasibility of using natural materials as markers instead of potentially expensive isotopically enriched ones, as well as biological and long-term radiation toxicity of the marker should be investigated. However, the primary focus of this work is to investigate the feasibility of this method with regard to accuracy and sensitivity. Biological aspects and implantation methods will be discussed in future work. It should be noted that the use and implantation of metallic fiducial markers for tumour localization in proton therapy has been well-established for clinical use (41; 42). The use of hydrogel markers for PET RV has also been previously investigated (43) and could potentially be adapted for the concept discussed here.

The thesis is structured as follows: Chapter 2 presents the results of a Monte Carlo simulation of a treatment scenario for HTM RV, which was used to investigate the feasibility of the technique for the first time. Chapter 3 presents the results of the first proof-of-principle experiment performed with protons at TRIUMF's proton therapy center (PTRC), in which we irradiated

naturally-abundant molybdenum foils at various proton beam energies. Delayed characteristic γ rays were measured with two Compton-shielded $LaBr_3$ scintillators. Chapter 4 presents the results of a follow-up experiment at TRIUMF, in which a composite HTM containing three candidate materials is introduced. The setup of the previous experiment was improved on by using High-Purity Germanium (HPGe) detectors and a PMMA phantom was also used to simulate the γ-ray background from tissue activation. Chapter 5 presents the result of an experiment in which the method of HTM RV was extended to HIT, using ^{nat}Ag as the HTM. Finally, Chapter 6 summarizes the research progress made to date and discusses the outlook of HTM RV in a potential transition to a clinical setting.

Chapter 2

GEANT4 Simulations

2.1 Introduction

This chapter has been adapted from Kasanda et al. (1) in accordance with the IOP Publishing Author Rights Policy for subscription articles.

The work presented in this chapter details the results of the initial simulations and subsequent analysis performed to determine the feasibility of HTM RV, in particular the SNR that can be achieved within a clinical fraction, and the resulting uncertainty in the range measurement.

2.2 Materials and Methods

2.2.1 Hadron Tumour Markers

The marker isotope ^{92}Mo was selected as a HTM candidate due to its potential for emission of intense delayed γ rays after proton activation at beam energies low enough to be near the Bragg peak region, the end of the proton beam range. In case of ^{92}Mo, three different reaction channels are present with cross sections maximized at different but low proton energies. By measuring the

intensity of the emitted γ rays from the different channels, the ratio alone is a measure of the proton beam energy at the position of the marker. In the results section we study to what extent this ratio measurement can be used for RV in PT.

Figure 2.1 shows a plot of the three relevant total reaction cross sections for ^{92}Mo as a function of incident proton energy, obtained using the statistical model code TALYS, version 1.8 (44). The calculations used the Watanabe deuteron optical model potential (OMP) (45), the Koning and Delaroche proton and neutron OMPs (46), the Constant Temperature Matched to the Fermi Gas Model (CT + BSFG) (47) as a nuclear level density model and the Kopecky-Uhl generalized Lorentzian (KU) (48) γ-ray strength function model. Recent cross section measurements of fusion-evaporation reactions undergone by several molybdenum isotopes suggest that the cross section for the ^{92}Mo(p,n)^{92}Tc reaction may be underestimated by up to 30% by TALYS, but that the total cross section for the ^{92}Mo(p,pn)^{91m}Mo and ^{92}Mo(p,pn)^{91}Mo reactions showed good agreement (49).

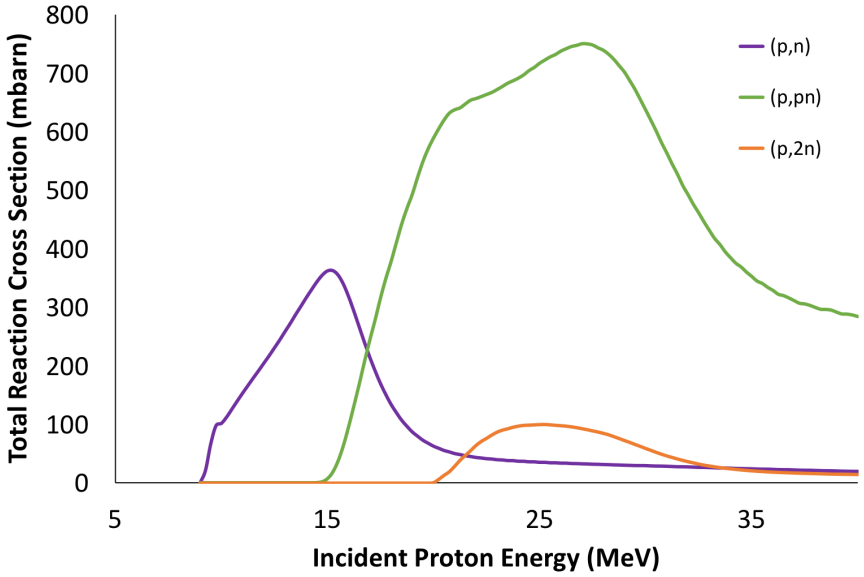

Figure 2.1: Total fusion-evaporation reaction cross sections for ^{92}Mo target as a function of incident proton energy, obtained using the TALYS software (44). For more details, see text.

Figure 2.2 depicts details of the reaction channels. The first reaction, ^{92}Mo(p,n)^{92}Tc, results in the emission of a 773.0(3) keV γ ray through the β-decay of ^{92}Tc with a half life of 4.25(15) minutes

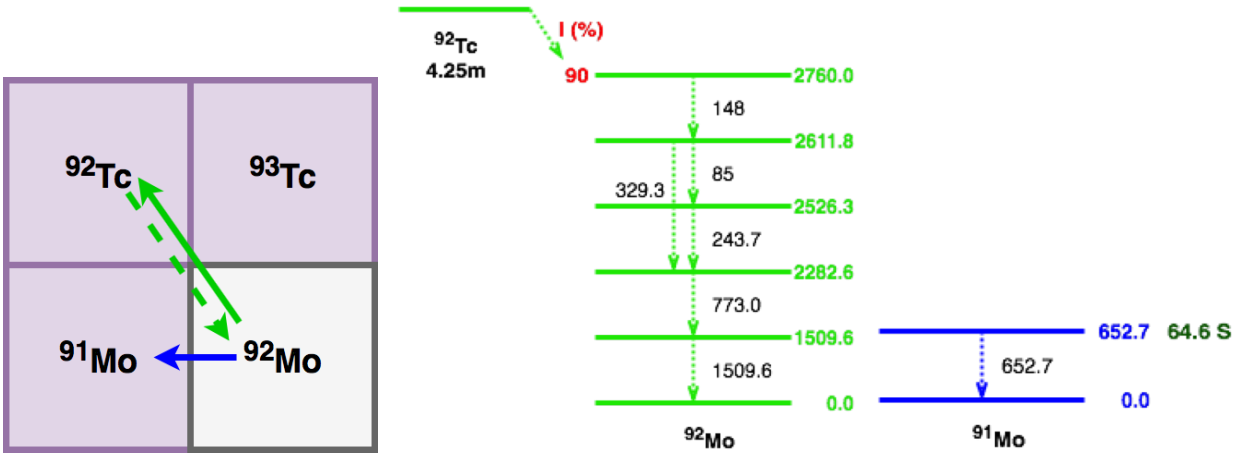

(a) (b) (c)

Figure 2.2: (a) Low-energy reaction pathways from ^{92}Mo proton activation. In green, the ^{92}Mo(p,n)^{92}Tc path is shown with the solid arrow, and the subsequent β-decay into ^{92}Mo is indicated with the dotted arrow. In blue, the (p,pn) path into ^{91}Mo is shown. In (b), a partial level scheme for the decay of ^{92}Tc is shown, indicating the energies of relevant γ rays (black) and levels (green) in keV. The (p,pn) reaction populates an isomeric state of ^{91}Mo, whose partial level scheme is similarly depicted in (c).

(50). The second reaction of interest is ^{92}Mo(p,pn)^{91m}Mo. ^{91}Mo has a low-lying isomeric state that is populated through this reaction, and results in the emission of a 652.9(1) keV γ ray with a half life of 64.6(6) seconds (51). It should be noted that this isomeric state is also populated through β decay following the ^{92}Mo(p,2n)^{91}Tc reaction. However, as the cross section is small (see Figure 2.1) and the contribution to the total γ intensity from this reaction is negligible, it is disregarded going forward. The characteristic γ rays from the first two reactions are suitable indicators of marker activation because they are emitted with high intensity, maximized at different proton activation energies, and the decays responsible for their emission have half lives on the scale of typical fraction delivery times. Consequently, we have chosen molybdenum as a candidate for our study.

Due to the photon-energy dependence of the linear absorption coefficient of tissue, the selection of γ rays with similar energies is favourable for this analysis in order to minimize discrepancies. For a scenario in which the tumour is located deep inside the tissue, literature values (52; 53) suggest that for the same number of emitted 600 keV and 800 keV γ rays passing through 20(1) cm of

soft tissue, a contribution to the uncertainty of 0.85% can be expected in R_{Mo}. This uncertainty is dependent to the depth of the marker inside the tissue and would thus be much smaller for tumours located closer to the surface of the skin.

The clinical feasibility of HTM RV strongly depends on the half lives of the isotopes emitting these γ rays. Due to the high intensity of prompt γ rays present during beam delivery from the irradiation of beam line elements and tissue, the ability to measure the decay of the HTM reaction products after the beam has been switched off is a powerful background-suppression tool. By periodically toggling the beam during treatment in order to measure the signal from the marker once the prompt γ background has subsided, a greatly amplified SNR can be achieved. In addition, one advantage of the much lower γ rates of offline spectroscopy is the possibility of using high purity Germanium (HPGe) detectors, which offer superior energy resolution on the order of 0.2% at 1.173 MeV (54), but experience significant dead times at high rates.

Although using γ spectroscopy for RV has been explored before, the concept of looking at delayed characteristic γ rays from a marker is a new method that has not yet been investigated to our knowledge. Unlike PET and PG RV, the beam energy in the marker measured using HTM RV is model-independent as it does not rely on comparison to MC simulations.

2.2.2 Simulation geometry

In order to determine the feasibility of HTM RV, we make use of GEANT4 (v. 10.02), a C^{++}-based platform for simulating the passage of particles through matter (55). The simulation geometry used in this work is illustrated in Figure 2.3.

The target geometry consists of an outer box, containing a 100 µm-thick marker region. The box is composed of Poly(methyl methacrylate) (PMMA), which is included in the GEANT4 material database as "G4_PLEXIGLASS". PMMA is often used in radiological phantoms because of its similar density, composition, and stopping power to human soft tissue (56). Its purpose in this

simulation geometry is to provide a γ background similar to what would be expected if the marker was located inside the soft tissue of a patient. The marker region is composed of a custom isotope having the nuclear properties of ^{92}Mo (Z = 42, A = 92). A material density of 10.28 g cm^{-3} was used, to approximate the density of naturally-abundant molybdenum. The depth of the marker within the box was selected to be comparable to that of a typical breast tumour (57). The dimensions of the box and marker region were selected to correspond to experimental targets (2). For this experiment, the thickness of the marker region was selected to minimize proton energy loss in the marker, while still providing a strong response relative to the γ background from the PMMA box. 76 MeV protons were generated in vacuum ("G4_Galactic") outside the target as primary events, and given momentum in the direction of the target geometry. This energy was selected such that the protons would be fully stopped inside the target, between the marker region and the far edge of the PMMA box. For the purposes of determining the γ-ray peak intensities produced by the marker with high precision in a low background environment (Section 2.3.2), the geometry was adjusted in select simulations such that the protons impinged directly on a 100 µm-thick ^{92}Mo marker in vacuum (G4_Galactic). For these simulations, the range-dependence of the measured ratio was explored by varying the energy of the generated protons, rather than the depth of the marker within the target. The initial proton energy for these simulations was varied from 8 MeV to 40 MeV in steps of 2 MeV. This geometry is referred to as "low background setup".

To simplify the simulations, a realistic beam energy spread and spatial distribution, as well as detector dimensions, efficiencies and resolutions, were not included in the geometry. Instead, all γ rays are recorded upon exiting the box, and detector resolution is applied during the data analysis using ROOT 6.10.8 (58). In order to reduce computation time, the GEANT4 simulation tracked the instantaneous passage of 10^8 primary protons through the target geometry, recording the energy and timing of all γ rays exiting the box. This can be done as opposed to simulating a larger number of primaries and considering only a small fraction of the simulated data, since γ rays

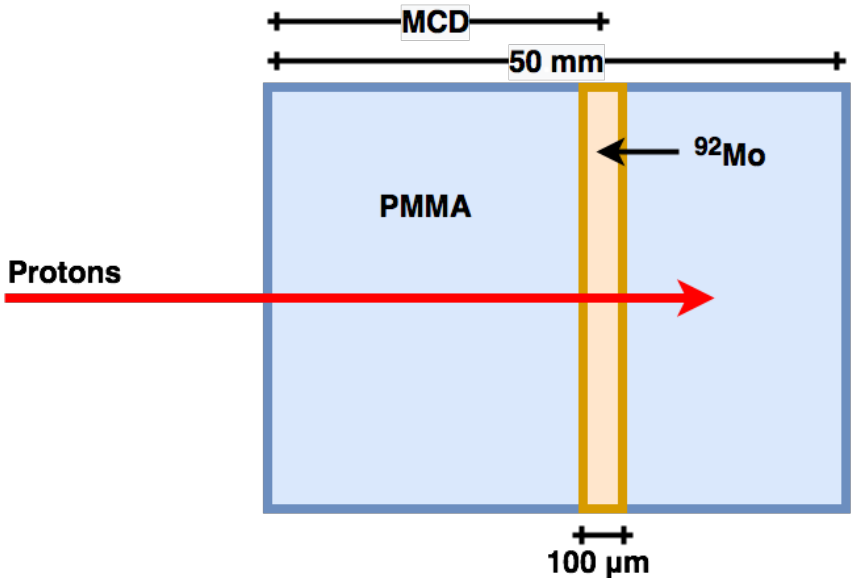

Figure 2.3: Sketch of 2D cross section of 3D simulation geometry. The tissue-equivalent box is indicated in blue, and the marker region is indicated in orange. The primary protons are generated outside the box, in vacuum. Here, the value MCD represents the marker centre depth, which is varied in order to simulate different treatment scenarios.

produced through β-decay are emitted isotropically. In this way, assuming an intrinsic detector efficiency of 10%, and a geometric efficiency of 33%, the number of primaries simulated produces γ-ray statistics that are equivalent to those of a 2.7 Gy fraction dose delivered with a pencil beam.

2.2.3 Simulation physics

A modular physics list was created (see Table 2.1), using QGSP_BIC as a base due to its applicability in the study of primary protons whose energy is below 10 GeV (59). In addition, the G4RadioactiveDecayPhysics constructor was added in order to accurately simulate the decay of long-lived reaction products, and the G4HadronPhysicsQGSP_BIC_AllHP constructor was included for the implementation of TENDL cross sections in the simulation.

Table 2.1: Reference table for modules used in Geant4 simulation (59).

Package	**Description**
QGSP_BIC	QGSP is the basic physics list applying the quark gluon string model for high energy interactions of protons, neutrons, pions, and Kaons and nuclei. The high energy interaction creates an exited nucleus, which is passed to the precompound model modeling the nuclear de-excitation. QGSP_BIC uses the Geant4 Binary cascade for primary protons and neutrons with energies below ∼10GeV, Binary cascade better describes production of secondary particles produced in interactions of protons and neutrons with nuclei.
G4Radioactive DecayPhysics	Constructor for implementation of the radioactive decay process which simulates the decays of radioactive nuclei.
G4HadronPhysics QGSP_BIC_AllHP	Neutrons of 20 MeV and lower use the High Precision neutron models and cross sections to describe elastic and inelastic scattering, capture and fission. For protons and light ions, ParticleHP is used below 200 MeV.
TENDL 1.3.2	TENDL is a nuclear data library which provides the output of the TALYS nuclear model code system for direct use in both basic physics and applications.

2.2.4 Implementation of proton activation cross sections

The calculated proton activation cross sections for the marker from Figure 2.1 are a crucial input, directly affecting the gamma ray yields presented in the results section. We confirmed that our cross section results are consistent with the results from the TENDL 1.3.2 library (44) and imported results from TENDL 1.3.2 into GEANT4; default GEANT4 cross sections are less targeted to the reaction energies of interest compared to TENDL. In addition, the emission rate of the characteristic γ ray of interest from ^{91m}Mo was added artificially into GEANT4 since the simulation physics did not accurately portray the population and decay of the isomeric state. A comparison with recent experimental data (2) suggests that, when a ^{91}Mo nucleus is detected as a reaction product, there is a 10% probability that a γ ray is created with an energy of 652.9 keV, whose emission we randomize with an exponentially distributed time stamp over a half life of 64.6 seconds. The probability for the population of the 652.9 keV isomer is consistent with the results of the aforementioned TALYS calculation, which shows that, at 22.75 MeV, 20.7% of the total (p,pn) reactions result in the production of the isomeric state, ^{91m}Mo. Combining this information with the γ intensities found on NNDC (51), we calculate a maximum emission rate of 10.01(21)% of the 652.9(7) keV γ ray in a (p,pn) reaction. Similarly, the average relative emission rate between 20 MeV and 30 MeV was calculated to be 9.1(13)%.

2.2.5 Beam time structure

In order to simulate pulsed-beam delivery, a beam timing macrostructure was implemented in ROOT, allowing for the periodicity of the beam pulses to be selected post-simulation. Hereafter, γ rays emitted only during the on-beam window ($T_{1/2} \ll 1$ s) are referred to as prompt, while γ rays with half-lives long enough to be detected in the off-beam window ($T_{1/2} > 1$ s) are referred to as delayed.

2.3 Results

2.3.1 Impact of offline spectroscopy

Figure 2.4 shows the simulated γ-ray intensity pattern observed using a periodic beam macrostructure of 5 seconds on-beam, followed by 5 seconds off-beam, at a beam current of 0.75 nA with 10^8 events.

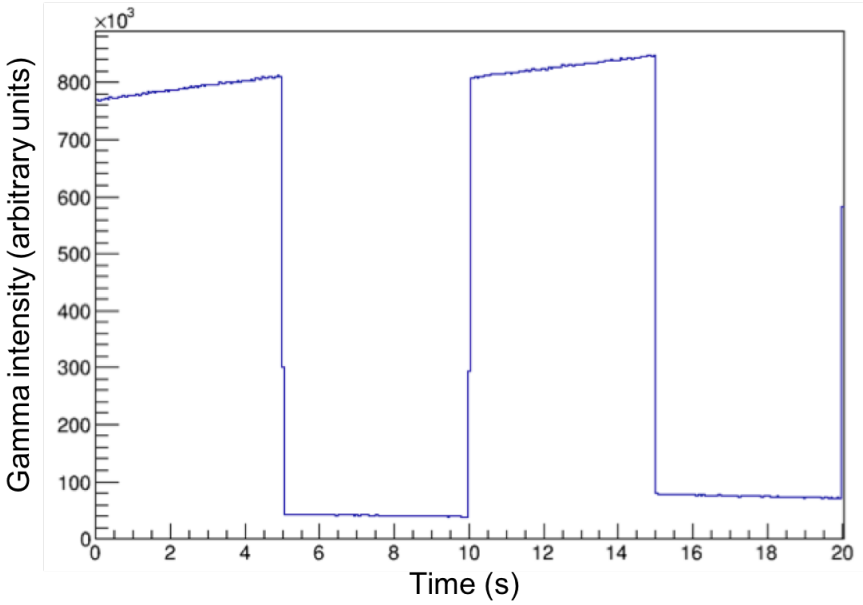

Figure 2.4: Simulation results of γ intensity as a function of time for periodic beam switching at 5 second intervals. This illustrates the immediacy and magnitude of the reduction in background rates.

The majority of the γ-ray and neutron background is produced on-beam. The impact of the background reduction in the off-beam window on the resulting simulated γ spectrum can be seen in Figures 2.5a and 2.5b. Figure 2.5b shows the energy region containing the two peaks of interest for this method: the 773.0 keV γ ray from the decay of ^{92}Tc, and the 652.9 keV γ ray from the decay of ^{91m}Mo. These gamma rays were selected as they have large branching ratios, and are thus emitted at high intensities from the HTM. In addition, the similar energies of these two gamma rays reduces the impact of energy-dependent detector efficiency and tissue absorption on

the measurement accuracy.

The result of the off-beam window is a dramatic decrease in tissue background, and a significant increase in the SNR for the γ rays of interest, at the cost of increased treatment delivery time. For the 773.0 keV γ ray, the SNR in the delayed-only spectrum is improved by a factor of approximately 30 relative to the spectrum in which both prompt and delayed γ rays are included. Following results discuss only γ rays produced in the off-beam window.

We conclude that, by periodically stopping the beam and performing γ-ray spectroscopy off-beam, the SNR of the characteristic peaks can be drastically improved compared to on-beam measurements.

Due to the long rise and decay times of their pulse signals, HPGe detectors are more susceptible to large dead times at high γ-ray rates (above 100kHz) (60). Thus, the reduction in γ-ray count rates achieved by measuring off-beam has the additional advantage of allowing the use of HPGe detectors in future experiments. The simulated data in Figures 2.5a and 2.5b replicates the timing and energy resolution of such a HPGe detector.

2.3.2 Dependence of characteristic gamma rays on beam energy

The simulations for this portion of the analysis used the low background setup described in Section 2.2.2. In this low-background simulation environment, the intensity of the γ rays of interest emitted from the marker were extracted with high precision, with no Gaussian energy smear applied, to produce a calibration curve of γ-ray intensities as a function of proton energies. The γ-ray intensities for the 6652.9 keV and 773.0 keV peaks were plotted in Figure 2.6a as a function of the mean proton energy inside the marker region. Figure 2.6b depicts the same simulation data, but the γ-ray intensity is expressed as a ratio of the peak areas of the 652.9 keV peak to the 773.0 keV peak, R_{Mo}. Expressing the γ-ray intensity as R_{Mo} makes the curve shown in Figure 2.6 independent of dose, beam intensity, and deadtime. The simulation results depicted in Figure 2.6 were obtained

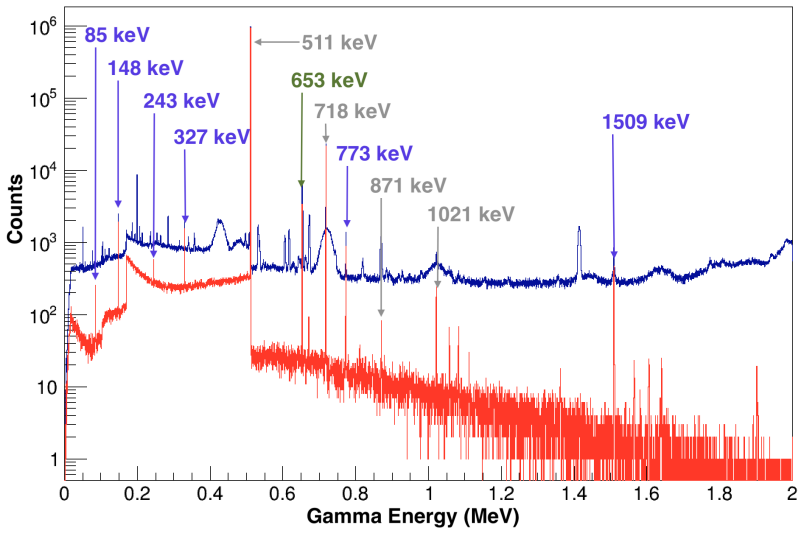

(a)

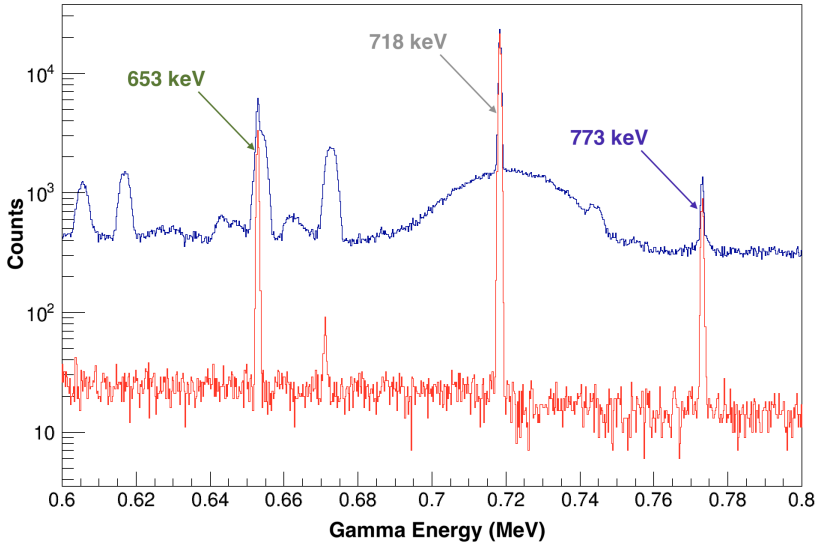

(b)

Figure 2.5: Simulated γ spectrum for 10^8 protons impinging on ^{92}Mo foil embedded in PMMA. The blue histogram shows all γ rays produced, while the red histogram shows only the γ rays produced in the off-beam window. The peaks labelled in violet correspond to the characteristic γ rays produced as a result of the decay of ^{92}Tc, which has a half life of 4.25 minutes, and the peak labelled in green is produced through the γ decay of ^{91m}Mo. The peaks labelled in grey correspond to prominent background peaks from the tissue-equivalent plastic (PMMA). A Gaussian smear replicating an energy resolution of 0.2% was applied to these spectra. (a) Full Spectrum (b) Selected portion of spectrum, focused on the region containing peaks of interest

without any Gaussian smear applied to the time and energy of the γ rays, nor any energy-dependent detector efficiency considerations. However, since the energies of the γ rays of interest are similar, the energy dependence of the detector resolution has a minimal impact on calculations.

2.3.3 Conversion of beam energy to range

In order to relate R_{Mo} to the range of the beam, the relationship between a proton's energy and its remaining range in tissue must be established. For this purpose, we make use of a numerical solution to the velocity profile of protons developed by Martinez et al.(61).

The numerical solution was applied to simulation data depicting depth of a proton in PMMA as a function of its energy at that depth, yielding the plot shown in Figure 2.7a.

The "true remaining range" of the proton beam was determined by plotting the average depth after the HTM centre at which simulated protons come to rest, then extracting the mean by fitting the resulting Gaussian distribution, as shown in Figure 2.8.

2.3.4 Range sensitivity

Simulations of a 76 MeV proton beam impinging on an HTM embedded in PMMA were performed at various marker depths within the plastic in order to characterize the range sensitivity of HTM RV. In all simulations, 10^8 proton events were generated and the reaction products were allowed to decay for 600 seconds. The simulated ratio, R_{Mo}, was compared to Figure 2.7b in order to extract the remaining range of the proton beam in the PMMA. It should be noted that due to the limited range of energies for which a non-zero ratio can be measured, the projection of R_{Mo} alone onto the range axis does not provide a unique solution. However, if the HTM is positioned in the most sensitive region, approximately 4.5 mm from the distal edge of the beam, then a typical treatment precision (26) should be sufficient to avoid any ambiguity in the extracted range for a given R_{Mo}.

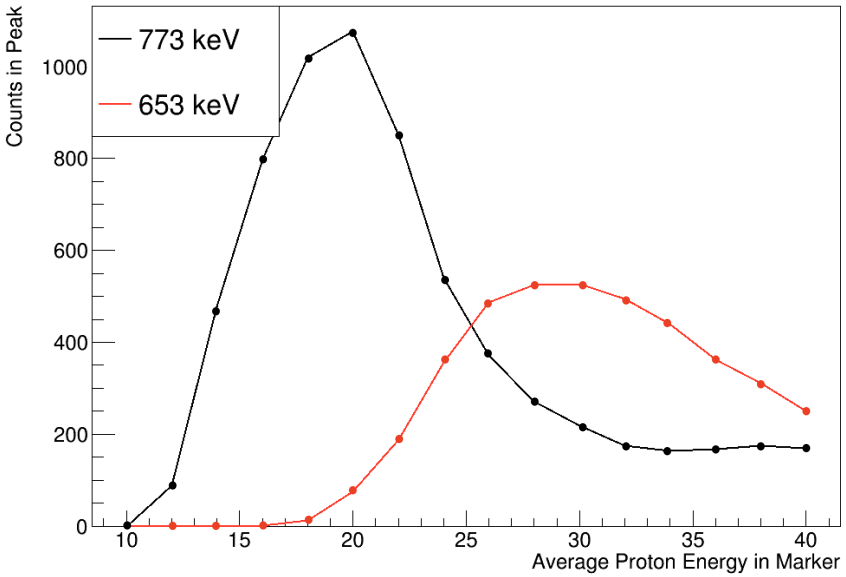

(a)

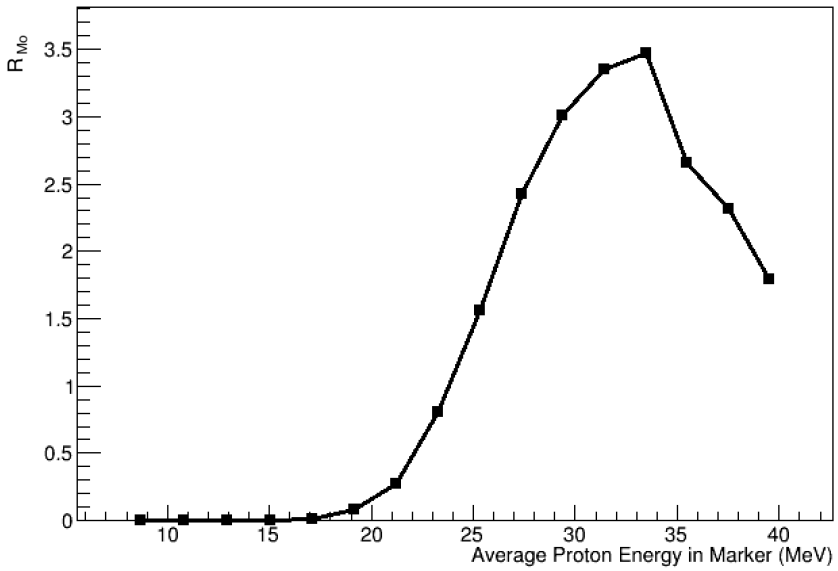

(b)

Figure 2.6: (a) Simulated counts of γ rays of interest (773.0 keV and 652.9 keV) as a function of average proton energy in the marker. (b) Same data, with y-axis expressed as a ratio of the intensity of the 652.9 keV peak to that of the 773.0 keV peak, R_{Mo}. Note that as this data is directly extracted from the simulation, with no realistic energy resolution applied, error bars have not been included.

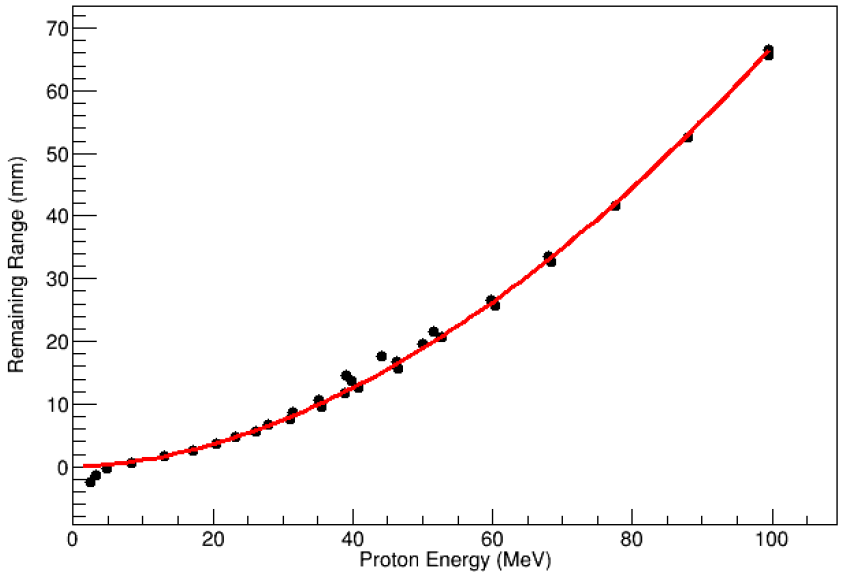

(a)

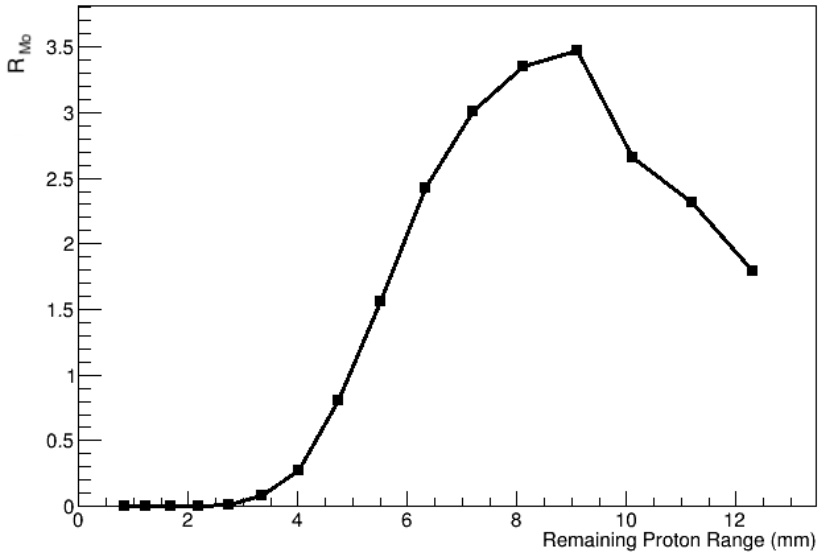

(b)

Figure 2.7: (a) Simulation data of proton depth in tissue as a function of proton energy (markers), fitted with the function developed by (61) (red line). (b) Representation of Figure 2.6b with the x-axis having been converted to remaining range, using the relationship between proton range and energy established in (a).

The extracted remaining range from Figure 2.7b was compared to the true remaining range in Figure 2.9.

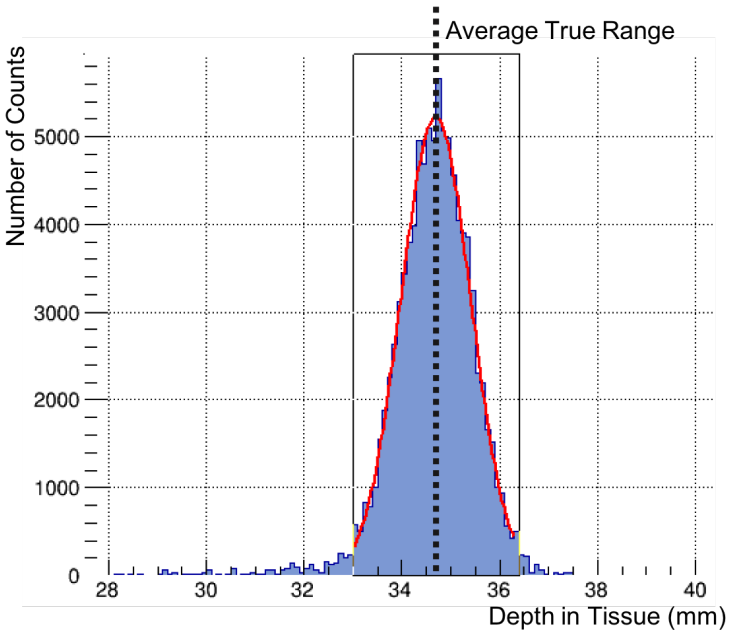

Figure 2.8: Example histogram of depth in PMMA at which 76 MeV protons come to rest. A Gaussian fit was used in order to extract the mean of this distribution.

The data plotted in red show the same results for delivery of only 0.27 Gy instead of 2.7 Gy, with the aforementioned detector efficiencies. The reconstructed range extracted using this method, with a dose of 0.27 Gy, is within 0.05(57) mm of the true range of the beam at the optimal position, and within 0.59 mm on average. The error bar includes contributions from statistical range uncertainty in the ratio from peak fitting, as well as uncertainty in the true range of the beam from straggling. Using a thicker marker would result in improved peak SNR at the cost of a reduced precision in range due to the larger spread of proton energies interacting with the marker.

2.3.5 Impact of energy and range straggling

If the CTV is located deeper inside the tissue, energy straggling effects inherent to PT will result in a wider distribution of proton energies impinging on the HTM, as well as a wider distribution in the range of the beam. In this case, the measured R_{Mo} will depend on a weighted average of the reaction cross sections over the energy distribution of protons interacting with the marker,

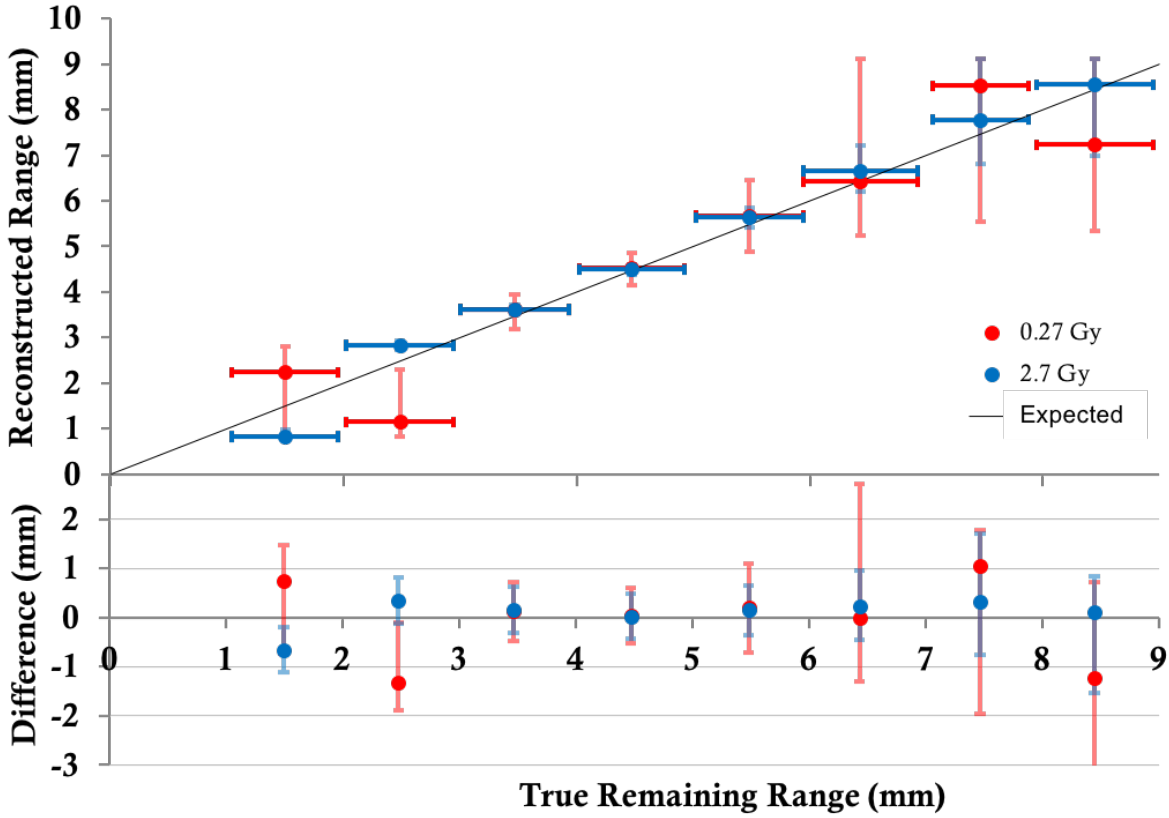

Figure 2.9: (top) Beam range calculated using simulated R_{Mo}, compared to true range of protons after the marker, extracted from simulation data. The straight line indicates the expected value for these data points, i.e. the ideal case in which the true range and extracted range are identical. The horizontal error bars represent the spread in the range of the beam due to straggling. (bottom) Difference between calculated and expected values for proton range. The standard deviations of these data sets from expectations are $\sigma_{2.7Gy} = 0.32\,\mathrm{mm}$, and $\sigma_{0.27Gy} = 0.84\,\mathrm{mm}$.

effectively smoothing out the R_{Mo} curves in Figures 2.6b and 2.7b. This change can be taken into consideration with corresponding calibration curves, as long as the slope of the R_{Mo} curve remains significantly different from zero. Additional simulations were conducted with initial beam energies of 150 MeV and 220 MeV (with an average corresponding HTM depth of 13.0 cm and 25.8 cm, respectively), varying the HTM position about its average value as in Section 2.3.4. A comparison of the measured R_{Mo} for the different HTM positions as a function of remaining beam range for these simulations is illustrated in Figure 2.10.

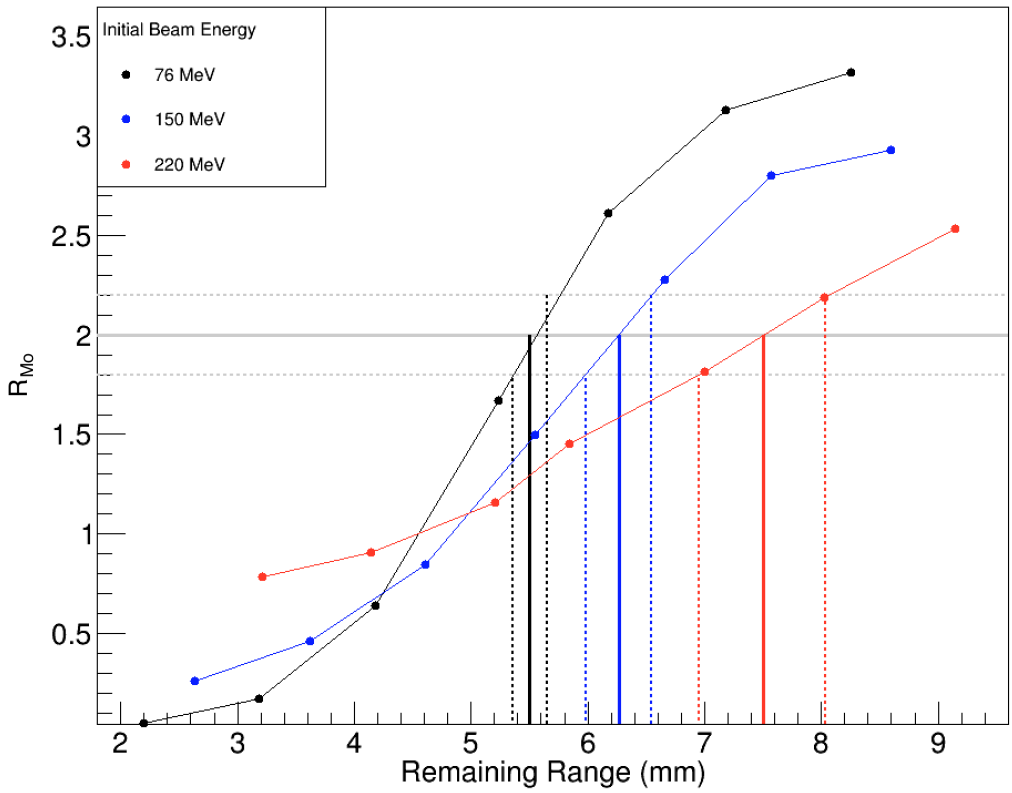

Figure 2.10: Illustration of dependence of peak ratio on HTM depth. Cases for three different initial beam energies are shown. The corresponding average HTM depths for a 76 MeV, 150 MeV, and 220 MeV beam are 35 mm, 130 mm, and 258 mm. The grey lines suppose a ratio of 2.0(2), and the coloured vertical lines indicate the projection of this measured ratio onto the range axis, and the resulting range uncertainty.

Figure 2.10 illustrates how the precision of HTM RV depends on the slope of the ratio calibration. A steeper ratio curve will result in a more dramatic shift in the ratio with a change in remaining beam range. Due to the averaging of the reaction cross sections over the energy range present in the HTM, the precision of HTM RV deteriorates with the depth of the HTM in tissue. Figure 2.10 also shows an approximation of the extracted range uncertainty in these three scenarios, given an assumed R_{Mo} of 2.0(2) (shown in grey). The ratio and its uncertainty are projected onto the range axis in order to estimate the range uncertainty of the method as a function of beam range. This value corresponds to the size of the vertical error bars in Figure 2.9. Due to the averaging of the reaction cross sections, a ratio of 2.0 corresponds to a different remaining range for each case,

indicating that a clinical calibration curve will need to take energy straggling into consideration. A linear fit ($R^2 = 0.99$) of the extracted uncertainty in the three cases as a function of total beam range yields the following range-dependent uncertainty, σ_R,

$$\sigma_R = 62.4\,\mu\text{m} + 0.0018 R_{\text{beam}},$$

where R_{beam} is the average total range of the proton beam. It should be noted that the uncertainty in the extracted range from HTM RV is much smaller than the standard deviation of the beam range due to range straggling. For the three cases shown in Figure 2.10, the initially uniform beams had an average range distribution with standard deviations of 1.5(1) mm, 2.0(1) mm, and 3.0(2) mm, respectively.

2.4 Discussion

2.4.1 Precision and limitations of technique

Our results show that the intensity ratio of the competing reactions of interest, R_{Mo}, is a highly sensitive indicator of average proton energy inside the marker. The R_{Mo} extracted from this method can be directly translated to the beam's range relative to the marker as a form of in-vivo RV in real time, without the need to refer to MC simulations. This method provides an absolute measurement of the residual range of the proton beam relative to the position of the HTM. The use of more than one HTM to provide treatment feedback relative to multiple reference positions is a possibility that will be investigated in future work. The simulation results obtained here suggest that an SNR of up to 38(6) can be achieved for the 773.0 keV peak in the delayed-γ spectrum when measuring with an energy resolution typical for a HPGe detector. It should be noted that the presented simulation does not take into consideration the γ and neutron background in the treatment room, nor the effects of Compton scattering inside the detector crystal.

The simulation results expressed in Figure 2.9 indicate that HTM RV provides a precise reconstruction of the range of the beam in a homogeneous phantom with no offset. As indicated by the two plotted data sets, the range in which this method will offer accurate range verification will be dependent on the SNR that can be achieved clinically. For the setup investigated in this work, the placement of the marker within the tissue that will offer the most sensitive response is approximately 4.5 mm in front of the point at which the beam stops. At this position, and with the statistics used to generate the data points representing the full fraction dose of 2.7 Gy, the marker's response to proton activation will allow for direct measurement of the difference in the beam's range from its target range, up to a difference of 2 mm in either direction. Outside this range, the reduced cross section in one of the two peaks of interest results in larger uncertainties in the reconstructed range.

Our work does not study the influence of tissue inhomogeneities on the precision of our technique. In the case of pencil beams with cross sections of a few millimeters, proper placement of the HTMs should allow beam direction selection such that strong inhomogeneities (like bone-tissue transitions) within the beam path are avoided. This way, an accurate and model-independent measurement of the beam in the marker is achieved. In the case of larger beam diameters, like those used in passive beam modulation, or large inhomogeneities over the cross section of the beam, the measured value for R_{Mo} reflects the integrated cross section of the beam with the marker. If, for example, part of the beam's energy is strongly reduced at the position of the marker due to the influence of bone, that part of the beam will not contribute to the γ-ray yield of the HTM. Although at this point our method loses the advantage of being model-independent, the comparison of the measured "effective" R_{Mo} to simulations based on the treatment plan will yield valuable information, highly sensitive to the beam's range and the tissue inhomogeneities for the actual setting. This important aspect will be studied in more detail based on simulations and measurements with more complex phantoms in future studies.

Since typical clinical range precision is generally under 2 mm, the application of HTM RV in the region of highest sensitivity can provide a unique measurement of the beam's range, with no degeneracy within the range of beam energies expected. In addition, the reduction in beam energy induced by the passage of the proton beam through a 100 µm HTM is minimal and can be well characterized to reduce impact on fraction delivery. The nature and severity of any additional beam perturbations caused by the localized HTM must be evaluated, but is beyond the scope of this work. The impact of CT artifacts and dose shadowing due to fiducial markers clinically employed in PT treatment planning is being investigated for various markers (62; 63; 64; 41; 65; 66).

In general, PT fractions are delivered with a range of beam energies to ensure full coverage of the CTV. The range reconstruction is dependent on the energy spread of the proton beam at the position of the marker, as discussed in Section 2.3.5. Therefore our method is best suited for shallow tumours treated with pencil-beam PT, where the beam energy is well defined and can be varied over the course of the fraction delivery.

2.4.2 Proposed clinical application

The results of the 0.27 Gy simulation suggest that our method could be used prior to fraction delivery as a method of quality control, as well as during treatment for online monitoring. The HTM would be surgically implanted near the CTV before treatment (67). The position of the implanted HTM inside the tissue can be precisely measured prior to treatment with a CT scan. Using a small portion of the dose delivered with a mono-energetic beam, the RV method outlined in this work can provide a high-precision measurement of the proton energy in the HTM before delivering the remainder of the fraction. Figure 2.11 illustrates this clinical application of HTM RV in three different treatment scenarios. If the range of the beam is different from expectations based on the treatment plan, the measured ratio will indicate this, allowing for adjustments to be made before delivery of the full dose.

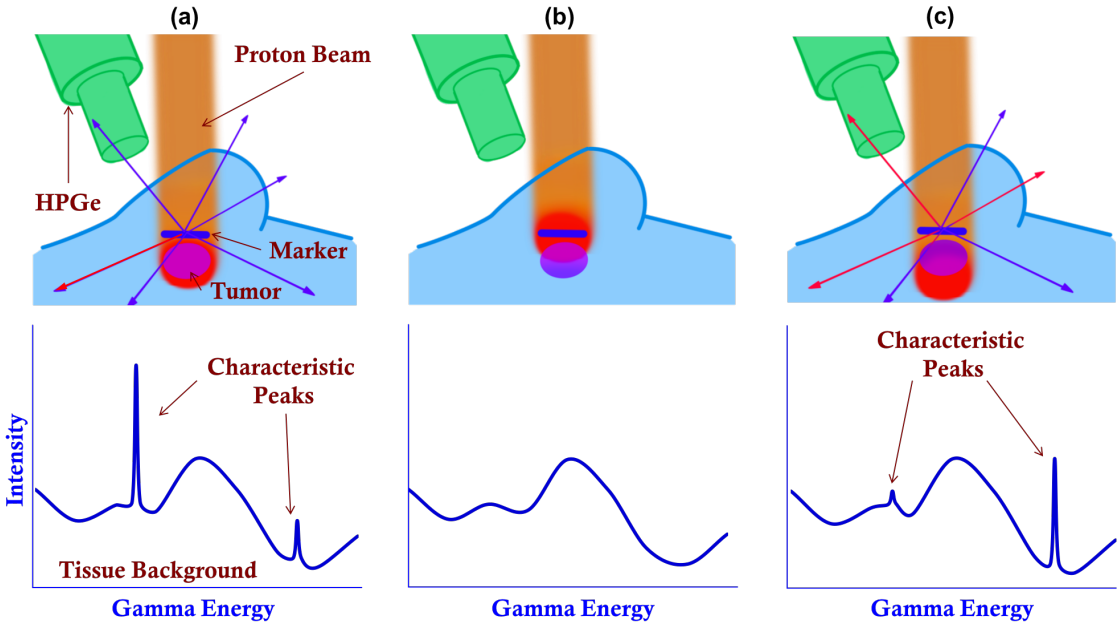

Figure 2.11: Illustration of proton dose profile and corresponding γ spectrum achieved in (a) an ideal treatment scenario, (b) a treatment scenario in which the beam falls short of the expected range, such that no γ-ray line is observed as the proton energy incident on the HTM is below the threshold for fusion-evaporation reactions, and (c) a treatment scenario in which the the beam stops beyond the expected range, such that a different ratio of the two characteristic γ lines is observed.

Thereafter, the signal from the HTM will continue to provide real-time range feedback for the remainder of the fraction delivery. The beam pulsing technique utilized in obtaining the R_{Mo} measurement allows for a signal enhancement of over an order of magnitude at the cost of an extension of the fraction delivery duration. However, in specific cases such as the radiological treatment of breast cancers, the timing of the fraction delivery may already be limited by the patient's breathing cycle, allowing for the implementation of HTM RV with minimal impact on delivery times. The prompt background at typical treatment beam intensities does not decay fast enough for event separation by synchronization with the beam microstructure. Therefore, this method of treatment delivery requires the implementation of a beam macrostructure at the treatment facility. Additionally, it is worth noting that PET RV can provide three-dimensional information on the beam path within the patient, while HTM RV is limited to a high-precision

measurement of the residual range of the beam relative to the HTM position. The two techniques could be used in conjunction in order to gain the benefits of both.

2.5 Conclusion

The in-vivo RV method outlined in this chapter is able to determine in silica the absolute remaining range of the beam inside the patient on a sub-mm scale, without the need for comparison to complex MC simulations, and is largely independent of tissue composition. The energy of the beam in the HTM is directly measured through the peak intensity ratio, R_{Mo}, and the remaining sub-cm range of the beam is calculated with a very small uncertainty, on the order of $62.4\,\mu\mathrm{m} + 0.0018 R_{\mathrm{beam}}$, where R_{beam} is the total range of the beam. With a simple and relatively cost-effective measurement setup consisting of a small γ-ray detector array and a digital data acquisition system, this method is highly accessible for clinical use. With acquisition times much shorter than PET, and range measurements taking place prior to the completion of fraction delivery, this method is able to provide feedback on treatment accuracy in real time, on a sub-mm scale, without the need for comparison to MC simulations.

Chapter 3

First Proof of Principle Experiment with protons

3.1 Introduction

This chapter has been adapted from Burbadge et al. (2) in accordance with the IOP Publishing Author Rights Policy for subscription articles.

The work presented in this chapter experimentally demonstrates the feasibility of a new method to measure the remaining range of a proton beam after it passes through an HTM (1).

3.2 Materials and Methods

For our first proof-of-principle experiment, molybdenum was chosen as an HTM material, because it was shown by simulations (see Chapter 2) to be well suited for our RV technique (1). ^{nat}Mo has a high (p, xn) reaction cross section to Tc isotopes, on the order of 100 mb for clinical proton beam energies (68; 69; 70; 71; 72). As the ^{92}Mo isotope has a high natural abundance of 14.53(30)

% (73), and it is the only Mo isotope that has the potential to emit strong delayed characteristic γ rays, enriched Mo is not required. In addition, reaction products from proton activation of ^{92}Mo have half lives which are short enough to be measured between beam pulses in a clinical time frame.

The majority of the delayed γ radiation of interest originates from four fusion-evaporation reactions on the ^{92}Mo nucleus, populating the ground state and isomeric state in ^{91}Tc and ^{91}Mo, respectively. The decay modes and emitted radiation from these reactions are illustrated in Figure 3.1. Meta-stable isomeric states are denoted by a superscript "m". The expected relevant populated states and their γ-ray emissions after proton activation of ^{92}Mo are:

1. The ^{92}Mo(p,pn)^{91m}Mo is expected to be populated with approximately 10% of the (p,pn) cross section strength in the energy range of the Bragg peak, according to calculations using the optical model reaction code TALYS (1). The isomer emits a 653 keV γ ray with an intensity of $I = 48.2(21)\%$ and half life of $t_{1/2} = 64.6(6)$ s (51). This reaction is illustrated in Figure 3.1a.

2. The ^{92}Mo(p,2n)^{91}Tc reaction may populate the ground state of ^{91}Tc, which will β decay to ^{91m}Mo with a branching ratio of 0.69% and half life of $t_{1/2} = 3.14(2)$ min, emitting a 653 keV γ ray with $I = 48.2(21)\%$ (51). This reaction is illustrated in Figure 3.1b.

3. The ^{92}Mo(p,2n)^{91m}Tc reaction may also populate ^{91m}Tc which lies at an energy of 139.3(3) keV (51). ^{91m}Tc will β decay to ^{91m}Mo with $t_{1/2} = 3.3(1)$ min by a 43% branch, emitting a 653 keV γ ray with $I = 48.2(21)\%$ (51). Higher energy states of ^{91}Tc populated by the ^{92}Mo(p,2n)^{91m}Tc reaction may also feed into the ^{91m}Tc state, resulting in additional emissions of the 653 keV γ ray.

4. Finally, the ^{92}Mo(p,n)^{92}Tc reaction populates the ground state of ^{92}Tc, which subsequently β decays into ^{92}Mo with $t_{1/2} = 4.25(15)$ min. The excited state of ^{92}Mo then decays by emission of a 148.0(6), 243.7(6), 329.3(3), 773.0(3) or 1509.6(3) keV γ ray, emitted with intensities of

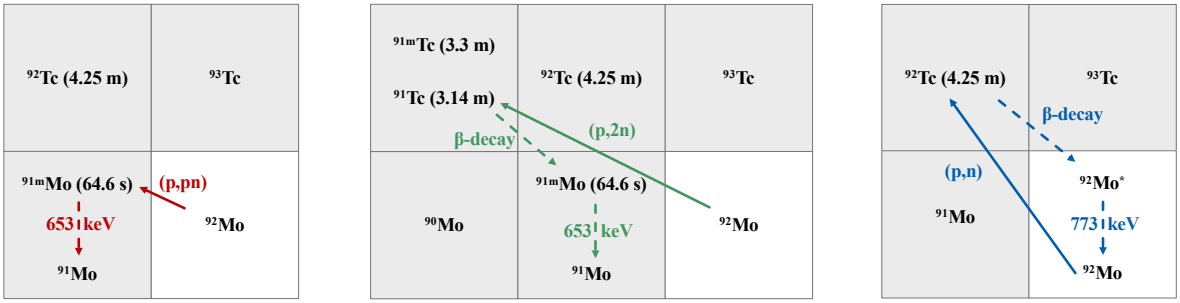

(a) (b) (c)

Figure 3.1: Reaction channels with high cross sections and strong delayed γ radiation from the proton irradiation of a ^{92}Mo target at energies near the Bragg peak include: (a) The $^{92}\mathrm{Mo}(p,pn)^{91\mathrm{m}}\mathrm{Mo}$ reaction (red), which can decay via the emission of a 653 keV γ ray. (b) The $^{92}\mathrm{Mo}(p,2n)^{91}\mathrm{Tc}$ reaction (green) and $^{92}\mathrm{Mo}(p,2n)^{91\mathrm{m}}\mathrm{Tc}$ reaction (not illustrated), which can both β decay into $^{91\mathrm{m}}$Mo, which subsequently decays by emission of a 653 keV γ ray. (c) The $^{92}\mathrm{Mo}(p,n)^{92}\mathrm{Tc}$ reaction (blue), which β decays into an excited state of ^{92}Mo. This state can decay by emitting a 773 keV γ ray.

$I = 71(4)\%$, $I = 13.3(5)\%$, $I = 80(3)\%$, $I = 99.857\%$, and $I = 101(3)\%$, respectively (50).

An example (p,n) reaction is illustrated in Figure 3.1c.

While the three first reaction pathways will all have subsequent decays emitting an indistinguishable 652.9(1) keV γ ray, it is not necessary to discern the origin of this γ ray in HTM RV, as only the resulting γ-ray yield as a function of proton energy is needed.

The 653 keV and 773 keV γ rays are ideal candidates for HTM RV, as they are both emitted with high intensity and are close in energy, so they have a similar relative detection efficiency and absoption coefficient. The ratio of characteristic 653 keV/773 keV γ-ray strength will henceforth be referred to as the quantity R_{Mo}.

3.2.1 Experimental Setup

Proton Therapy Facility at TRIUMF

To determine the feasibility of the HTM RV technique, an experiment was performed at the TRIUMF 500 MeV cyclotron (74) at the PT facility at beamline 2C1, which is specialized to treat

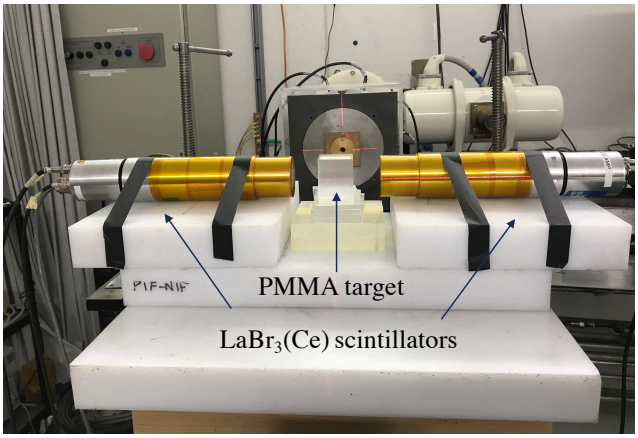

Figure 3.2: Two $LaBr_3$ scintillators were placed inside Compton shields (not shown) surrounded by Mu-Metal foil (not shown) to improve the signal-to-noise ratio of the spectra. A PMMA phantom, measuring 5 x 5 x 5 cm^3, is placed in the beam's isocentre in the picture to indicate target position.

patients with ocular melanomas (67). A 70 MeV proton beam was extracted from the cyclotron with an intensity of 2 nA. In order to ensure a uniform intensity distribution of the beam, it was first dispersed through a 0.8 mm lead disk. The beam then passed through a collimator, whose shape was a square with rounded corners, such that the beam measured approximately 3 x 3 cm^2 in the isocentre. The energy of the beam in the isocentre downstream of the beamline components was determined by previous beamline calibrations to be 63 MeV. As this energy can be too high to treat shallow tumours, the energy of the proton beam was further decreased to a clinical value with a range shifter, which places 0 to 40 mm of poly(methyl methacrylate) (PMMA) in the path of the beam to reduce its energy (75). Boronated paraffin was placed downstream to shield the detector from neutrons, mostly produced by the irradiation of the collimator and lead disk.

Data was acquired at four range shifter settings in order to characterize the energy sensitivity of HTM RV. The settings were selected to include values at which an energy calibration of the range shifter had been performed. The calibration, which has been confirmed with measurements in a water phantom, uses SRIM (76) to simulate the beam's energy downstream of the range shifter assuming an incident beam energy spread of 1 MeV. The proton beam energies in the isocentre are,

with their respective standard deviations, 13.7(19), 20.7(14), 23.3(13) and 27.1(12) MeV. Of these, the 23.3 MeV setting was the only one at which a verified calibration had not been performed. The energy was interpolated using a quadratic fit of calibration data between 13 and 35.5 MeV and its uncertainty calculated by linearly interpolating between the uncertainties of the two adjacent calibrated points.

The beam was then impinged on a 100 µm-thick natural Mo foil target in the isocenter, measuring 2 x 2 cm^2 mounted in air. Two Compton-suppressed $LaBr_3$(5% Ce) scintillators were placed perpendicular to the beam axis, surrounding the target, as is shown in Figure 3.2. Saint-Gobain BrilLanCe 380 $LaBr_3$ scintillators were selected for this experiment due to their high intrinsic efficiency, cost efficiency relative to higher resolution detectors such as HPGe, and radiation hardness, while also offering an off-beam energy resolution of 4.4(4)% at 773 keV. The scintillators were placed inside two bismuth germanate (BGO) Compton-suppression shields to reduce the background from Compton scattering. These Compton-suppression shields were then wrapped in Mu-Metal in order to shield the scintillators' photomultiplier tubes against the magnetic field of the main cyclotron.

Pulsed Beam Delivery

This experiment also took advantage of a pulsed beam. While the beam is on, high radiation background is emitted from the proton activation of the beam line components, collimator and the phantom or patient. Data was collected in short on-beam and off-beam windows in order to increase the SNR of delayed spectroscopic peaks of interest. To create on-beam and off-beam windows of five minutes each, the transmission of the beam into the treatment room was manually controlled. This was accomplished using a pneumatically actuated beam stop, located upstream of the treatment room, allowing for prompt interruption of beam delivery during patient treatment.

Data Acquisition System

A new data acquisition system (DAQ) was developed for this experiment which consisted of a CAEN DT5730 14-bit digitizer, which can operate at 500 MS s^{-1} using a custom frontend integrated with the MIDAS DAQ (77) with pulse shape discrimination firmware. The initial unpacking of the raw data to analysis histograms was performed with GRSISort (version 4.0.0.0) (78), a C^{++}-based sorting code developed by the TIGRESS & GRIFFIN collaboration at TRIUMF. In conjunction to GRSISort, Tv (version 1.9.13) (79), and ROOT (version 6.14/04) (58) were used in the offline analysis.

3.2.2 Peak Fitting Procedure

R_{Mo} values were determined by fitting the 653 keV and 773 keV peaks and taking the ratio between their areas. The fits were performed with Tv by fitting a Gaussian peak on a linear background. However, due to the limited resolution of the spectra, there was a significant uncertainty associated with the choice of fitting technique. As such, multiple fitting techniques were employed, described in more detail in section 3.3.3. Since the variance in R_{Mo} due to the choice in fitting procedure was much larger than the error bars for R_{Mo} in individual fits, this method allowed for a more accurate representation of the total uncertainty associated with R_{Mo}. Although there was no significant difference in the spectra from both detectors in the region of interest, the spectra were analyzed individually in order to check the consistency of our method.

3.2.3 Range Determination

A simulation was performed with SRIM-2013 in order to relate the energy of a proton beam to its range by simulating a 63 MeV proton beam of 10,000 primary protons impinging on 35 mm of PMMA, with a density of 1.17 g cm^{-3}. PMMA was selected as it has a similar elemental composition as human tissue and is often used as a tissue-equivalent plastic in phantoms. The

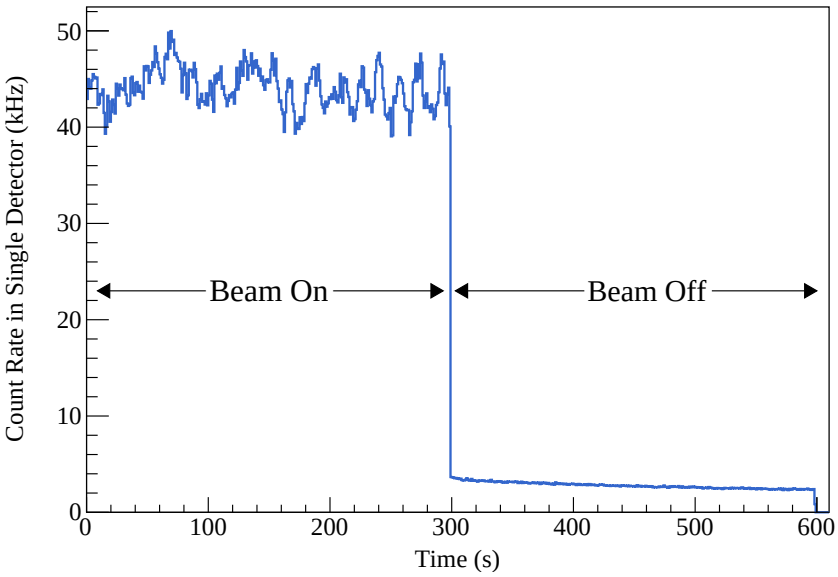

Figure 3.3: The beam pulsing structure for the irradiation of Mo at a beam energy of 20.7 MeV illustrates the significant reduction of the number of counts from prompt radiation background in the off-beam window. The fluctuations in the count rates are due to small changes in beam intensity.

range of the beam in PMMA was plotted as a function of beam energy and was fitted using a solution to the Bethe formula for clinical PT energies developed by Martinez et al(61). Once the range calibration is applied, a measurement of R_{Mo} can be directly related to the beam's residual range in PMMA.

3.3 Results

3.3.1 Beam Pulsing Technique

By using the beam pulsing technique described in Section 3.2.1, the average count rates from the irradiation of the Mo foil at 20.7 MeV were instantaneously reduced from 44 kHz in the on-beam window to 3.6 kHz in the off-beam window, as shown in Figure 3.3. To take advantage of the decrease in background radiation, only the off-beam spectroscopic data was analyzed.

3.3.2 Off-Beam γ-Ray Spectra

The off-beam spectra from a single detector are shown in Figure 3.4. Several characteristic γ rays were observed that are consistent with the reaction products from activation of the Mo foil. Notably, the cross sections of the 148.0, 243.7, 329.3, 773.0 and 1509.6 keV peaks from the (p, n) reaction were maximized at 13.7 MeV and decreased as a function of beam energy, while the cross section of the 652.9(1) keV peak from the (p, pn) or $(p, 2n)$ reaction was maximized at 27.1 MeV. These results are consistent with TALYS calculations (1).

The off-beam Mo spectrum at 20.7 MeV showing only the region from 600 to 900 keV is shown in Figure 3.5 to demonstrate the resolution of the spectra in the region of interest and motivate the need for various peak fitting techniques, as described in Section 3.2.2.

3.3.3 γ-Ray Intensity Ratios

The R_{Mo} values obtained using various fitting methods described in Section 3.2.2 are plotted with different colours in Figure 3.6. There were two primary fitting techniques which both used a Gaussian peak shape. In the first technique, the peak at 653 keV is treated as a doublet together with a weak unidentified line around 700 keV, whereas the peak at 773 keV is treated as a triplet together with two identified lines which form the broad peak around 850 keV. In this method, the peaks were either allowed to vary in width (indicated by the black line (detector 1) and red line (detector 2) in Figure 3.6) or the peak width was fixed (indicated by orange line (detector 1) and green line (detector 2) in Figure 3.6). In the second technique, the five aforementioned peaks were treated as a quintuplet of peaks, as indicated by the blue line (detector 1) and violet line (detector 2) in Figure 3.6. All fits were performed using a linear background as higher order polynomials were not able to consistently describe the shape of the background spectrum over the entire energy range (see Table 3.1 for details). Regardless of the fitting technique, R_{Mo} has a characteristic slope as a function of beam energy, hence allowing measured values of R_{Mo} to be related to the effective

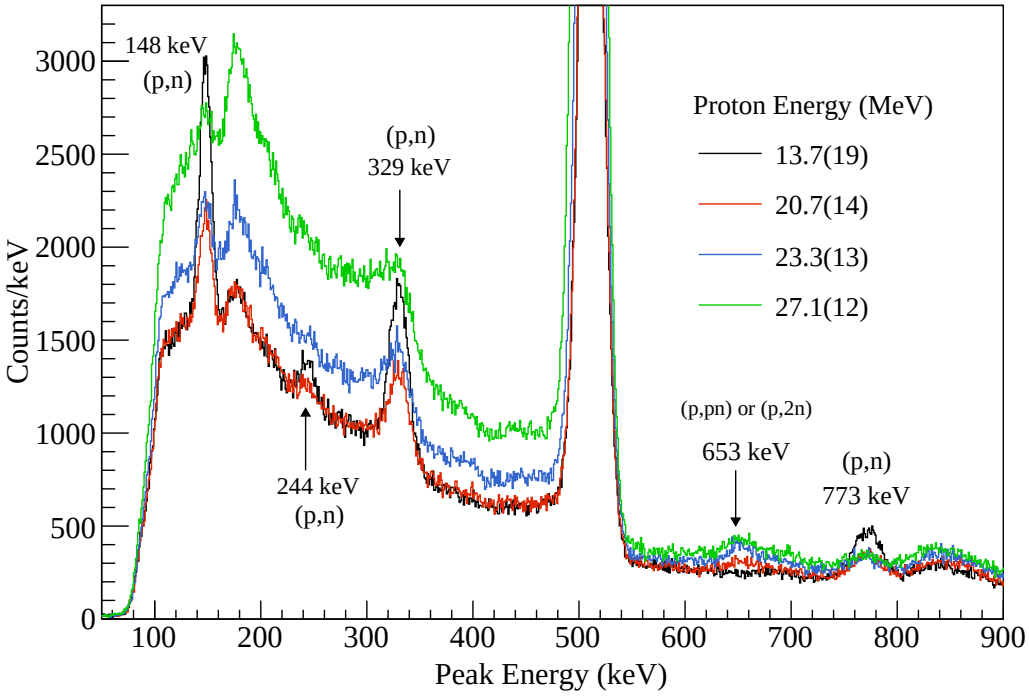

Figure 3.4: Off-beam spectrum collected in one $LaBr_3$ scintillator after the irradiation of the Mo target, illustrating the relative change in intensity of the 148.0(6), 243.7(6), 329.3(3), 773.0(3) keV peaks from the (p, n) reaction. The 1509.6(3) keV peak is not shown in the figure. The 653.9(1) keV peak, which originates from a (p, pn) reaction is also observed. No efficiency corrections have been applied. Since the shape of the background varies as a function of beam energy, the spectra cannot be normalized to one another.

proton beam energy in a molybdenum tumour marker. The sensitivity of HTM RV is limited by the height of the band, which is dominated by the uncertainty in the fitting procedure as a whole, rather than the uncertainty in the individual fits of the peaks (vertical error bars). At an average proton energy of 22 MeV, corresponding to a region where R_{Mo} is most sensitive to energy, the ratio is $R_{\mathrm{Mo}} = 0.91(17)$.

3.3.4 Half-Life Measurement

The half life of the (p, n) reaction product, ^{92}Tc, was evaluated to affirm that the characteristic peaks of interest were populated by the β decay of ^{92}Tc. The half life was evaluated at a beam

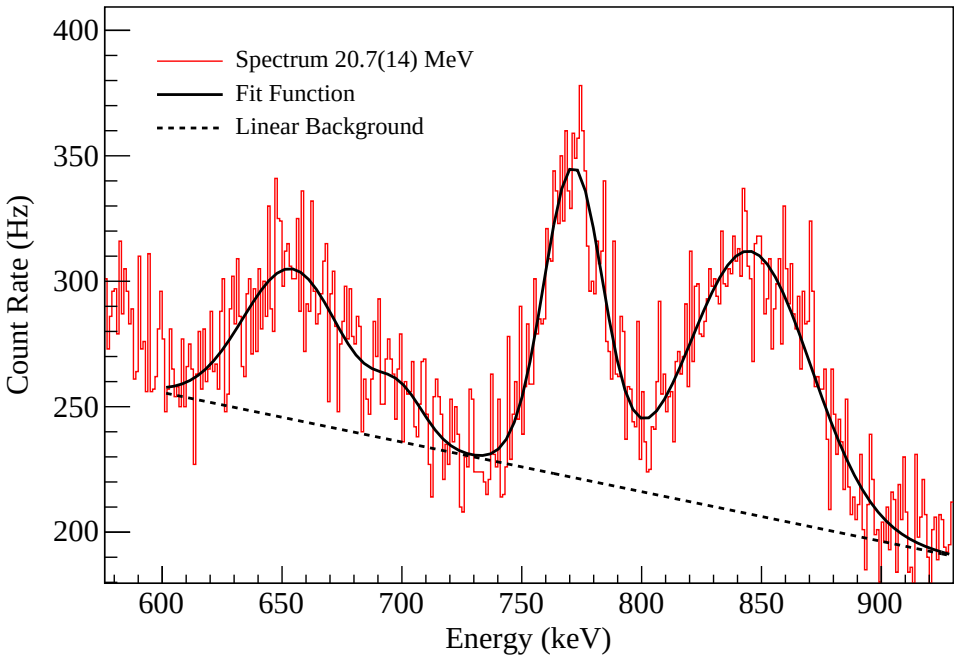

Figure 3.5: Mo spectrum from Figure 3.4 in the region of interest (red), demonstrating a sample fitting technique where the 653 keV and 773 keV peak areas are determined by fitting four peaks as a quadruplet (solid black) on a linear background (dashed black) using GRSISort. The difference in the peak areas obtained between different fitting methods accounts for the width of the uncertainty band in Figure 3.6. This particular fitting technique was not used anywhere in this work.

energy of 13.7 MeV, where the reaction cross section is maximized. By splitting the off-beam period into six 49 s intervals and plotting the area of the 773 keV peak in these intervals as a function of time, the half life was determined to be 265(25) s with a $\chi^2_{red} = 1.6$, which agreed with the literature value of 255(9) s (50). The half-life of the (p, pn) and $(p, 2n)$ reaction products could not be evaluated because the 653 keV peak is populated by three different reaction channels, and the level of statistics acquired did not support the fitting of a function of three exponential curves.

Color	Det.	653 keV peak	773 keV peak
Orange	1	doublet; fixed position and width with 27.1 MeV spectrum	triplet with extra bg peak; fixed position with 13.7 MeV spectrum
Yellow	1	Fit as quintuplet. Fixed position with 20.7 MeV spectrum	
Dark blue	1	doublet; fixed widths	triplet; fixed widths
Black	1	doublet; fixed position with 27.1 MeV spectrum	triplet
Green	2	doublet; fixed position and width with 27.1 MeV spectrum	triplet with extra bg peak; fixed position with 13.7 MeV spectrum
Violet	2	Fit as quintuplet. Fixed position with 20.7 MeV spectrum	
Teal	2	doublet; fixed position and width with 13.7 MeV spectrum	triplet
Red	2	doublet; fixed position with 23 MeV spectrum	triplet

Table 3.1: Parameters used for fitting the peaks at 653 keV and 773 keV, respectively. The colors refer to the resulting R_{Mo} lines in Figure 3.6

3.4 Discussion

3.4.1 Precision of HTM RV using a Mo Marker

This section discusses the intrinsic expected precision for HTM RV based on data acquired with $LaBr_3$ detectors to measure R_{Mo} under realistic conditions in a passive beam delivery PT facility. The intrinsic uncertainty, i.e., the range uncertainty neglecting the impact of external factors such as the CT imaging resolution, is dominated by the error in the measured value of R_{Mo}. For this discussion, $R_{\mathrm{Mo}} = 0.91(17)$ was chosen based on the expected ratio for an average proton energy of 22 MeV, as discussed in Section 3.3.3. Since this R_{Mo} value is located in the most sensitive region (the region of steepest slope of Figure 3.6), the calculated precision reflects the smallest attainable range uncertainty.

As the measured value for R_{Mo} is related to the proton beam energy in the marker, precise knowledge of the function $R_{\mathrm{Mo}}(E_{\mathrm{proton}})$ is required. In general, this function could be calculated from experimental proton activation cross sections and known γ-ray intensities. However, the cross sections for ^{92}Mo activation have not been reported in literature. Instead, we utilize our

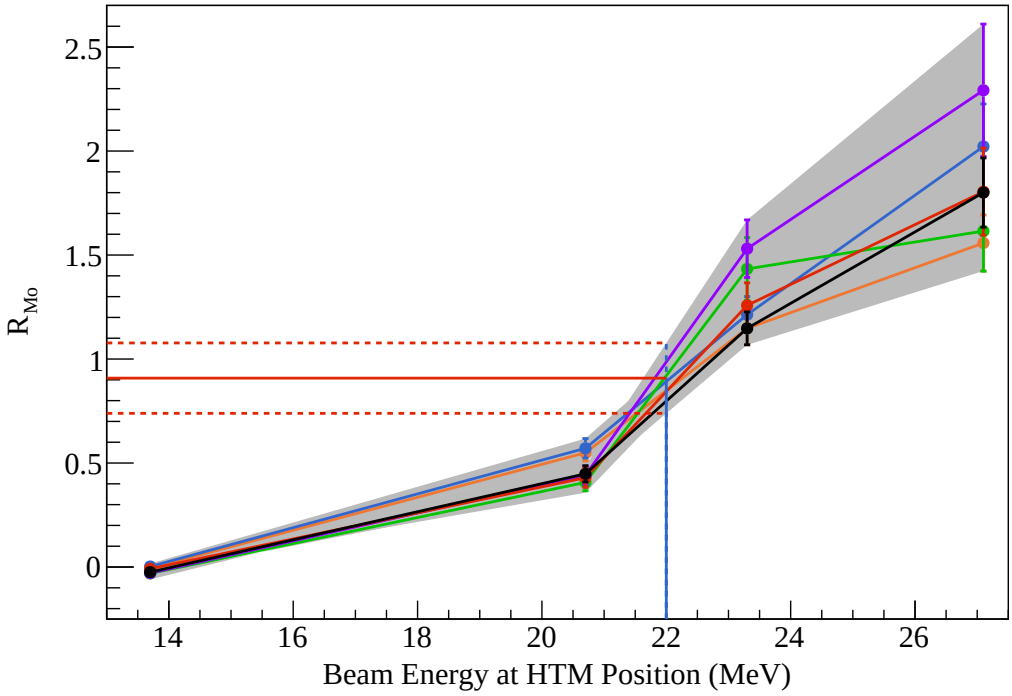

Figure 3.6: The relationship between R_{Mo} and the average proton energy in the HTM is illustrated by the experimental band (grey). To produce this plot, the R_{Mo} values and their associated uncertainties obtained from individual fitting techniques (see Table 3.1 for details) were superimposed (solid lines) and filling the area through the error bars with ROOT. The experimental uncertainty in R_{Mo} was estimated by projecting the average proton energy (blue) onto the experimental band and extracting the minimum, maximum and average R_{Mo} values (red).

experimental results of Figure 3.6 to relate any measured value of R_{Mo} to the proton beam energy in the marker. Given the poor resolution of the $LaBr_3$ detectors and the large energy straggling in passive beam delivery systems, the proton activation cross sections measured in this work have rather large systematic uncertainties from applying various fitting routines, as seen in Figure 3.6. To demonstrate the achievable uncertainty with known cross sections, we select the results of a single fitting routine for R_{Mo} to define the "true" curve of $R_{\mathrm{Mo}}(E_{\mathrm{proton}})$, and assume that the error bars for $R_{\mathrm{Mo}}(E_{\mathrm{proton}})$ are negligible. Although our choice for $R_{\mathrm{Mo}}(E_{\mathrm{proton}})$ might need to be changed after a dedicated cross section and yield measurement, the impact on the precision of HTM RV using a molybdenum marker is expected to be small.

The value of $R_{\mathrm{Mo}} = 0.91(17)$ can now be related to a certain proton beam energy in the marker. This proton beam energy is related to the remaining range of the beam after passing the HTM. Thus, in order to characterize the range accuracy of our HTM RV, the range calibration curve described in Section 3.2.3 was applied to the results of a single line, representing our choice of $R_{\mathrm{Mo}}(E_{\mathrm{proton}})$, in Figure 3.6, resulting in Figure 3.7.

The R_{Mo} value and its experimental error band were now projected onto the experimental curve and the uncertainty in the remaining range of the beam was estimated from the midpoint between the minimum and maximum projected range. A range uncertainty of ± 0.21 mm was achieved. It should be noted that this range uncertainty represents the uncertainty in the remaining range of the beam relative to the position of the HTM in the patient due to errors in proton energy measurement in the marker, and that the uncertainty in the remaining range of the beam from the HTM to the CTV would still need to be estimated. However, it is clear that, due to the small remaining range of a few millimetres, the uncertainty in projecting the remaining range after passing the HTM is generally negligible in the absence of large inhomogeneities within this range. Cases in which large inhomogeneities are present near the distal edge of the Bragg Peak would have to be evaluated on an individual basis.

3.4.2 Effect of Detector Resolution

To explore the resolution limit of our HTM RV method, various uncertainties in R_{Mo} values were assumed and the corresponding uncertainty in the range determined, see Figure 3.8. For instance, if R_{Mo} can be measured with a $\pm 1\%$ uncertainty, an intrinsic range uncertainty of ± 0.01 mm is obtained.

The nominal energy resolution of the $LaBr_3$ scintillators is 2.6% at 662 keV (80) but 4-5% in this energy range at the experimental event rates. This causes large uncertainties in the fitting of the γ-ray peaks, resulting in the rather large uncertainty of $R_{\mathrm{Mo}} = 0.91(17)$, used in Figure 3.7.

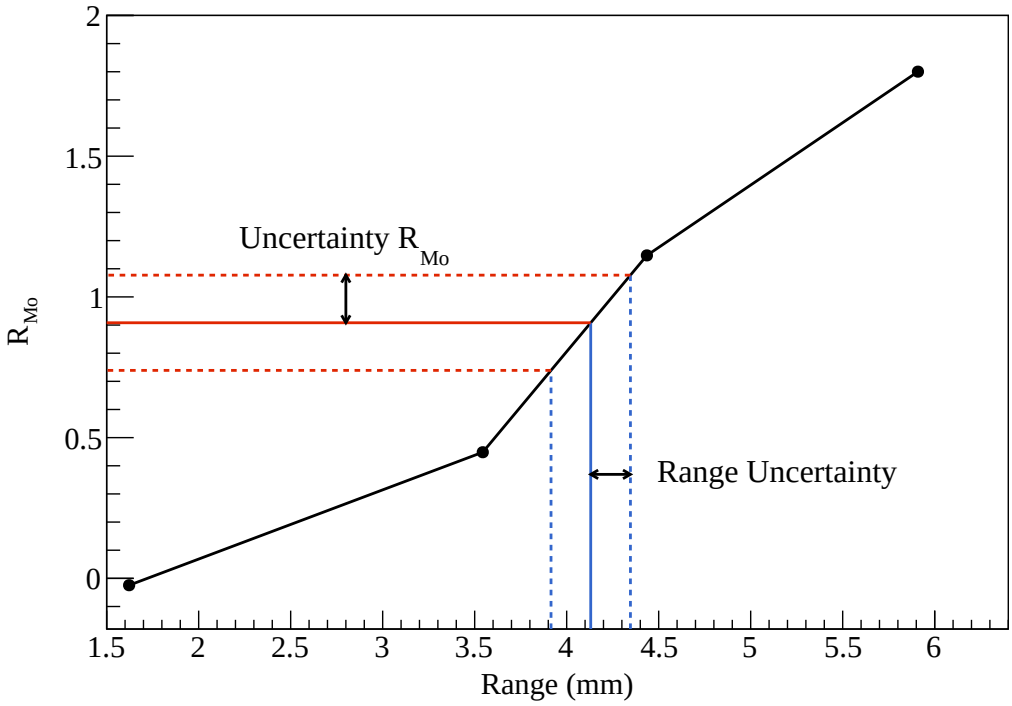

Figure 3.7: The sensitivity of R_{Mo} to the beam's range for a single fitting technique (black). The uncertainty in the range was determined by projecting R_{Mo} (solid red line) and its associated uncertainty (dashed red lines) onto the experimental band, and using the upper and lower limits of R_{Mo} to extrapolate the upper and lower limits of the range. The range (solid blue line) was then evaluated to be the average between its limits (dashed blue lines). When $R_{\mathrm{Mo}} = 0.91(17)$ is assumed, corresponding to an uncertainty of $\pm 18.6\%$, a range of 4.13(21) mm is achieved.

In addition, the fitting was affected by a significant radiation background which was found to be dominated by the activation of material in the treatment room, such as beam collimators.

3.4.3 Effect of Tissue

While in this work R_{Mo} was characterized in air, the clinical feasibility of this technique depends on whether HTM RV can be done with realistic (tissue) backgrounds. This will be investigated in future experiments (see Chapter 4) by irradiating an HTM with additional PMMA to simulate the expected background in tissue irradiation and estimate the SNR that can be achieved. An important advantage of the HTM RV technique is that most of the delayed γ radiation is produced

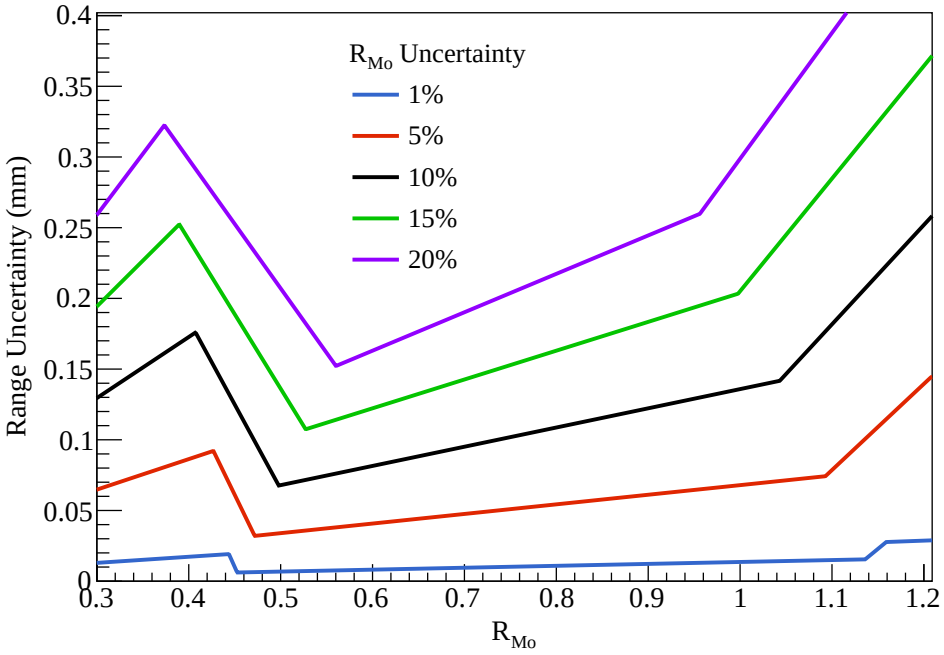

Figure 3.8: Uncertainty in the remaining range of the beam as a function of R_{Mo} for different assumed uncertainties in the measured ratio. Since the uncertainty in the range is dominated by the peak fitting uncertainty, it is expected that with high-resolution spectroscopy with, for example, a HPGe detector system, smaller range uncertainties can be achieved.

by the decay of fusion-evaporation reaction products (mostly ^{11}C, ^{13}N, and ^{15}O) originating from proton activation of tissue. These reactions largely result in the emission of 511 keV γ rays, which does not add significant background to the region of the ^{92}Mo lines of interest. Nevertheless, in future experiments where the radiation background from PMMA is much higher, HPGe detectors should be employed to ensure that the 718 keV peak from the decay of ^{10}C can be distinguished from the 773 keV peak from the decay of ^{92}Tc.

The presence of tissue will also potentially affect the measured value for R_{Mo} due to energy dependence of γ-ray absorption in tissue of the characteristic γ lines emitted from the marker. The use of an HTM with two characteristic peaks which are close together in energy, such as the 773 keV and 653 keV peaks in ^{92}Mo, allows R_{Mo} to require minimal corrections for the difference in attenuation of the γ rays through tissue. This is a significant advantage over measuring a

single γ ray, which would require an estimate of the total absorption of the γ ray in the patient, among other complications of absolute intensity measurements, such as the influence of detector efficiencies, beam intensities, data acquisition deadtimes.

Depending on the diameter of the treatment beam and the clinical scenario, tissue inhomogeneities can have a major impact on the results presented in this work, see Kasanda et al. (1). If inhomogeneities along the beam path substantially alter the energy distribution of the protons at the marker, the remaining range can no longer be evaluated in a model-independent way. Rather, the measured ratio R_{Mo} now reflects the integrated cross section of the proton energy distribution at the marker position. This information can be compared to MC simulations, but the exact uncertainties will strongly depend on the clinical scenario and need to be studied in future MC simulations and experiments.

3.4.4 Effect of Range Straggling

Due to the nature of passive beam delivery systems, the HTM was irradiated with a broad distribution of proton energies. While in this work R_{Mo} values were plotted as a function of the average proton energy, in reality, R_{Mo} represents a weighted average of reaction cross sections over a distribution of proton energies that irradiate the HTM. A precise measurement of these cross sections using a monoenergetic pencil beam can determine the dependence of R_{Mo} on absolute reaction cross sections. While the shape of the R_{Mo} response curve to monoenergetic protons is expected to differ from that of average proton energies in Figures 3.6 and 3.7, the difference is not expected to greatly impact the sensitivity of HTM RV. Future measurements using HPGe are planned for a dedicated measurement of $R_{\mathrm{Mo}}(E_{\mathrm{proton}})$ using thin molybdenum foils to achieve precise cross section results for the proton activation of molybdenum as a function of proton energy.

Since a 63 MeV beam was extracted in this work, whose range in PMMA is only 29.6(4) mm, the spread in proton energies due to range straggling was relatively small. As the HTM would be

placed very close to the tumour, the spread of the proton beam due to scattering off the marker would also be small. The impact of inherent range straggling of the proton beam for HTM RV was investigated in Kasanda et al. (1) (see Chapter 2) for a range of proton energies. For tumours located deep in the tissue, the effect of range straggling is more significant, as the HTM is irradiated with a broader distribution of proton energies. Because of the error in extracting average proton energies from a distribution of proton energies hitting the marker, sensitivity of HTM RV to the beam energy is reduced, which can be seen by the flattened R_{Mo} response curve in Kasanda et al. (1). However, simulations suggest that a sub-millimetre uncertainty in the remaining range can still be obtained for tumours as deep as 258 mm with HTM RV when R_{Mo} is measured with the resolution of a HPGe detector system (1). These results suggest that as long as the distance from the HTM to the tumour remains the same for varying tumour depths, the range uncertainty will only weakly depend on the depth of the tumour.

In a clinical application, once the response of R_{Mo} to monoenergetic proton energies is characterized with a pencil beam, the curve can be convoluted with the clinical proton energy distribution. The depth-dependent uncertainty due to range straggling can then be applied to determine the total range uncertainty that should be given as the safety margin.

3.4.5 Comparison to clinical RV methods

Compared to current RV techniques which are already in pre-clinical and clinical stages, our result suggests that HTM RV may greatly improve the range accuracy in PT, especially for cases in which the tissue is relatively homogeneous across the beam diameter. The impact of inhomogeneous tissue in the beamline upstream from the HTM will be investigated in future work.

A range accuracy of 1-2 mm has been achieved in coregistered bony structures using offline PET/CT (25). There are inherent limitations to this technique, such as the biological perfusion of PET activity and patient motion during the 20-30 minute acquisition time (25; 81). Online

PET systems are incorporated with the proton beam "nozzle" to acquire data during fraction delivery. This method minimizes the impact of acquisition delays present in offline PET. The main limiting factors of this method are the high background γ rates during fraction delivery, as well as limited angle coverage due to spatial constraints(26; 23).As PET RV relies on a comparison to MC simulations, it is limited to the accuracy that can be achieved with a simulation, due to uncertainties in converting CT Hounsfield units into tissue composition, as well as an overall paucity of experimental reaction data for thick targets (26).

RV using PG emission allows signals correlated with the proton dose to be measured in real time, without the biological washout that poses a problem in the PET technique. Shifts in proton Bragg peaks of 2 mm have recently been measured with PG using a knife-edge slit collimator during irradiation of head and neck tumours (33; 32) as well as tissue-equivalent plastic phantoms using a Compton camera (36). Proton range shifts as small as 1 mm were recently detected in plastic phantoms with a clinical PGS prototype (82).

From our results, it is clear that HTM RV has potential to further reduce the range uncertainty into the sub-mm regime, and its clinical feasibility should be investigated. In future experiments, the range uncertainty in tissue-equivalent plastic phantoms will need to be evaluated in order to determine the precision of HTM RV with realistic backgrounds, penetration depths, and tissue inhomogeneities.

3.5 Conclusions

To characterize the feasibility of a new method of range verification for proton therapy, delayed γ radiation from proton irradiation of a Mo marker was measured in a proof-of-principle experiment. The experiment aimed to relate the relative intensity of two delayed characteristic γ rays originating from fusion-evaporation reactions on a molybdenum target to the remaining range of the beam. The results suggest that the remaining range of the beam downstream of an HTM can extracted

with sub-millimetre uncertainty for a beam energy at the isocenter of 63 MeV. While characterizing the range uncertainty that can be attained with HTM RV with higher beam energy and realistic tissue remains the subject of future studies, HTM RV presents a viable alternative to current range verification methods which do not allow a model-independent implementation of an instant safety feedback, and could allow tumours near organs at risk to be safely treated with highest precision, further improving the therapeutic index of PT.

Chapter 4

Follow-Up Experiment with protons in a phantom

4.1 Introduction

This chapter has been adapted from Kasanda et al. (3) in accordance with the IOP Publishing Author Rights Policy for subscription articles.

While the experiment by Burbadge et al was successful in demonstrating the possibility of range verification using a single HTM material, the achieved signal-to-noise ratios of the γ-rays of interest were too low for a clinical application. In the follow-up experiment at TRIUMF presented in this chapter, we improve on our previous study by introducing a composite HTM containing three candidate materials, enabling us to make use of the strongest reaction channel of each material. We also employ High-Purity Germanium (HPGe) detectors with superior energy resolution. This allowed us to detect our peaks of interest over a simulated tissue background, induced by placing the composite HTM into a PMMA phantom.

Table 4.1: γ rays of interest originating from interactions between the composite HTM target and the proton beam. This information includes natural abundance of the isotope of interest, the nuclear reaction from which the γ ray originates, the isotope responsible for the emission of the γ ray of interest, the half-life of this isotope (decay $T_{1/2}$), the energy of the emitted γ ray (E_γ) and the relative intensity of the emitted γ ray (I_γ) (86).

Material	Natural Abundance	Reaction of Interest	Decay Product	Decay $T_{1/2}$ (minutes)	E_γ (keV)	I_γ
^{89}Y	100%	^{89}Y(p,n)^{89}Zr	^{89m}Y	4.161(10)	587.8(1)	89.62%
^{92}Mo	14.53%	^{92}Mo(p,n)^{92}Tc	^{92}Mo	4.25(15)	773.0(3)	99.857%
^{64}Zn	49.17%	^{64}Zn(p,n)^{64}Ga	^{64}Zn	2.627(12)	991.56(10)	48.3%

4.2 Materials and Methods

4.2.1 Hadron Tumour Markers

As established in Chapters 2 and 3, the method of HTM RV requires two strong reactions of interest in order to limit dependence on beam intensity and simulations by analysing the ratio of the two signals. ^{nat}Mo was established in these previous works to be a good candidate HTM, as both the ^{92}Mo(p,n)^{92}Tc and ^{92}Mo(p,pn)^{91m}Mo reactions satisfied most of the conditions for an HTM signal. However, the signal from the ^{92}Mo(p,pn)^{91m}Mo reaction was found to be significantly weaker than the one from the ^{92}Mo(p,n)^{92}Tc reaction, limiting the precision of the measurement. In order to take advantage of the strongest signal of multiple candidate markers, we introduce the concept of a composite HTM. It is composed of multiple candidate materials, each needing to produce only one strong signal of interest upon activation with the treatment beam.

In preparation of the experiment, candidates for HTM RV with a proton beam were investigated, based on the properties listed in Chapter 1.6. The PACE4 code (83; 84) was used to calculate cross sections for protons incident on a large number of naturally abundant metal isotopes at several Bragg Peak energies. Reaction products with a significant cross section in the relevant energy region were compared with NNDC data (85) to ensure they satisfy the half-life and γ emission requirements of an HTM.

Of all the metals examined, ^{nat}Mo, ^{nat}Y, ^{nat}Zn, ^{nat}Ni and ^{nat}Mg were identified as having favourable properties and were selected for investigation in this experiment. ^{nat}Mo had already been established in Chapter 3 to be a good candidate for HTM RV. Following preliminary experiments and online analysis, ^{nat}Ni and ^{nat}Mg did not produce a favourable signal upon proton activation and were therefore dismissed as HTM candidates. ^{nat}Mo, ^{nat}Y, and ^{nat}Zn were selected as components of the composite HTM, see Table 4.1 and Figure 4.1.

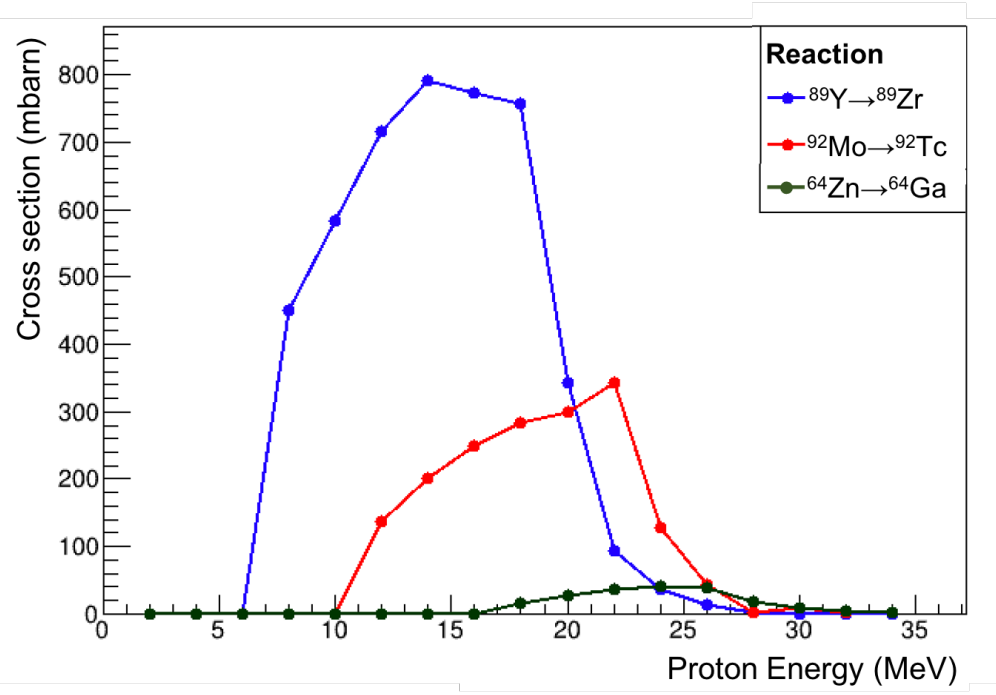

Figure 4.1: Total cross sections for (p,n) reactions on ^{89}Y, ^{92}Mo, and ^{64}Zn, obtained using PACE calculations (83; 84), for proton energies up to 35 MeV. Default settings for the optical parameters in PACE were used.

4.2.2 Experimental Setup

This follow-up experiment was performed at the same facility described in Chapter 3, the Proton Therapy Research Facility (PTRC) at beamline 2C1 of the TRIUMF 520 MeV cyclotron (74), which used to clinically treat patients with ocular melanomas (67), see Figure 4.2. As in the previous

experiment, a 70 MeV proton beam was extracted from the cyclotron with an intensity of 2 nA. The facility is a passive beam delivery system with a maximum field size of 50 by 50 mm in the isocentre, where the beam energy after transversing monitoring detectors and beam shaping devices is 63 MeV. The energy of the proton beam can be changed by intercepting the beam with a range shifter (RS), which is a piece of Poly(methyl methacrylate) (PMMA) of adjustable thickness. The delivered dose is monitored by an ionization chamber (IC) upstream of the collimator. For more details on the beam settings used in this experiment, see Chapter 3.

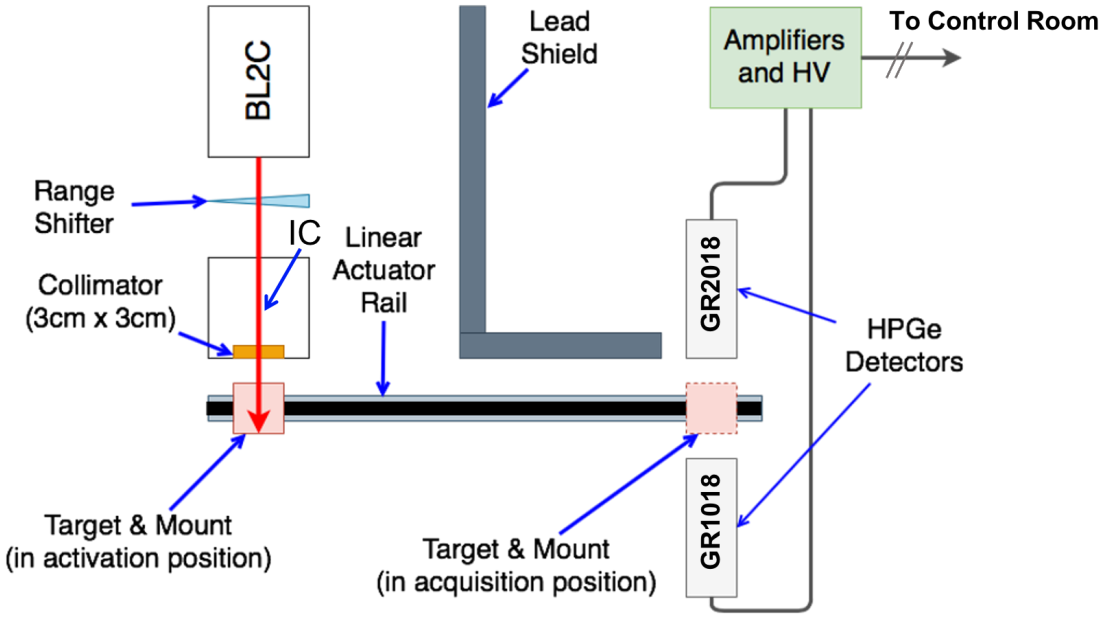

Figure 4.2: Sketch of experimental setup at the PIF/NIF facility. The targets are mounted on the remotely-controlled linear actuator rail. While the beam is on, the target is located in the indicated activation position or isocentre. When the activation is complete, the beam is switched off and the targets are moved remotely to the indicated measurement position for acquisition of the delayed γ-ray spectrum. This sketch is not to scale.

In order to perform this follow-up measurement, thin foils of ^{nat}Mo, ^{nat}Y and ^{nat}Zn, measuring approximately 2 cm×2 cm were arranged in tiles as shown in Figure 4.3. The thickness was 200 µm for the ^{nat}Mo and ^{nat}Zn foils, and 150 µm for the ^{nat}Y foil. The same composite target was used for all activations to ensure the composition of the target was consistent across measurements. These composite target foils were mounted on a linear actuator rail (Zaber, model X-LC40B1800-E08),

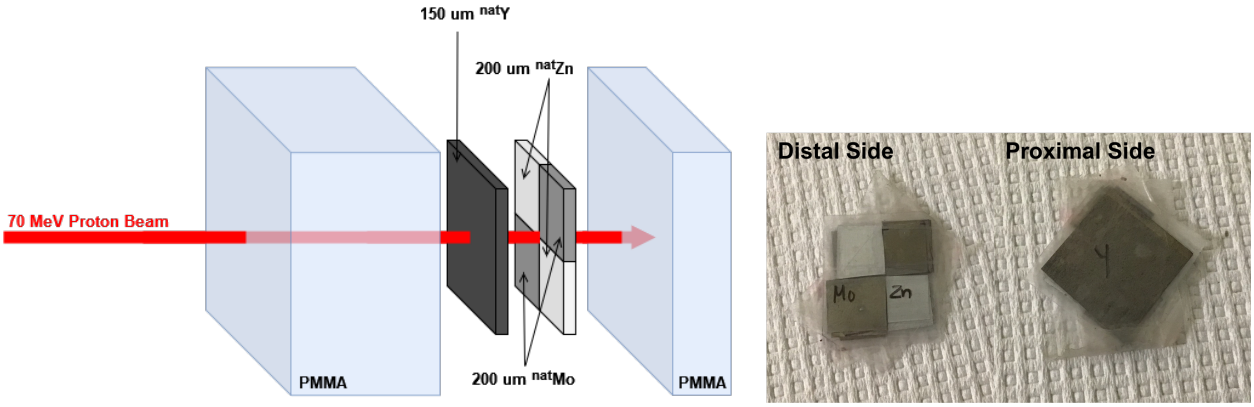

(a) (b)

Figure 4.3: (a) Sketch of composite HTM target used for runs in which a block of PMMA was used to degrade the treatment beam to the desired energy (PMMA runs). Note that spaces between the components are included in this sketch for visual clarity only. In the experiment, all target components were clamped together with no air in between. Additionally, the red arrow only depicts the direction and positioning of the treatment beam relative to the target and is not representative of the size of the beamspot. (b) Photos of proximal and distal side of the assembled composite marker.

which was remotely operated from the control room. The rail transported the targets in the span of 2 to 3 seconds over a distance of about 4 m from the activation position in the beam line indicated in Figure 4.2 to the measurement position located between the two detectors. This allowed the detectors to be positioned at a safe distance from the beamline to avoid excessive neutron-induced damage to the detector crystals during the target activation period. Our detector system consisted of two High-Purity Germanium (HPGe) detectors: a Mirion ReGe GR1018 and a Canberra GR2018. The GR1018 was positioned facing the distal side of the target, while the GR2018 was positioned opposite to it facing the proximal side, behind a large Pb shield indicated in Figure 4.2. The distance between the two detectors was 8 cm, and the composite HTM target was approximately centered between them. Several shielding bricks were positioned between the beamline and the detectors to further minimize damage and γ background from the proton beam. Both detectors were powered with a CAEN DT5521EM HV power supply, and data acquisition was performed using a GRIF-16 ADC VME-6U module with a GRIF-C data collector (87). Energy calibrations

Table 4.2: Summary of settings used for runs in which the facility's range shifter was used to degrade the beam energy to the desired setting (RS runs). The average beam energy at the isocentre is calculated from a calibrated SRIM simulation of the treatment beam, and the remaining beam range in PMMA is calculated as described in Section 4.2.2. The counts in the IC during each of these runs is included as well, and is used as a normalization factor in Figure 4.7.

Range Shifter Setting	Range Shifter Thickness (mm)	Average Beam Energy at Isocentre (MeV)	Remaining Range (mm)	IC Counts
2050	22.88	27.17	6.468	111,935
2225	24.65	22.71	4.680	114,911
2300	25.40	20.59	3.924	118,630
2400	26.41	17.5	2.929	122,087
2450	26.91	15.73	2.420	127,236
2500	27.42	13.71	1.890	126,031
2600	28.42	8.97	0.886	142,006
2700	29.43	7.31	0.614	218,286

for the HPGe detectors were performed using a ^{152}Eu source. The energy resolutions achieved in the GR1018 and GR2018 detectors were 0.92(5)% and 0.30(2)% at 587 keV, respectively. All activations were performed using the maximum field size of 3 cm×3 cm in order to evenly irradiate the entire composite HTM, and to avoid contributions to the γ ray and neutron background from activation of a collimator.

Data was acquired at eight different proton energies that were adjusted using the RS device in order to characterize the energy sensitivity of HTM RV. The proton beam energies in the isocentre for each RS setting used are summarized in Table 4.2, and were calculated from an experimentally-validated SRIM (76) simulation of the treatment beam (88). Irradiations in which the beam energy was reduced to the desired setting using the RS are hereafter referred to as RS runs.

In addition to the activations performed using the facility's RS, a separate set of runs was acquired in which the Range Shifter was removed from the beamline, and the treatment beam was instead degraded in a block of PMMA in which the composite HTM was embedded (see Figure 4.3b) to simulate the background produced from tissue. This block of PMMA was mounted to

Table 4.3: Summary of settings used for runs in which a block of PMMA was used to slow the beam to the desired energy (PMMA runs). The entrance energy at the composite HTM and the remaining range of the beam in PMMA are calculated as described in Section 4.2.2. The counts in the IC during each of these runs is included as well, and is used as a normalization factor in Figure 4.7. The uncertainty in the remaining range is due to the uncertainty in the PMMA block thickness.

PMMA Thickness (mm)	Entrance Energy (MeV)	Remaining Range (mm)	IC Counts
28.85(3)	9.57(15)	0.99(3)	109,633
27.33(10)	16.07(34)	2.19(10)	105,686
26.94(3)	17.43(7)	2.91(3)	105,744
25.91(3)	20.61(8)	3.93(3)	112,554
25.05(5)	23.02(13)	4.79(5)	141,433
23.5(11)	26.95(26)	6.38(11)	126,231

the linear actuator rail along with the composite HTM such that it would also be moved to the measurement position following activation. This set of runs is hereafter referred to as PMMA runs. A sketch of the target including the tissue simulating PMMA is shown in Figure 4.3a. A variety of PMMA thicknesses were used in this experiment to measure the variation of the composite HTM peak ratio as a function of the incident beam energy on the composite HTM and are summarized in Table 4.3. The beam energy at the proximal edge of the composite HTM foil for these runs was estimated using the same method described in Chapter 2, in which the numerical solution established by Martinez et al. (61) is compared with GEANT4 data of proton ranges to obtain the parameters in the numerical simulation. The GEANT4 data depicts the energy loss of protons in a block of PMMA with a density of $1.17\,\mathrm{gcm}^{-1}$.

For both the RS runs and the PMMA runs, the estimation of the remaining range of the beam in PMMA as a function of the beam energy at the foil entrance was performed using the same numerical solution. While the composite HTM foil itself degrades the proton energy, we chose in this experiment to not include the energy loss in our calculation of the remaining range, and instead to consider the remaining range of the beam beside the marker. This is clinically more relevant

for a fiducial marker of realistic clinical dimensions, as typically they are not placed in front of the treated tumour. Fiducial markers are significantly denser than tissue and induce distortions in the dose distribution distal to their position in the patient. The remaining range of the beam is calculated for each of the energies described in Tables 4.2 and 4.3, using the same GEANT4 data set and numerical solution described in Section 4.2.2.

The initial unpacking of the raw data to analysis histograms was performed with GRSISort (version 4.0.0.0) (78), a C^{++}-based sorting code developed by the TIGRESS & GRIFFIN collaboration at TRIUMF.

4.3 Results

4.3.1 Data rates

Targets were activated for 150 s in the position indicated in Figure 4.2, then moved into the measurement position between the two HPGe detectors and allowed to decay for 300 s while the γ-ray spectrum is recorded. Two activations and subsequent decay measurements were performed in each run to maximize the HTM signal given the half-lives of the reaction products. The measured counts throughout one of the PMMA runs is depicted in Figure 4.4.

Count rates in the activation period of RS runs were approximately 20 kHz in the GR1018 and 28 kHz in the GR2018. When the beam was switched off and the target was moved to the measurement position, the count rates in the RS runs were immediately reduced to approximately 1.8 kHz and 1.6 kHz in the GR1018 and GR2018 detectors, respectively. Count rates in the activation period of PMMA runs were approximately 25 kHz in the GR1018 and 33 kHz in the GR2018. In contrast to the RS runs, the count rates in the PMMA runs increased to approximately 50 kHz in each detector when the beam was switched off and the target was moved to the measurement position. This is because the PMMA block used to slow the beam to the desired energy is also

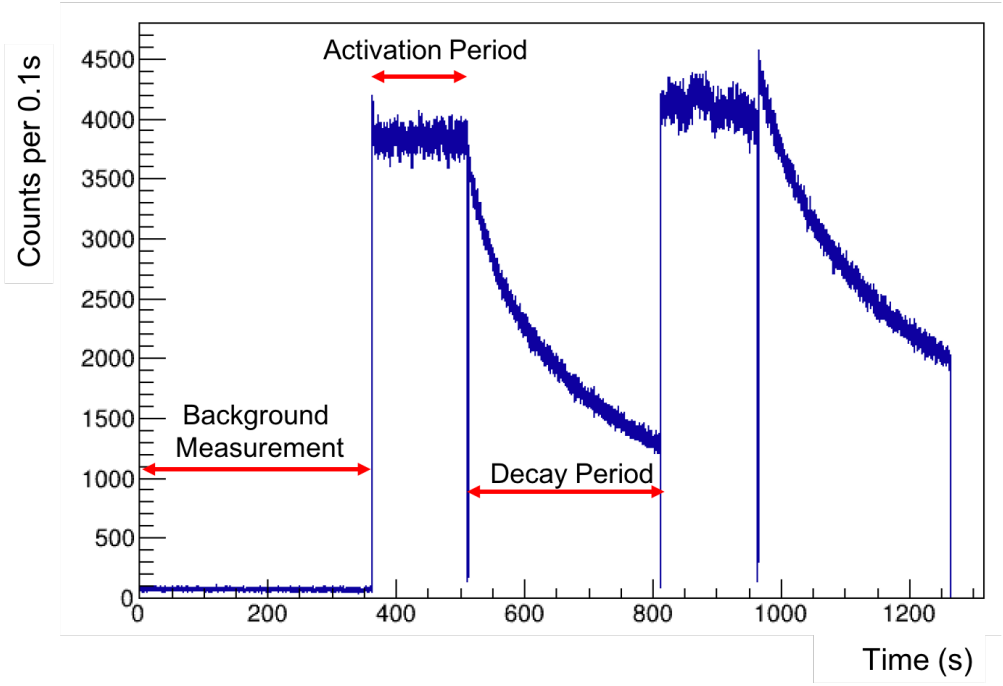

Figure 4.4: Gamma intensity in the GR2018 as a function of time for one run. The counts in the background measurement period originate from target and room activation accumulated from previous runs. The counts in the activation period originate from prompt radiation induced by the treatment beam while the target is undergoing activation. After the target has been activated for 150 s, the beam is stopped and the target is moved into the measurement position between the detectors. The decay of the activated target is then measured for an additional 300 s, as indicated by the time period labeled "decay period". Each run consisted of a background measurement followed by two consecutive activation-decay sequences. Following each activation period, there is a brief downward spike in data rate which corresponds to the time window in which the beam has been turned off but the target has not yet reached the measurement position

moved to the measurement position alongside the composite HTM to simulate tissue background.

Analysis using a high-activity ^{60}Co source revealed that for the data rates achieved in this experiment, detector deadtime including pileup remained below 1% at the rates used for the RS runs. The deadtime for the PMMA runs was more significant, reaching 11% at rates of 50 kHz. However, since the ratio of the γ rays of interest is largely independent of detector efficiency, deadtime corrections were not implemented in this analysis.

4.3.2 Experimental Gamma spectra

The literature values for the γ-rays of interest are summarized in Table 4.1. Peaks were identified in our spectrum that corresponded to the literature values in both energy and in half-life, and are only present in runs during which the composite HTM foil was activated. This is highly indicative of the identified peaks originating from the reactions of interest. An example spectrum from a PMMA run in which the peaks of interest have been identified is shown in Figure 4.5.

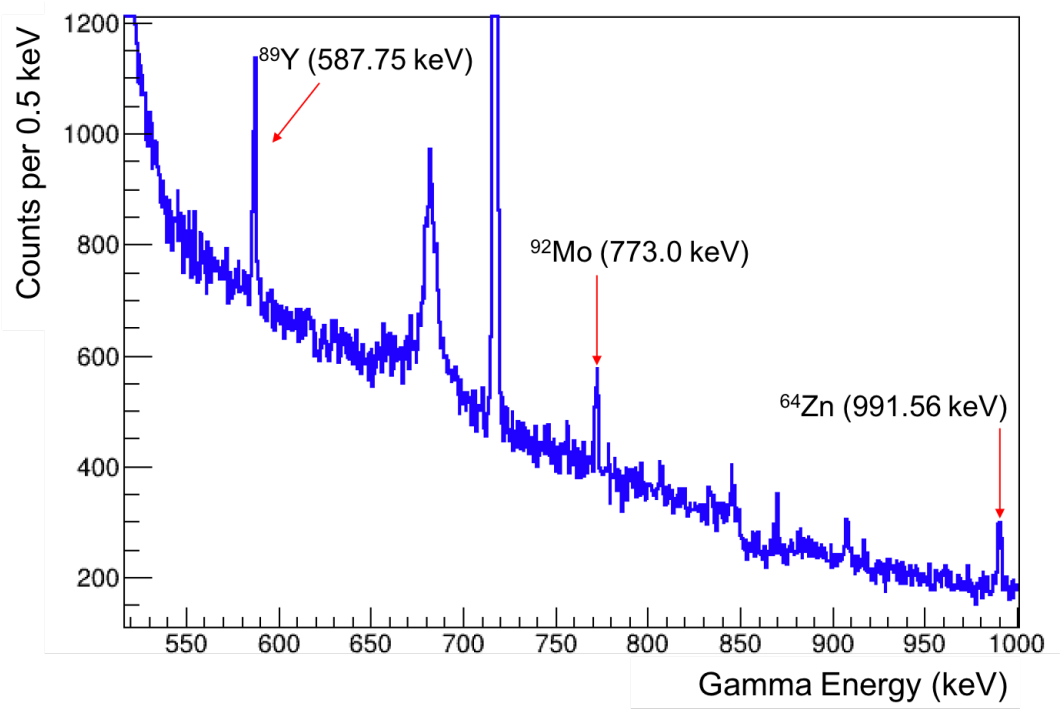

Figure 4.5: GR2018 γ-ray spectrum from a PMMA run with labeled peaks of interest originating from the composite HTM. The unlabeled peaks in this spectrum are background peaks caused by activation of the PMMA block. Note that the large background peak at 718.35 keV (from the β^+ decay of ^{10}C) is cut off at the top in order to better visualize the peaks of interest.

4.3.3 Background Subtraction and Normalization

In order to avoid uncertainty contributions from variations in the composition of the HTM, the same target was used for all runs. In each run, a background measurement was performed for

5 min prior to target activation, as shown in Figure 4.4. In most of the runs, the activity from the previous run had sufficiently decayed to avoid any significant contributions to the measured peak area following target activation. A few runs required minor adjustments to the measured peak area, where the peaks of interest were fitted at 30 s intervals in the background measurement. The decay of these peaks was then calculated as a function of time with the half-life fixed to the known theoretical value for each γ-ray of interest. These fit results were used to calculate the number of counts to be subtracted from the measured peak areas.

The ionization chamber (IC) counts during the activation period of each run are summarized in Tables 4.2 and 4.3, and were used as a normalization factor in the analysis in Section 4.3.4. All peak areas are normalized to 100 000 counts in the IC.

4.3.4 Peak Fitting

Focusing on the energy region of interest for the 587.8(1) keV peak, Figure 4.6 shows the fitting results with a Gaussian function over a quadratic polynomial background. Due to the two detectors used in this experiment having significant differences in their energy resolution, the gamma spectra from each detector were fitted independently, and the resulting peak areas measured in both detectors were summed together. The resulting normalized and background-subtracted total peak areas for each run were then plotted as a function of the beam energy at the proximal edge of the composite HTM foil in Figure 4.7, showing decent agreement with each other and following the features of the cross sections in Figure 4.1.

4.3.5 Calculation of Peak Ratio

As described in Chapters 2 and 3, the relative intensity of the peaks of interest provides an absolute measurement of the remaining range of the beam independently of beam rate, circumventing the need for comparison to complex Monte Carlo simulations to extract a range measurement. In

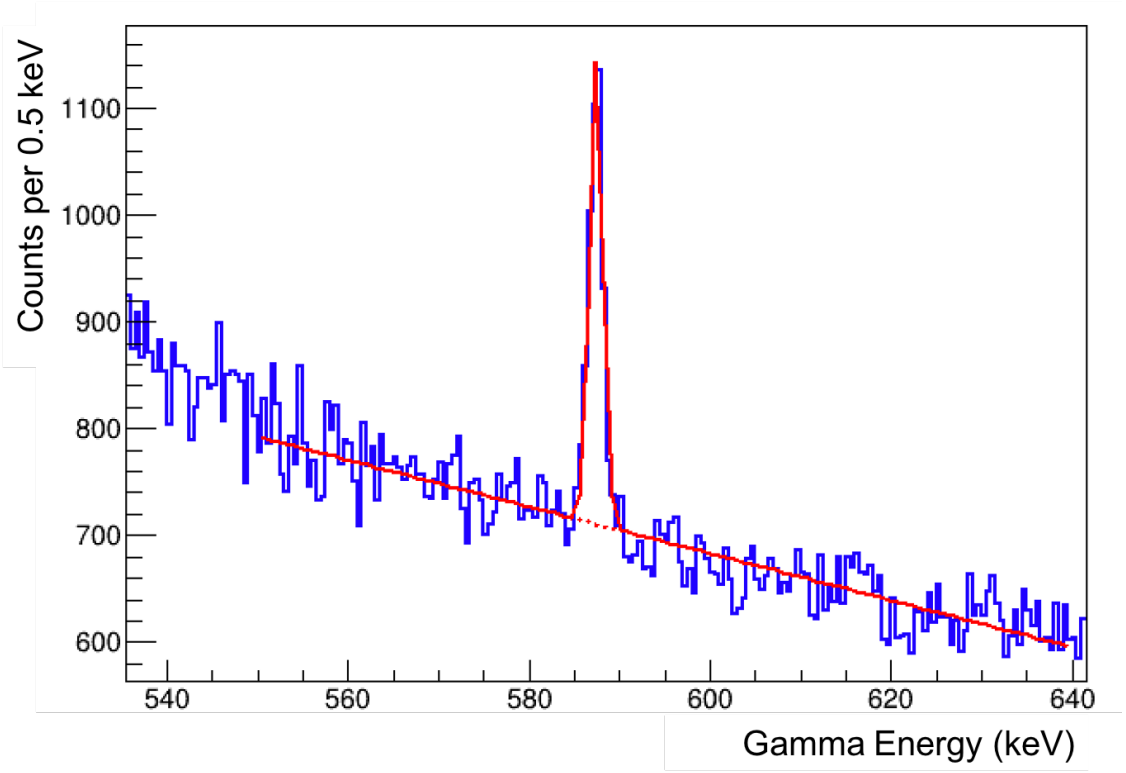

Figure 4.6: Example of a γ-ray peak of interest fitted with a Gaussian function over a quadratic polynomial background. This spectrum was acquired by the GR2018 detector in one of the PMMA runs.

this work, we introduce a new definition of the peak area ratio

$$R_{M1/M2} = \frac{A_{M1} - A_{M2}}{A_{M1} + A_{M2}}, \tag{4.1}$$

in which M1 and M2 represent the two HTM materials in question, and A_{M1} and A_{M2} represent the respective experimentally measured peak areas of the γ-rays of interest emitted following the activation of these materials. This updated definition of the peak area ratio is less sensitive to variation in the area of very small peaks, preventing large jumps in the ratio when one of the peaks disappears. The three possible peak ratios that can be extracted from the composite HTM used in this experiment are $R_{Mo/Y}$, $R_{Mo/Zn}$, and $R_{Zn/Y}$. The results of these experimental peak ratios for the RS runs are plotted against the remaining range of the beam in Figure 4.8. The uncertainties are in the ratio are calculated using standard uncertainty propagation on Equation 4.1, taking

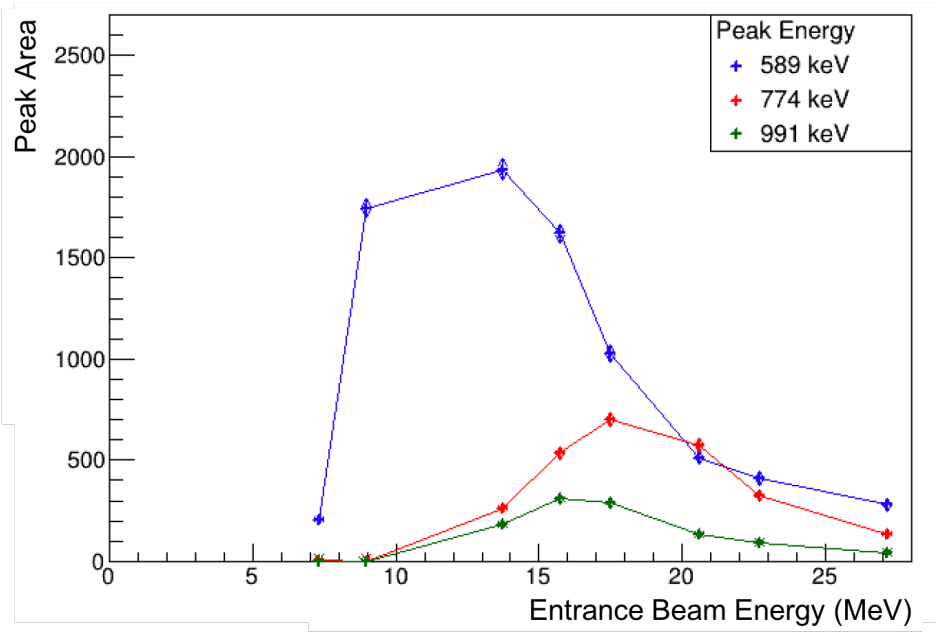

(a)

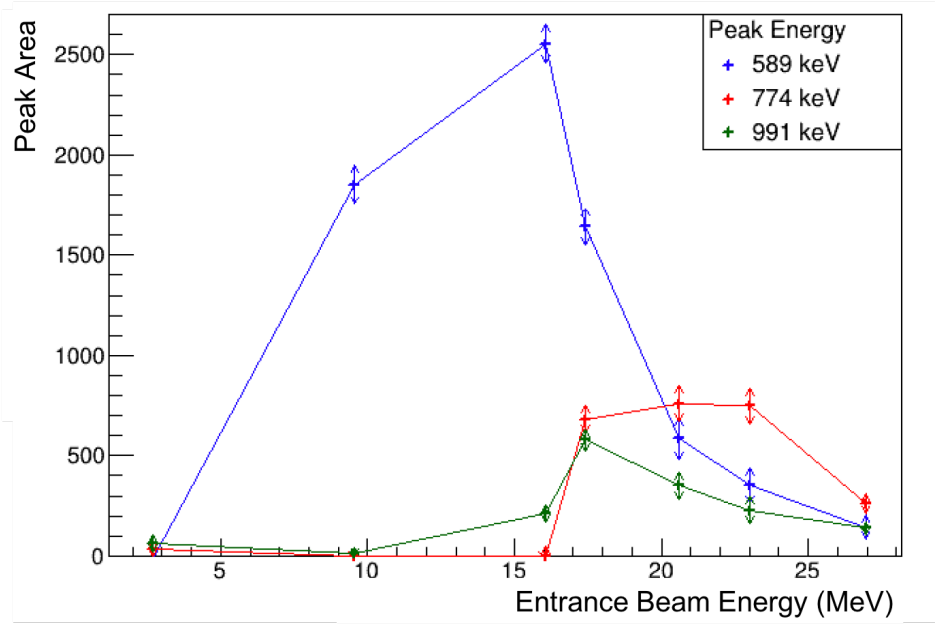

(b)

Figure 4.7: Sum of fitted, normalized, and background-subtracted peak areas for both detectors as a function of the entrance beam energy for (a) each of the RS runs described in Table 4.2 and (b) each of the PMMA runs described in Table 4.3.

into consideration the statistical uncertainty in the measured peak areas and uncertainties in the background subtraction.

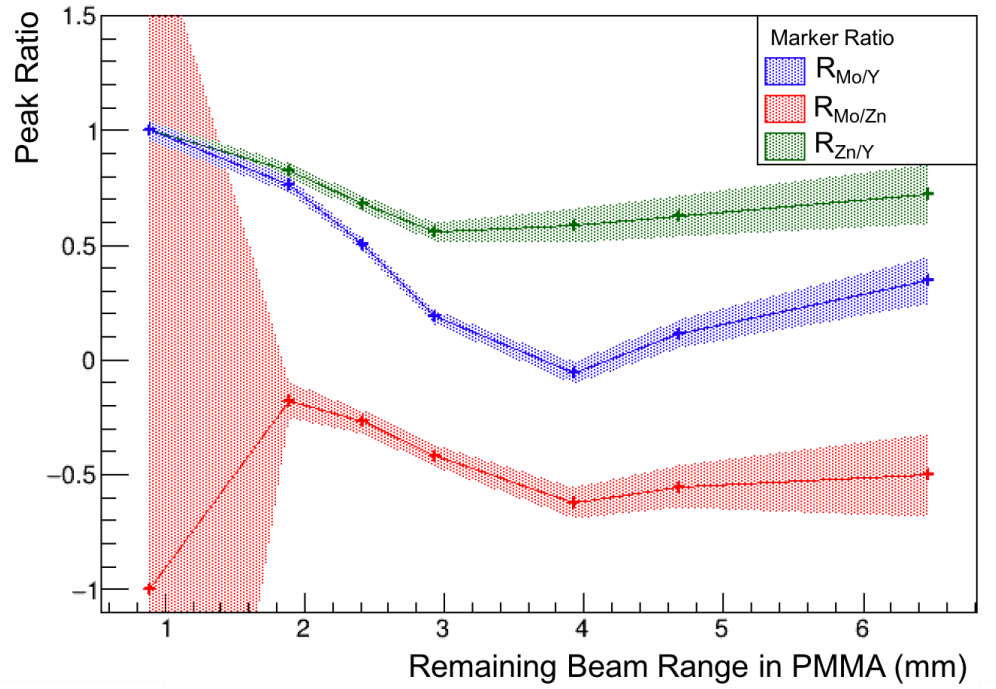

Figure 4.8: Plot of the measured peak ratios $R_{Mo/Y}$, $R_{Mo/Zn}$, and $R_{Zn/Y}$, calculated using data from the RS runs in Figure 4.7a and Equation 4.1, as a function of the remaining beam range for each run (see Table 4.2). The uncertainty is indicated with the colored bands.

This plot indicates that of the three peak ratios, $R_{Mo/Y}$ is the most sensitive indicator of remaining beam range. The larger cross section for the ^{89}Y(p,n)^{89}Zr and ^{92}Mo(p,n)^{92}Tc reactions results in small statistical uncertainties in $R_{Mo/Y}$, compared with $R_{Mo/Zn}$, and $R_{Zn/Y}$. The energy offset of the excitation functions for the two reactions of interest results in a steeper slope for this ratio as a function of remaining beam range. The other two ratios exhibit a less strong dependency on remaining beam range and larger uncertainties. As a result, they are excluded from further investigation. The peak ratios measured in the PMMA runs are summarized in Table 4.4, in association with the theoretical remaining range calculated in Table 4.3 for each setting at which the ratio was measured.

Table 4.4: Measured ratio, $R_{Mo/Y}$, for each of the PMMA runs described in Table 4.3 that fall within the sensitive range of 1-4 mm.

Theoretical Remaining Range (mm)	Measured Ratio $R_{Mo/Y}$
0.99(3)	1.00(7)
2.19(10)	0.59(5)
2.91(3)	0.41(5)
3.93(3)	-0.13(1)

4.4 Discussion

4.4.1 Range Reconstruction and Sensitivity of Method

In order to perform a range measurement which takes into consideration the background contributions of tissue, we reproduce the process established in Chapter 2 in an experimental setting. The measurements from the RS runs, in which the peak ratio can be measured precisely on a lower background, are used as a calibration curve, like the one shown in Figure 2.7b. The peak ratio measurements and associated uncertainties from the PMMA runs are then projected against this calibration curve to extract the remaining range of the beam, as illustrated in Figure 4.9. Note that, like in Figure 2.7b, the region of this plot that is useful for range reconstruction is limited to the range of values for which each ratio is correlated with a unique range. In the case of the composite HTM used in this experiment, the sensitive range extends from approximately 1 mm to 4 mm remaining range. Beyond this range, the ratio function, $R_{Mo/Y}$, does not allow unique assignment of the remaining range of the beam.

The extracted remaining range using the method depicted in Figure 4.9, referred to as the "Reconstructed Range", can then be compared against the theoretical remaining range predicted according to the thickness of PMMA used to slow the beam (calculated as described in Section 4.2.2, and listed in Tables 4.3 and 4.4) to obtain a measure of the sensitivity of this range verification method. This is similar to the process used in Chapter 2. The results of this comparison for the

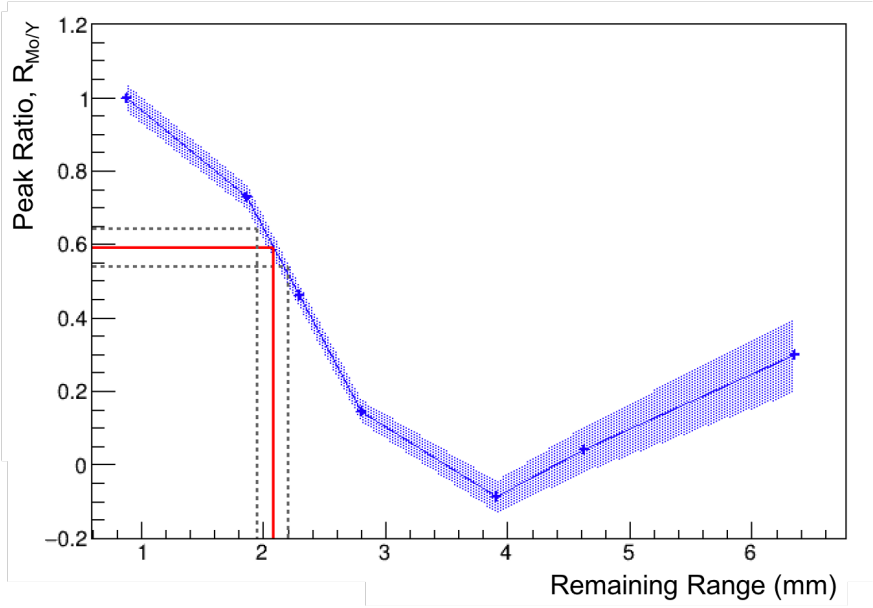

Figure 4.9: Demonstration of the range reconstruction procedure. The shaded blue area represents the results of peak ratio measurements for the the RS runs, which we use as a calibration curve for the relationship between the measured peak ratio, $R_{Mo/Y}$, and the remaining range of the beam. The horizontal red line and dotted black lines represent the measured peak ratio in the PMMA runs, which is projected against the calibration curve. The vertical red line and dotted black lines represent the beam range and associated range uncertainty that is extracted using this method. In this example, for a measured ratio of 0.59(5), a range of 2.24 mm is extracted, with an associated range uncertainty of 0.17 mm

PMMA runs in the sensitive region of $R_{Mo/Y}$ are summarized in Figure 4.10. Note that the runs whose theoretical remaining range was predicted to be larger than 4 mm were excluded from this portion of the analysis as they did not fall within the sensitive region. The average deviation of the reconstructed range from the predicted range in the sensitive range is 0.13(22) mm, and the standard deviation of the residuals is 0.18 mm, demonstrating that the uncertainty of HTM RV is very small, and far better than 1 mm, for any beam setting in which the proton beam targets the HTM within its sensitive range. Thanks to the combined effect of the composite marker and the improved detection setup and powerful data acquisition system we were able to demonstrate the clear detection of the characteristic gamma rays emitted by the HTM. Different from Burbadge et al (2) the HTM was embedded in a PMMA phantom this time, demonstrating the clinical ability

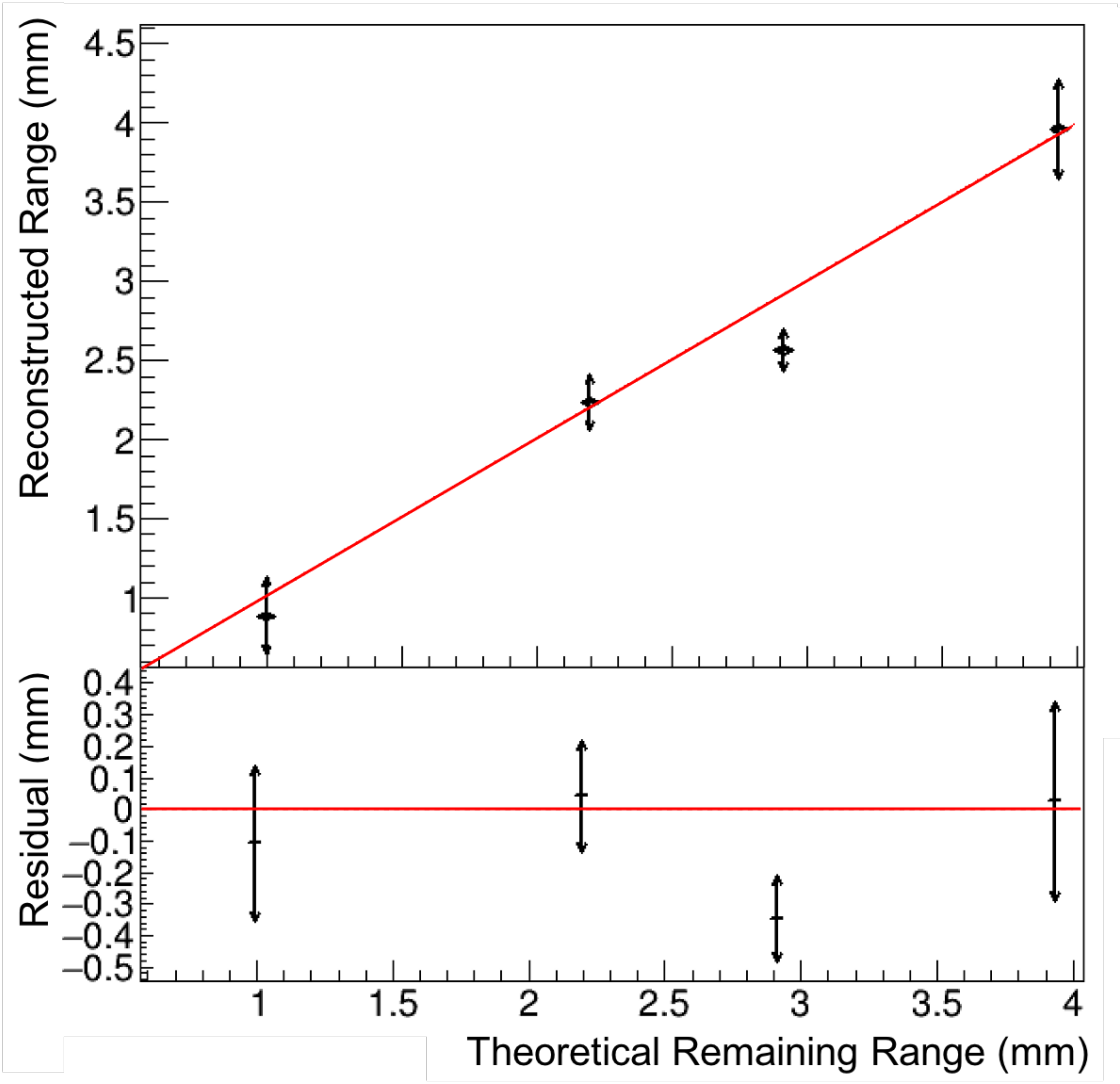

Figure 4.10: Results of range reconstruction compared with the predicted remaining range of the beam. The red line represents the ideal case in which the reconstructed range corresponds exactly to the predicted remaining range. The residuals of the experimental measurements relative to the ideal case are plotted below.

of our method, for the first time.

4.5 Conclusion

In our follow-up experiment we used a composite HTM and HPGe detectors with higher energy resolution to improve our sensitivity. With these advancements we were able to reconstruct the range with a composite HTM containing Y and Mo embedded in a PMMA phantom for various proton beam energies. The measured remaining ranges were found to be within 0.13(22) mm of the expected values on average, with uncertainties much smaller than other range verification methods currently being considered.

Chapter 5

Extension to Heavy-Ion Therapy

5.1 Introduction

This chapter has been adapted from Kasanda et al. (4) in accordance with the IOP Publishing Author Rights Policy for subscription articles.

In the work presented in this chapter, we investigate the application of HTM RV, to heavy-ion therapy. In extending the method to heavy-ion therapy, we must first identify new candidates for HTM materials, since the signals observed in molybdenum are specific to nuclear interactions with a proton beam. For the experiment discussed in this work, ^{16}O was used as the primary beam. While ^{16}O is not currently used for clinical irradiation, it shares many of the same benefits as the clinically-common ^{12}C, and is of particular interest in the treatment of radioresistant hypoxic tumours ((89)). Treatment planning with ^{16}O is an area of active research interest (21).

Table 5.1: γ rays of interest originating from interactions between the ^{nat}Ag target and the ^{16}O beam. This information includes the energy of the emitted γ ray (E_γ), the half-life of the isotope responsible for the emission of the γ ray of interest ($T_{1/2}$), the nuclear reaction from which the γ ray originates, the relative intensity of the emitted γ ray (I_γ) (86),and the maximum cross section for the nuclear reaction (σ_{max}) according to PACE (84; 83).

E_γ (keV)	Parent $T_{1/2}$ (s)	Origin Reaction	I_γ	σ_{max} (mbarn)
1256.68	53.5	^{107}Ag(^{16}O,x)^{112}Sb$\rightarrow^{112}$Sn	93.14%	109
1299.92	209.4	^{107}Ag(^{16}O,x)^{114}Sb$\rightarrow^{114}$Sn	98.7%	210

5.2 Materials and Methods

5.2.1 Hadron Tumour Marker

Prior to the experiment, a number of stable isotopes were investigated to identify candidates for HTM RV with a ^{16}O treatment beam, based on the properties above. PACE4 code (83; 84) was used to calculate cross sections for ^{16}O incident on a large number of naturally abundant metal isotopes at several Bragg Peak energies. Any reaction products with a significant cross section in the relevant energy region were compared with NNDC data (85) to ensure that they would satisfy the half-life and γ emission requirements of an HTM, as described in Chapter 1.6.

Of all the metals investigated with this method, ^{nat}Ag, ^{nat}Sn, ^{nat}Ti, and ^{nat}Tl were identified as having favourable properties and were selected for investigation in this experiment. In addition, ^{nat}Au was included due to its utility as a clinical fiducial marker. Of all the HTM materials investigated, only ^{nat}Ag was found to produce delayed characteristic γ rays at sufficient intensities for further analysis. For the portion of the experiment investigating silver as an HTM material, the targets consisted of samples of 50 µm-thick ^{nat}Ag foils. Note that due to the larger stopping powers involved with heavier ion beams, the HTM foil used in this experiment is thinner than the one used in previous works (1; 2; 3) to minimize cross section averaging effects from beam energy loss in the HTM.

5.2.2 Experimental Facility

Data collection took place at the Single Event Effects Test Facility (SEETF) in the National Superconducting Cyclotron Laboratory (NSCL) at Michigan State University. This facility produces ion beams with energies as high as 170 MeV u^{-1}, allowing for measurements to take place in air instead of in vacuum. The ions are accelerated with a pair of coupled superconducting cyclotrons: a K500 and, subsequently, a K1200. (90),(91). Beam attenuation to the desired current was performed upstream of the K500 cyclotron to minimize the impact of the induced beam inhomogeneities at the target (90). The fully accelerated beam was guided through the A1900 superconducting fragment separator and delivered undegraded to the SEETF beamline. Beam energy and intensity measurements were made between irradiations using a Faraday cup inserted into the SEETF beamline upstream of the multi-purpose user setup. The ^{16}O beam used for this experiment was delivered with an energy per nucleon of 149.41(10) MeV u^{-1} and a beamspot FWHM of 2.4 mm.

5.2.3 Experimental Setup

In order to investigate the viability of our candidate HTM materials for application in heavy ion therapy with an ^{16}O beam, thin square foils of each material measuring approximately 2 cm×2 cm (much larger than the beam spot) were embedded within a block of PMMA to simulate both the degrading of the beam in tissue, as well as the background produced from tissue. The thicknesses of PMMA upstream and downstream of the foil were 26 mm and 10 mm, respectively. These targets were positioned 60 cm downstream of the vacuum window, in air, and mounted on a linear actuator rail as shown in Figure 5.1.

The actuator rail (Zaber, model X-LC40B1800-E08) was remotely controlled from the data collection room to move the targets approximately 2 m from the activation position in the beam line indicated in Figure 5.1 to the measurement position located between the two detectors. This

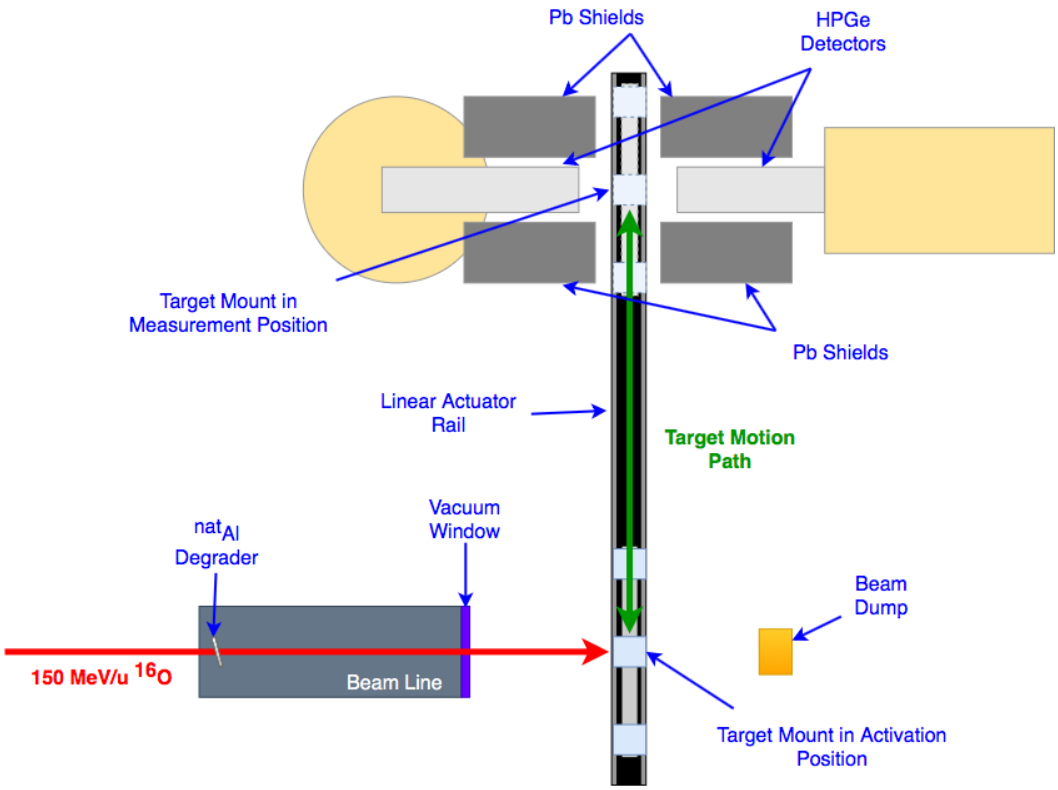

Figure 5.1: Sketch of experimental setup in the SEETF vault. The targets were mounted on the remotely-controlled linear actuator rail. While the beam was on, the target was located in the indicated activation position. When the activation was complete, the beam was switched off and the targets were moved remotely to the indicated measurement position for acquisition of the delayed γ-ray spectrum. The target mount could hold three targets. The sketch illustrates the case in which the centre target is being activated and measured.

transition occurred in the span of less than one second. Our detector system consisted of two High-Purity Germanium (HPGe) detectors: a GR1018 and a GR2018. The GR1018 was positioned facing the distal edge of the target (right side in figure), while the GR2018 was positioned opposite to it. The distance between the two detectors was 7 cm, with the target foil being slightly closer to the GR1018 detector in the measurement position due to the asymmetric dimensions of the PMMA block. Both detectors were powered with a CAEN DT5521EM HV power supply. Data acquisition was performed with a CAEN DT5780 Dual Digital Multi Channel Analyzer (MCA).

The purpose of the linear actuator rail was to allow the detectors and data acquisition system to

be positioned a safe distance from the beamline to avoid excessive neutron-induced damage to the detector crystals during the target activation period. Targets were activated for 150 s at an average beam rate of approximately 230 epA (average beam current in each run is listed in Table 5.3) in the position indicated in Figure 5.1, then moved into the measurement position between the two HPGe detectors and allowed to decay for 300 s. There were three target mounts on the linear actuator rail which could be remotely placed in the activation position one at a time. This allowed the experimenters to set up the targets to be activated for the subsequent three runs when entering the vault, reducing down time between activations. The dimensions of the target mount were chosen such that there was sufficient distance between the targets to avoid background contributions from neighbouring targets. ^{nat}Pb bricks were positioned near the detectors as indicated in Figure 5.1 in order to shield the HPGe detectors from background radiation produced by recently activated neighbouring targets and to further minimize damage and γ background from the ion beam.

The targets were activated with a 149.41 MeV/u beam of ^{16}O, which was degraded in the beamline to the appropriate energy, using ^{nat}Al degraders positioned upstream, in the beamline. The degraders were mounted in such a way that their angle relative to the beamline could be varied remotely using stepper motors, allowing incremental modification of the effective thickness of the degrader in the beam path. The degrader configurations used for the runs discussed in this work are summarized in Table 5.2. The PMMA blocks used to simulate tissue background in the target were allowed to decay for a minimum of one hour before re-use in order to minimize buildup of γ-ray background levels in subsequent runs, and fresh ^{nat}Ag foils were used for each activation. The degraded beam exited the SEETF vacuum window, a 75 µm zirconium foil, and entered the experimental setup, in air. Alignment of the beam axis was verified using the optical alignment system integrated into SEETF to ensure the ion beam would be centered on the target foils for optimal activation.

Prior to the experiment, the experimental setup was reproduced in LISE (92) in order to

Table 5.2: Summary of degrader configurations used for individual runs, and corresponding beam energies at foil entrance according to LISE calculations (92). The estimated residual range after foil according to SRIM (93) is also included.

Setting	Degrader Thickness (mm)	Degrader Angle (degrees)	Beam Energy at Foil Entrance ($MeV\ u^{-1}$)	Residual Range after Foil (µm)
1	1.8	43	17.2(12)	488
2	1.8	45	15.0(13)	339
3	2.6	0	13.4(15)	244
4	2.6	10	12.1(16)	174
5	2.6	15	10.2(18)	82
6	2.6	20	6.9(24)	20

calculate the entrance and exit energy of the ion beam in the target foil for each configuration and ensure the energy window for the reaction channel of interest was covered. The degrader positions indicated in Table 5.2 were selected in order to measure the response of the target to the beam at several different energies within the Bragg Peak in which the reaction channel of interest was calculated to be open, and to measure the HTM signal as a function of the entrance energy of the beam into the HTM foil.

5.3 Results

5.3.1 Data rates

The plot of γ intensity as a function of time shown in Figure 5.2 illustrates the jump in intensity and subsequent decay when the target is moved into the measurement position. The relatively constant background present in the activation period is the result of room background induced by the ion beam.

The maximum count rate measured during each of the runs analyzed in this work was 24(2) kHz for the GR1018 and 43(4) kHz for the GR2018, on average.

At these rates, the MC2A digitizer was able to store 100% of the tripped events to the disk.

Event pileup within the 1.5 µs processing time of the digitizer resulted in a 7% contribution to deadtime at the maximum count rate measured with the GR2018. Since, in the analysis, time windows were selected to individually optimize SNR for each peak of interest, the average deadtime contribution from pileup is much lower in practice. As an example, for the runs using degrader setting 1 as described in Table 5.2, the average deadtime for the GR1018 detector was 2.20% for the time window used to fit the 1257 keV peak and 1.32% for the time window used to fit the 1300 keV peak. For the GR2018, the average deadtime contributions from pileup are 4.35% and 2.74% for each of the two time windows, respectively.

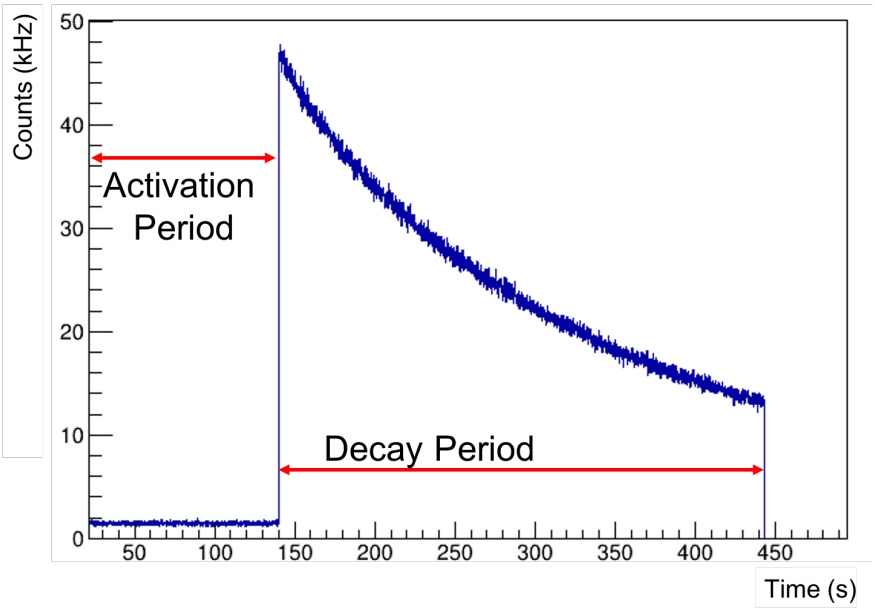

Figure 5.2: Gamma intensity in the GR2018 as a function of time for one run. The intensity remains low while the beam is on as the target is in the activation position. The sharp increase in intensity at 140 s corresponds to the moment at which the target is moved into the measurement position between the detectors. The decay of the activated target is then measured for an additional 300 s.

5.3.2 Experimental spectra

To detect the gamma rays of interest, energy and efficiency calibrations were performedfor the HPGe detectors using a ^{152}Eu source. The literature values for the γ-rays of interest are summarized in Table 5.1 and both are predicted to to be emitted in the decays following from reactions between naturally abundant ^{107}Ag and the ion beam. Both γ rays are emitted with high intensity through the β^--decay of the reaction products. Peaks were identified in our spectrum that corresponded to the literature values described in Table 5.1 in both energy and in half-life, and are only present in runs during which ^{nat}Ag foils were activated. The results are highly indicative of the identified peaks originating from the reactions of interest. Figure 5.3 illustrates the decay of both peaks of interest as a function of time, in comparison to literature values.

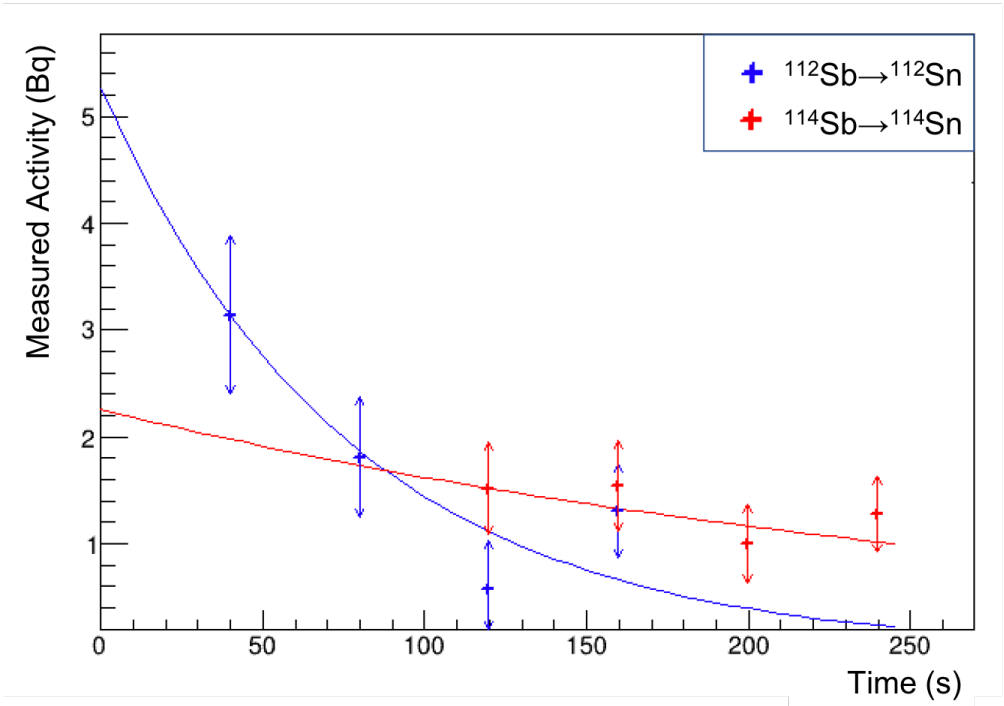

Figure 5.3: Decay of two peaks of interest as a function of time. The data points in this plot were obtained by summing all runs with different degrader positions in order to maximize statistics. The solid lines represent the theoretical decay curves for each isotope of interest, based on the known half-life of the isotope and normalized to the first data point in each series.

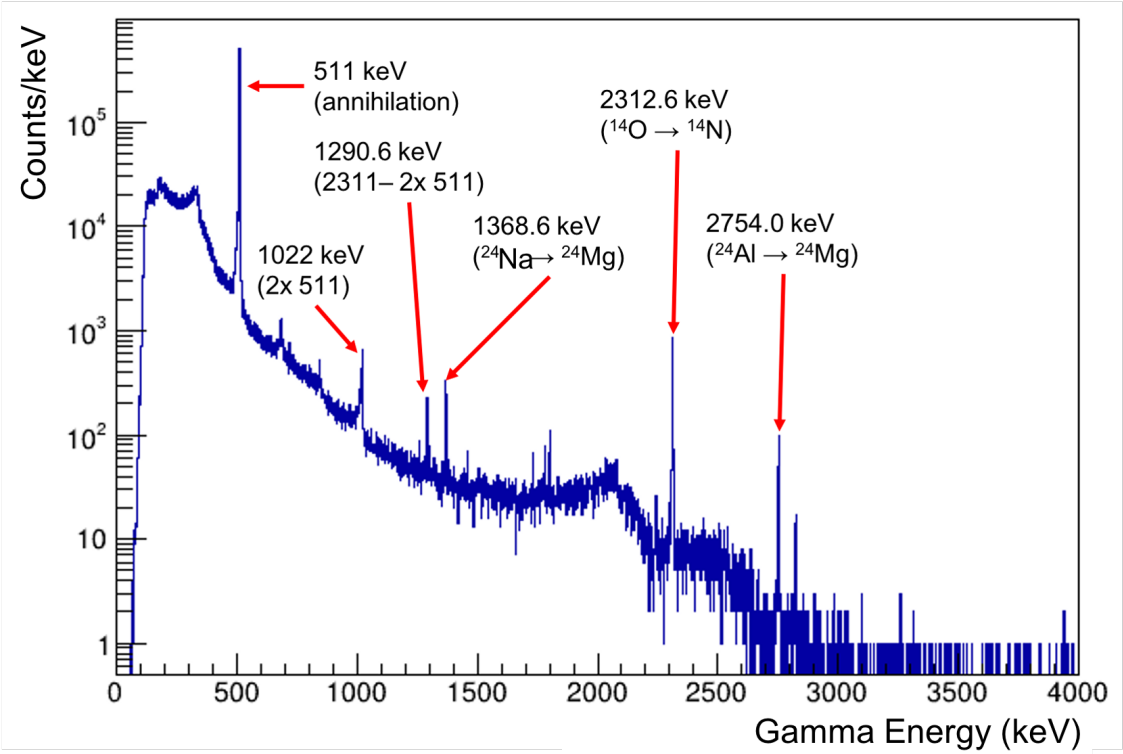

Figure 5.4: Delayed γ spectrum using time window optimized for 1300 keV peak for the run corresponding to a residual range of 244 µm after the foil. Prominent background peaks have been identified, including the sum-peak at 1022 keV and the double escape peak at 1290.6 keV.

In order to verify the half-lives of the isotopes emitting the γ rays of interest, the runs from all degrader settings described in Table 5.2 were summed together. Then, six time projections with durations of 40 s were taken at 40 s intervals, and the peaks of interest fitted in order to determine the average activity in each projection. Each time, the FWHM of the peaks was fixed to that of the large 1290.6 keV double-escape peak from the β^--decay of ^{14}O into ^{14}N (2312.593(11) keV $-$ 2$\times$ 511 keV) in order to achieve more consistent results. The peaks of interest were fitted as a doublet alongside the 1290.6 keV double escape peak for improved background estimation. In Figure 5.3, the first two time windows for the 1299.92 keV peak and the last two time windows for the 1256.68 keV peak have been omitted since the peak is not clearly visible above the background in these projections. The decay of the peaks of interest is compared against theoretical decay

curves for each isotope of interest, based on the known half-life of the isotope and normalized to best fit the data, indicating good agreement. Since the two peaks of interest are emitted with different half-lives and the background is large relative to the peaks, it was beneficial in the interest of maximizing the signal to noise ratio (SNR) to consider different decay time windows for each γ-ray of interest. By projecting delayed γ energy spectra acquired in different time windows, it was found that the best SNR was obtained for the 1256.68 keV peak by considering only γ rays emitted between 20 s and 80 s after end of the activation period. Similarly, for the 1299.92 keV peak, the selected time window included γ rays emitted between 100 s and 220 s after end of the activation period.

The resulting γ-ray energy spectrum from one of the runs in which the peaks were maximized, using the time window optimized for viewing the 1299.92 keV peak, is shown in Figure 5.4. In this spectrum showing the full range of energies measured by the detector, the 1299.92 keV peak is too small to be labeled.

Focusing on the energy region of interest, Figure 5.5 shows the results of fitting the peaks of interest with a Gaussian function. As with the half-life measurements in Figure 5.3, the FWHM of the peaks was fixed to that of the large 1290 keV background peak from PMMA in order to improve fit results, and the peaks of interest were fitted alongside this same background peak for improved background estimation.

The results for the fitted peak area for the γ-rays of interest at each setting are listed in Table 5.3.

5.3.3 Normalization

in order to compare measured gamma rays to expectations, it is helpful to normalize our fitted peak areas to the beam current. Throughout the experiment, the neutron flux incident on a sensor within the vault, which is strongly correlated with beam rate, was monitored and compared

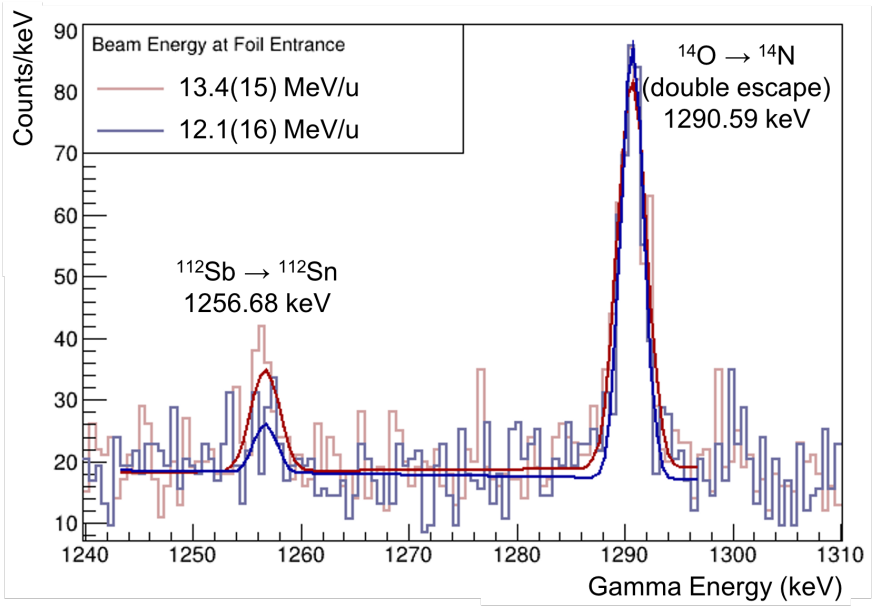

(a)

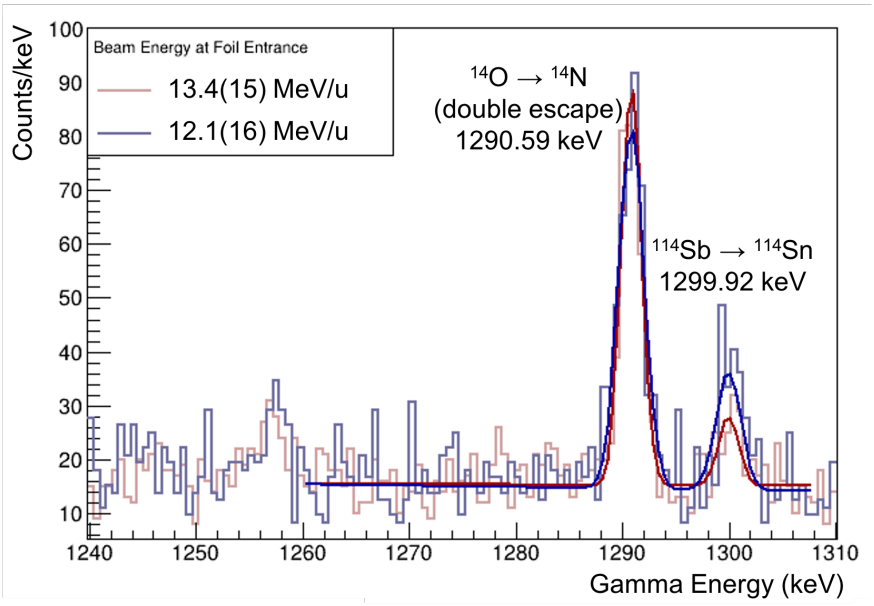

(b)

Figure 5.5: Comparison of fitted peaks for two neighbouring beam energy settings, illustrating the change in peak area with a small change in beam energy. Fits were calculated using 1290 keV background peak as basis for FWHM, to improve fit.(a) 1257 keV time window. (b) 1300 keV time window. The illustrated spectra contain data from a single HPGe detector.

Table 5.3: Summary of normalized and fitted peak areas for each setting used, along with the average beam current incident on the foil during the run, to which the fitted peak areas have been normalized.

Setting	Fitted Peak Area		Average Beam Current on Foil (epA)
	1257 keV	1300 keV	
1	17(13)	22(17)	220(5)
2	40(16)	0(15)	257(6)
3	110(19)	69(16)	256(6)
4	71(15)	100(15)	208(5)
5	14(17)	76(16)	229(5)
6	6(17)	23(16)	217(5)

with intermittent Faraday cup readings of the ^{16}O beam in order to estimate the beam intensity throughout the measurement. A linear fit of the Faraday cup readings as a function of the background-subtracted neutron flux yielded a slope of $2.59(13) \times 10^{-8}$ eA per mRem/h. A plot of the measured neutron flux (in mRem/h) during a section of the experiment is shown in Figure 5.6. The integrated neutron flux during the activation period of each run was used as a normalization factor in Figure 5.7. All peak areas are scaled to the neutron flux in the runs using degrader setting 1, as defined in Table 5.2.

5.4 Discussion

5.4.1 Range Verification through Peak Identification

Measuring the peak areas from the γ rays of interest enables us to plot the cross section for the ^{107}Ag(^{16}O,x)^{112}Sb and the ^{107}Ag(^{16}O,x)^{114}Sb reactions as a function of residual beam range, see Figure 5.7a. This conversion took into consideration detector efficiency estimations, decay rates of relevant reaction products, γ-ray emission probabilities, and beam rate estimations. Good agreement of the energy dependence of the reaction channel between the calculation and the experimental results is observed. However, the measured cross sections were found to be

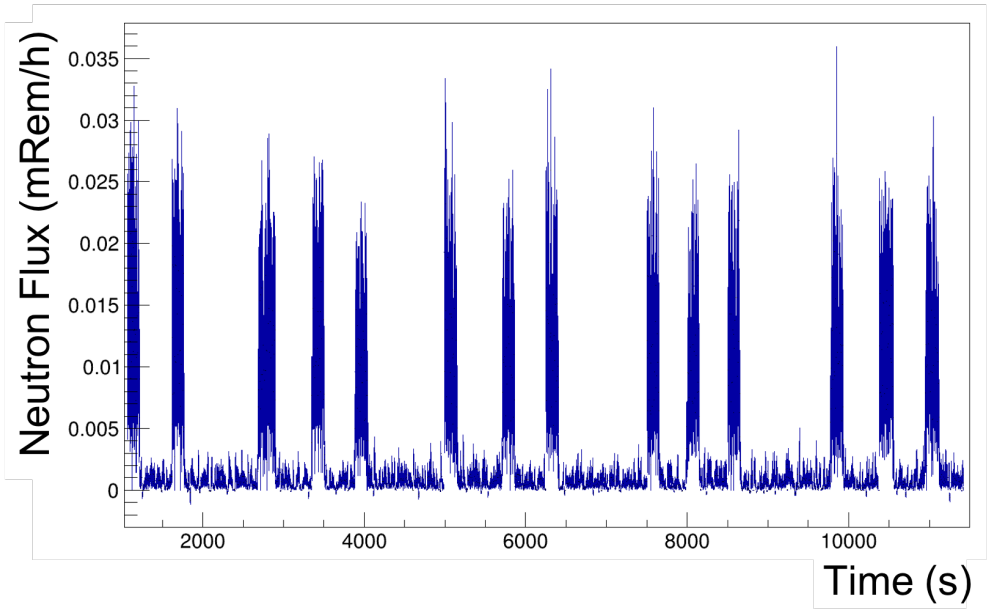

Figure 5.6: Measured neutron flux (in mRem/hr) as a function of time (in seconds) for a segment of the experiment, illustrating the pattern of activation and decay employed during this experiment. The larger time segments between activations correspond to the occasions the experimenters entered the vault to install fresh targets.

significantly lower than those predicted by PACE (83),(84) by a factor of 0.081.

The calculated normalized peak area of interest for each degrader configuration indicated in Table 5.2 was then plotted against the corresponding residual beam range in Figure 5.7b. In this figure, one can see that the peaks of interest appear and subsequently disappear entirely within the span of 500 µm. This is in and of itself a sub-milimetre measure of beam range. If the marker were to be positioned in the patient such that ideal irradiation would result in maximum activation of the HTM, observation of the peaks of interest, regardless of intensity, would be indicative that the tumour has been irradiated appropriately within 0.5 mm. This peak identification method is a possibility for heavy ion therapy due to the much larger stopping powers relative to proton therapy. In contrast, previous investigations of this method for proton therapy found that the reaction channels for the peaks of interest opened and closed over the span of several millimeters for a foil target similar to the one used in this experiment (1). The beam energy range over which

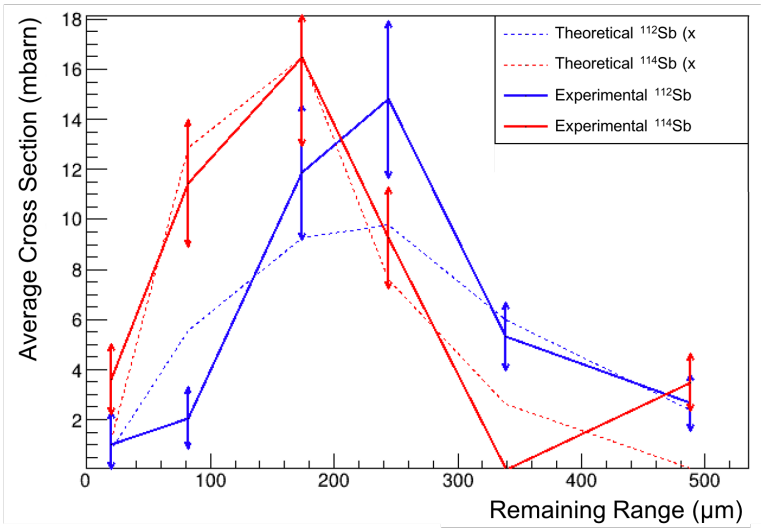

(a)

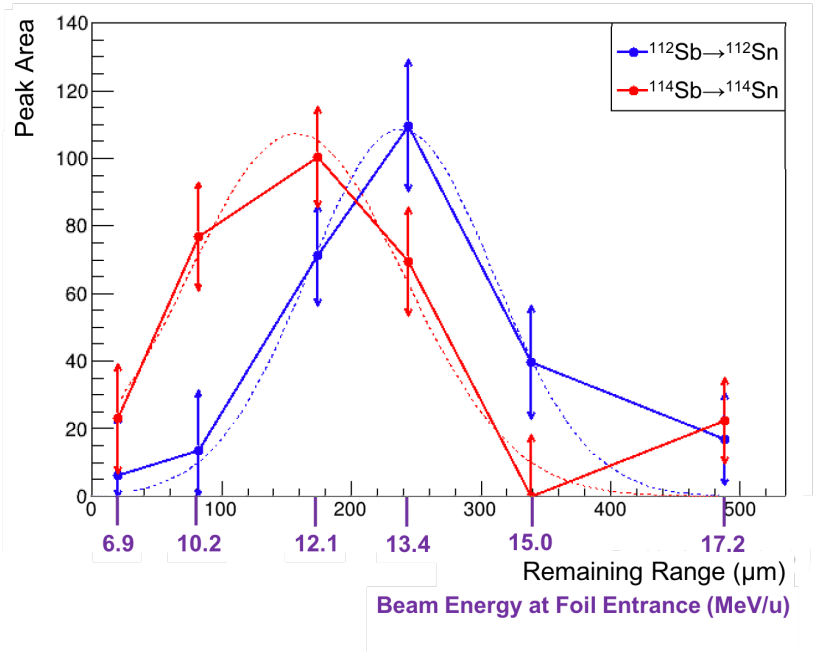

(b)

Figure 5.7: (a) Experimentally measured average cross sections in the marker as a function of remaining range for both channels of interest, compared with their theoretical counterparts according to PACE calculations (84; 83). The theoretical cross sections have been normalized to the maximum of the experimentally measured cross section for the ^{107}Ag(^{16}O,x)^{112}Sb reaction to better align with the scale of the experimental values. The normalization factor was 0.081. (b) Normalized (see Section 5.3.3) peak intensities for all 50 µm Ag+PMMA runs, as a function of remaining beam range (calculated according to LISE (92)). Corresponding beam energies at foil entrance are indicated in green. Dotted lines indicate a gaussian fit of the data points for each peak.

the channels of interest are open is also highly dependent on the thickness of the marker used, allowing the precision of the verification method to be adjusted based on the precision of marker positioning and irradiation techniques. PACE calculations of the average cross sections for the reactions of interest, fitted with a Gaussian curve, are plotted as a function of the remaining range of the beam beside the marker in Figure 5.8, to illustrate the shape of the excitation function. In this case, as in Chapter 4, we consider the remaining range of the beam in the tissue immediately beside the marker, as opposed to the remaining range of the beam behind the marker.

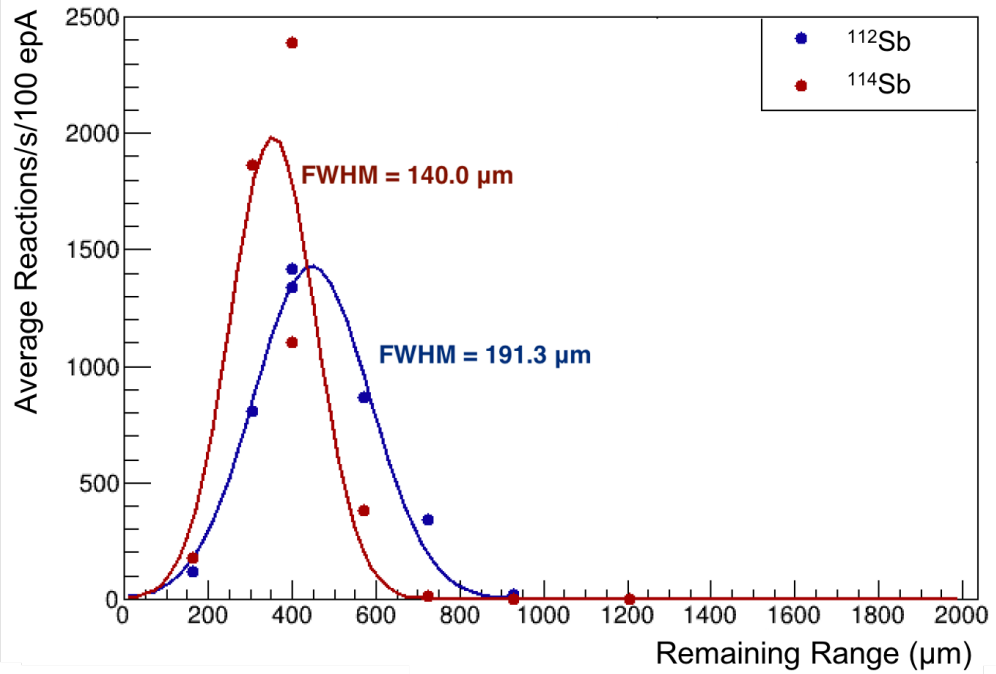

Figure 5.8: Calculation of cross sections for reactions of interest in a 50 µm-thick foil of natural silver. The cross sections have been fitted with a gaussian curve to illustrate the rough shape of the excitation function, and are plotted as a function of the remaining range beside the marker.

5.4.2 Range Verification using intensity of single peak

If the maximum intensity of the peak is known prior to treatment, the shape of the excitation function can be used to estimate range uncertainty with additional precision, using only a single

peak. First, for the data obtained in this experiment, the peak area as a function of remaining range is assumed to be Gaussian. These Gaussian fits are shown in Figure 5.7b. With a higher-precision calibration and more data points, this assumption may not be necessary in a clinical setting. Second, the maximum expected intensity of the peak of interest must be known. This may be accomplished with Monte Carlo simulations.

If the marker is positioned such that successful irradiation of the target volume results in the area of the peak of interest being maximized, then the lower bound of the measured peak area can act as a measure of the range uncertainty, indicating at an upper bound on the difference in distance from the targeted depth that the beam has reached within the patient. For example, looking at the 1257 keV peak in Figure 5.7b, a the lower bound of a measurement of 60% of the maximal intensity (indicated in green) with an associated uncertainty of 20% corresponds to points on the Gaussian fit located at a distance of approximately 100 µm from the mean (indicated in blue). Ignoring the uncertainty associated with our measurement since the quality of the calibration curve is not limited by clinical statistics, this measurement indicates that we are within $\pm$ 100 µm of the targeted depth. This method may have applications as a relative range measurement for different energy layers used in PBS delivery.

Figure 5.10 indicates the results of this procedure as a function of measured peak area relative to the maximum as well as the associated uncertainty. Once the lower bound of the measured peak area reaches zero, the range uncertainty using this method goes to infinity since we do not see a peak in this scenario.

Making use of the impact of HTM dimensions and densities on beam energy loss in the marker, the range of the Y-axis of Figure 5.10 can essentially be optimized to best match the range sensitivity of the clinical setup by adjusting the composition of the HTM.

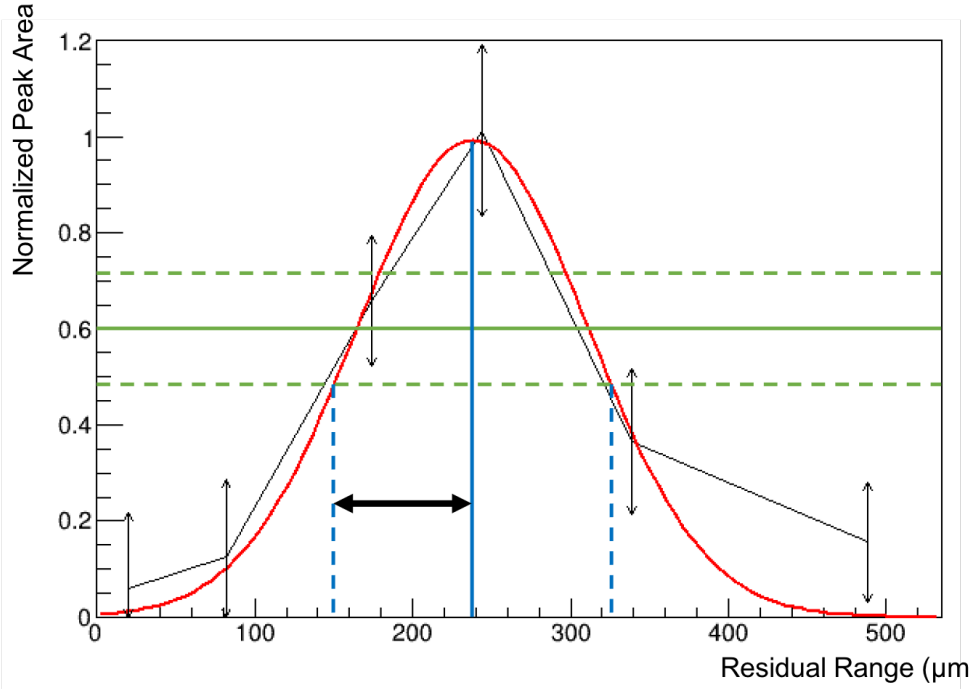

Figure 5.9: Sketch of method for estimating range uncertainty with a single peak. The green lines indicate a measurement of the peak area of 60% of the maximal value, with an associated uncertainty of 20%. The black arrow indicated the resulting upper bound on the distance from the targeted depth

5.4.3 Range verification using ratio of two peaks

One disadvantage of range verification using peak identification is the need of an absolute measurement in order to have meaningful interpretation of the observed γ-ray intensity. To avoid the issue of normalization and any assumptions regarding the beam delivery rate, it is helpful to consider the ratio of the two peaks of interest to one-another, R_{Ag}. This value, which is defined as the 1257 keV peak area divided by the 1300 keV peak area, is independent of beam current, dose delivered, and detector efficiency (ignoring slight difference in detection efficiency of two peaks, since they are similar in energy). It is however dependent on marker thickness, as well as the timing of the dose delivery and γ-ray measurement due to the very different half-lives of the two peaks.

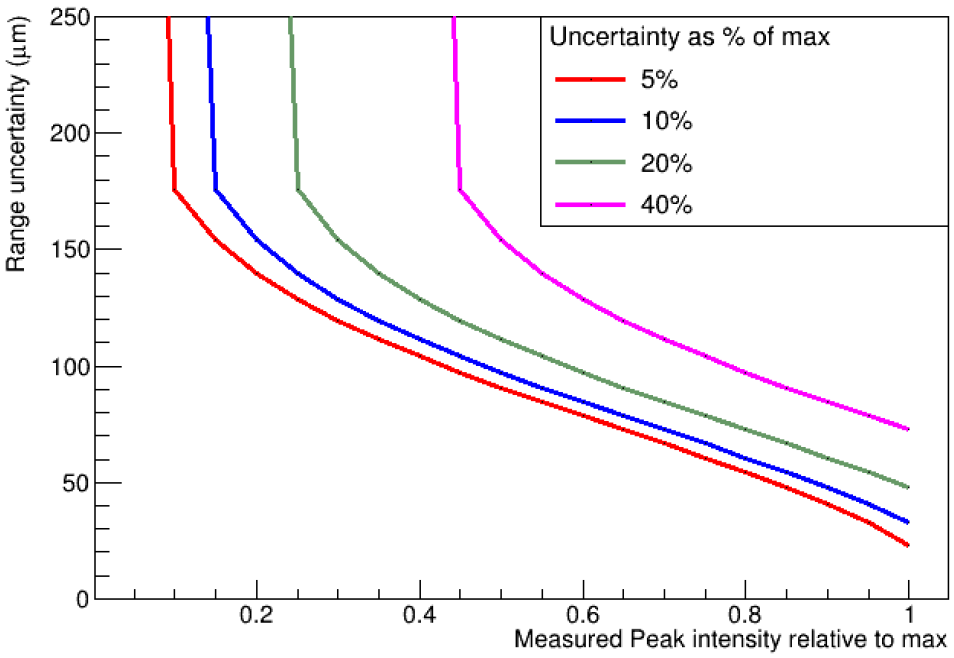

Figure 5.10: Uncertainties in range for several assumed uncertainties in peak area. These values correspond to the size of the black arrow in Figure 5.9 for different measured peak areas and associated uncertainties.

The nature of the excitation functions of these two competing reaction channels is such that the channels open and close within a small energy window, with their respective maximal cross sections occuring slightly offset in energy from one another. This makes the ratio of the two peaks highly sensitive to small shifts in the remaining range of the beam, making it ideal as a range verification parameter. A plot of R_{Ag} as a function of the residual range of the beam after the marker is shown in Figure 5.11. The experimental values are indicated in black, but the two highest-energy points have been omitted because the 1300 keV peak is not detectable in our experiment. The solid blue line corresponds to a theoretical prediction of the peak ratio based on PACE cross sections and known γ-ray intensites. Note that although calculations of the cross sections for the reactions of interest reported in Figure 5.7a were over an order of magnitude lower than predicted by PACE, the ratio of the two peak areas is independent of this factor and fits within our experimental uncertainty without requiring any adjustments in magnitude.

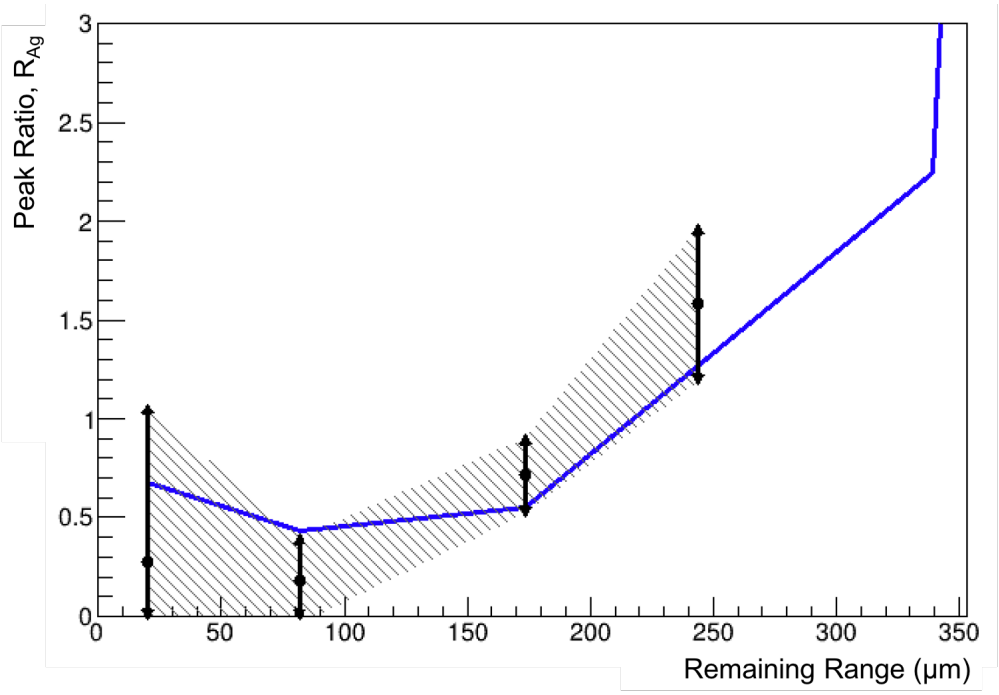

Figure 5.11: Peak ratio, R_{Ag} for all Ag+PMMA runs, as a function of remaining beam range (calculated according to LISE (92)). The solid blue line represents a theoretical prediction of the peak ratio based on PACE calculations of the reaction cross sections and known γ-ray intensities. Experimental points for which the 1300 keV peak was very small have been omitted due to large uncertainties.

5.4.4 Impact of realistic marker dimensions

In this work, 50 µm-thin foils of $^{\mathrm{nat}}$Ag were used to determine the cross sections of the beam reaction with the HTM as a function of beam energies in the range of the Bragg peak. In a clinical setting, the HTM would have the dimensions of a typical fiducial marker, potentially degrading the achieved precision of our method. Based on the calculated cross sections we have thus simulated the energy loss of the beam in a fiducial marker of 1 mm thickness. We further assumed that the marker contains 10% $^{\mathrm{nat}}$Ag by weight, homogeneously distributed in PMMA. These parameters were chosen such that the total mass of $^{\mathrm{nat}}$Ag in the beam path is the same for both markers, resulting in similar statistics if a pencil beam is centered on the marker. Figure 5.12 illustrates the resulting effect on the predicted γ ray intensities when using a fiducial marker.

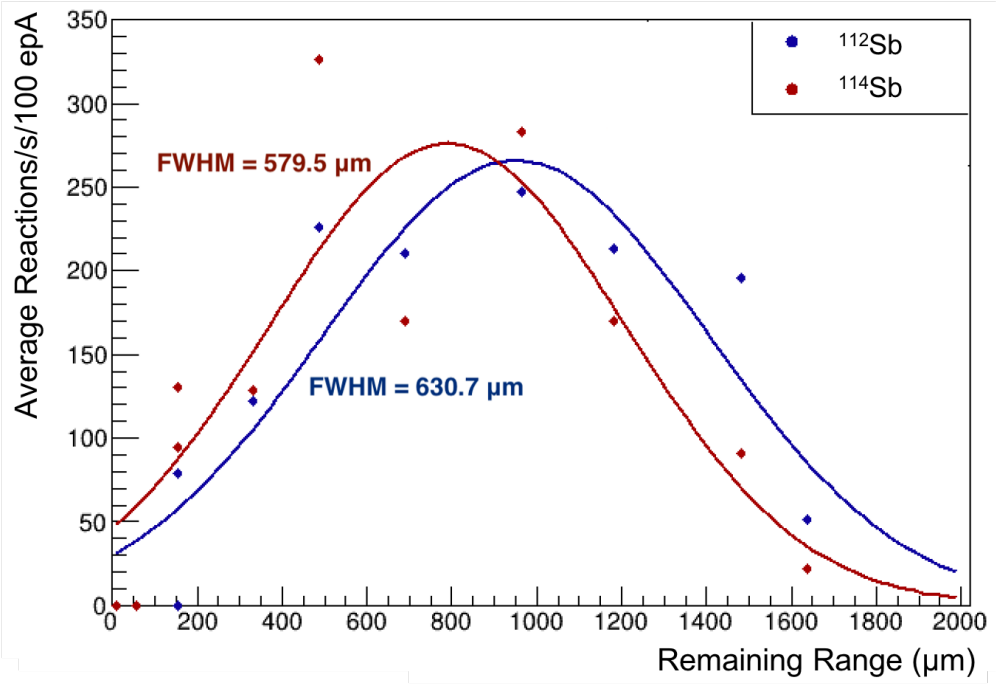

Figure 5.12: Calculation of cross sections for reactions of interest in a 1 mm-thick fiducial marker containing 10% natural silver diluted in PMMA, according to LISE(92) calculations of energy loss in the target and PACE cross section calculations. As in Figure 5.12, the cross sections have been fitted with a gaussian curve to illustrate the rough shape of the excitation function. The cross sections are plotted as a function of the remaining range beside the marker, as described in section 5.4.1. NOTE: although the average cross section in this example is smaller due to the active material being diluted, the marker itself is thicker by a factor of 20.

As shown in Figure 5.12, the reduced density and increased thickness of the marker result in an increased spread in the excitation function as a function of remaining beam range. It is worth noting that in this example the beam is very easily stopped within the marker. Therefore, it is helpful to once again consider the remaining range of the beam in the tissue immediately beside the marker, as opposed to the remaining range of the beam behind the marker. Since the marker used in obtaining this plot is 1 mm thick, all points below 1000 μm on the x-axis represent beam settings for which the beam will be stopped inside the marker. The Gaussian fits of the excitation functions indicate that the FWHM is increased by a factor of 3.29 and 4.13 for the 1257 keV and 1300 keV peaks, respectively, relative to the marker dimensions used experimentally, illustrated

in Figure 5.8. In a clinical scenario, performing three measurements under slight variation of the beam energy will reduce range uncertainties using this peak detection method to uncertainties of about 1 mm, or better.

Even higher precision can be achieved using the ratio method established in previous works (1; 2). Again, the use a fiducial marker will change the results compared to a thin foil. While in this experiment statistics were still very limited due to the use of small HPGe detectors, the true ratio of γ rays as a function of beam energy can be precisely measured, in principle. We here assume that this ratio is given by the ratio of the two fit functions in Figure 5.12. As in Burbadge et. al. (2), we take this curve to be the "true" R_{Ag} function for the purpose of discussing the limit of the precision of the range verification measurement, and assume that the error bars for this function are negligible. As noted in Burbadge et. al. (2), these values may need to be changed following a dedicated measurement of the cross sections for the reactions of interest, but the impact of these changes on the precision of the range verification measurement are expected to be small.

Following this, we can project any ratio measurement within the region of interest with an associated uncertainty to extract the remaining range of the beam and the associated range uncertainty. In this example, we choose a measured ratio of 1.4, as it falls within the region of R_{Ag} with the steepest slope (i.e the most sensitive region). An uncertainty in the ratio measurement of 25% is assumed, as this is on par with the experimental uncertainty that was achieved in this region. As illustrated in Figure 5.13, projecting this ratio against the theoretical R_{Ag} function yields a range measurement of 600 µm, with an associated range uncertainty of $\pm$290 µm.

In this experiment only a small set of two HPGe detectors was used. In a clinical setting, an array of HPGe detectors could be installed, covering a solid angle of about 20%. If we assume the number of particles per Gray delivered in Oxygen therapy to be comparable to that of Carbon ion therapy, the statistics achieved in this experiment are equivalent to those that could be achieved clinically with an array of HPGe clovers arranged to provide a geometrical efficiency of 20%, and

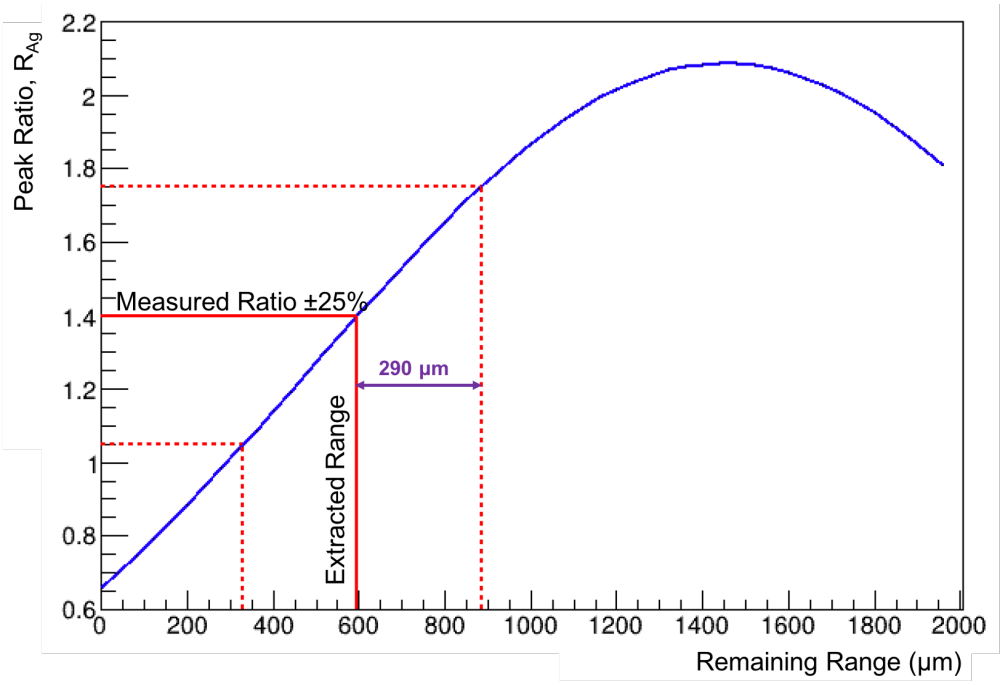

Figure 5.13: Illustration of sensitivity limit of range verification method. The blue line represents an estimation of the theoretical ratio function in a fiducial marker of realistic dimensions as depicted in Figure 5.12. The red horizontal lines represent the measured ratio and associated uncertainty as described in Section 5.4.3. The red vertical lines represent the extracted beam range and associated uncertainty.

with 3.5 Gy of dose delivered (approximately 2.45×10^9 particles). Hence, our work demonstrates that both the peak intensity method as well as the ratio method using a Ag fiducial marker will result in precise sub-millimeter range verification in heavy ion beam therapy.

It should be noted that, unlike PET RV, which can provide three-dimensional information on the beam path within the patient, HTM RV is limited to a high-precision measurement of the residual range of the beam relative to the HTM position. The two techniques could be used in conjunction in order to gain the benefits of both. Further work expanding to other ion beams may make this method clinically relevant.

5.5 Conclusion

In addition to our work with proton beams (1; 2), we expanded out HTM range verification method in hadron therapy to an ^{16}O beam with silver fiducial markers, and presented first proof-of-principle measurements. The energy dependence of the activation cross section is large: with a 50 µm thick Ag HTM, the opening and closing of the reaction channel happens in the span of only 500 µm residual range. Additionally, the theoretical limit of the range uncertainty that can be extracted using this method with a fiducial marker of realistic dimensions was determined to be approximately ± 290 µm . Our method comprises a simple alternative to PET and Prompt Gamma range verification, with the advantage of being independent of Monte-Carlo simulations. It relies only on the knowledge of the position of the HTM relative to the tumour, provided by a CT scan. Using the ratio of two appropriate reaction channels, e.g. ^{107}Ag(^{16}O,x)^{112}Sb and the ^{107}Ag(^{16}O,x)^{114}Sb reactions as discussed here, results in the method being independent of beam delivery variations. Future work will include dedicated cross section measurements for the reactions of interest.

Chapter 6

Outlook of Clinical Translation

The work presented in this thesis details the process of developing a novel method of HTM RV from its beginnings as an idea needing to be demonstrated through simulation to be feasible, to its current state. The method of HTM RV has been shown experimentally to yield absolute measurements of beam range on a sub-millimeter scale in both PT and HIT.

In a future clinical application of HTM RV, we envision that a metal HTM would be implanted close to the CTV prior to treatment, a process which is already in clinical practice (67). Due to the high atomic number of the HTM, it will be clearly visible in a CT scan, which is often performed prior to PT to facilitate treatment planning. This CT image will give the distance from the HTM to any point in the CTV, and the HTM can be used to align the patient to the beam. To achieve the highest sensitivity, the HTM should be positioned such that the targeted residual range falls in the most sensitive region of the calibration curve, as discussed in Section 2.3.4. When the fraction delivery starts, the expected beam range can be compared to the delivered beam range and the result can be used to abort beam delivery if it exceeds a set safety margin. It should be noted that the HTM RV method can only provide a range estimate of the proton beam at the location of the HTM, not a 3-dimensional verification of the treatment field. It can, however, be combined with

other 3D methods, *e.g.* RV with PET, albeit at lower resolution.

HTM RV provides a direct measurement of the energy of the treatment beam at the HTM, which can be used to estimate the remaining range of the beam. Although there is inherent uncertainty in the conversion from beam energy to remaining range, the range of the beam after the marker would be small, on the order of milimeters. Therefore, this range can be estimated with relatively high precision based on simulations and calibration measurements, and this estimation is independent of any uncertainties in tissue stopping powers upstream of the HTM.

Before this method can be considered as clinically relevant, several considerations that are outside the scope of this Ph.D thesis must be addressed. First, in all the experiments presented in this work, the precision of the RV measurement was limited by statistical uncertainties. In a clinical setting, the calibration curve that would be used to extract the range of the beam does not need to be limited to statistics achievable in a clinical fraction. Performing dedicated cross section measurements for candidate HTM reactions of interest would have a dramatic positive impact on the precision of the range measurements yielded by HTM RV. For optimal precision, these calibration measurements would need to be performed on a marker of clinical dimensions, and would be specific to the beam delivery system with which they were acquired, but do not require the participation of a patient.

In Chapter 5, the difference in the range determination when considering an HTM of realistic clinical dimensions as opposed to a thin foil was explored through calculations. The dimensions of a clinical HTM would be similar to those of solid fiducial markers used in PT treatment planning of ocular (41), liver (94) and prostate cancers (62; 64), which are already clinically employed and are already being studied in the context of in-vivo proton RV (43). Although the impact of a larger HTM is much more dramatic in HIT than in PT due to the higher stopping powers, it is still relevant in PT and should be investigated experimentally. Particularly in the case of HIT, beam energy loss in the HTM results in a larger range of beam energies contributing to the HTM

activation, causing losses of sensitivity associated with cross section averaging within the marker. These losses may be mitigated by creating a clinical HTM composed partially of less dense materials such as tissue-equivalent plastics or even liquids. These materials would reduce the overall density of the HTM, limiting beam energy losses in the marker. When making the transition to a larger HTM of clinically realistic dimensions, the density of a the HTM must be carefully considered in order to minimize sensitivity losses, while maintaining sufficient statistics to precisely extract the peak ratio and ensuring sufficient CT contrast relative to the surrounding tissues. Additionally, the composite HTM used in the experiment described in Chapter 4 was created by arranging foils of the selected materials in tiles. A more realistic clinical composite HTM would be made of a homogeneous blend or alloy of candidate materials to avoid uncertainties associated with the position and orientation of the HTM within the patient. The effect of artifacts on planning CT images and dose shadowing from beam perturbations, which can lead to changes to the planned dose, are already being investigated for various fiducial markers (62; 63; 64; 41; 65; 66), and will need to be carefully evaluated for each HTM. The toxicity and biological half life of the HTM in the human body will also need to be characterized.

Although the exact geometries and implantation techniques for the HTM are subject to future studies, it is clear that HTM RV only allows direct RV for settings in which the beam interacts with the HTM. Multiple markers can be strategically placed to cover the most critical angles during treatment, defining calibration points for RV with sub-millimetre precision. As an example, multiple fiducial markers have been successfully applied for image-guided external radiation therapy for prostate cancer (95), allowing monitoring of inter-fraction motion of the prostate bed and improving accuracy of the treatment delivery. Replacing those fiducial markers with HTM material will, in addition, allow range calibration for prostate cancer, allowing, for instance, to verify the translation of CT grey scales to pelvis bone and soft tissue stopping power ratios. The results can then be used to fine-tune the treatment plan also for regions not directly covered by the HTM.

The HTM RV technique would pair well with the irradiation of thoracic cancers using the deep inspiration breath hold (DIBH) technique, where the timing of the delivered dose is already limited by the patient's breathing cycle (96). In this type of treatment, the HTM signal could be measured between beam pulses to provide real-time verification of the treatment without lengthening the total treatment time. The ratio could also be included in the safety interlock system, immediately terminating the treatment when the detector does not register the correct signal.

Tissue inhomogeneities are a subject of significant consideration in RV for PT and HIT that has not been taken into account in this work. Future experimental investigations of HTM RV should make use of a realistic tissue phantom to study the impact of tissue composition fluctuations in the beam path on the precision of the range measurement. Once the method has been tested in clinically realistic conditions, the incorporation of HTM RV into a clinical workflow should be established on a more technical level. The signal from the HTM can be recorded in the time frame of a treatment fraction. As no time-intensive simulation is necessary for the analysis of the remaining range, the results of HTM RV can be taken into account for the delivery of a subsequent fraction, not altering the present work flow dramatically. Alternatively, during a fraction, only a small part of the prescribed dose could be delivered, the HTM data analysed, and the remaining portion of the fraction adjusted if necessary by a criteria, e.g. the remaining range is outside of the applied treatment margins. While this method will delay the work flow, it may ultimately lead to smaller prescribed field margins and therefore to a smaller volume of healthy tissue being irradiated.

The arrangement of the γ-ray detector array relative to the beam and the patient, and the timing of the measurement in regard to beam delivery will both have an important impact on the statistics that can be achieved, and the resulting precision of the range measurement. The solid angle coverage of the γ-ray detector array that can be achieved in a treatment room (with cost efficiency in mind) must be considered in tandem with the statistics that can be achieved within a clinical fraction when planning a clinical implementation of HTM RV. In the experiment discussed

in Chapter 4, the use of HPGe detectors was crucial in the detection of the HTM signal over the simulated tissue background. However, HPGe detector crystals are susceptible to damage from the high neutron doses that are produced in the vicinity of the treatment beam during fraction delivery. In our experiment, this damage was mediated by positioning the detectors several meters away from the beamline and quickly moving the HTM target to the detectors following activation, using a linear actuator rail. This solution is unfortunately not practical in a clinical scenario where the HTM is implanted in a patient undergoing treatment. Therefore, alternative methods of protecting the detectors from the beamline during fraction delivery must be considered.

The experiments discussed in Chapters 3 and 4 took place at TRIUMF's PTRC, which uses a passively scattered proton beam. Passive scattering is a method of spreading out the Bragg Peak to ensure full coverage of the CTV. An alternative beam delivery method, commonly referred to as pencil beam scanning (PBS), allows for more conformal CTV coverage by using steering magnets to deliver the beam to each voxel of the CTV, one at a time (15). This method is the clinical standard in part because it permits treatment plans considering multiple beam directions converging on the CTV, resulting in further healthy tissue sparing. When applied in the context of HTM RV, the advantages and drawbacks of PBS beam delivery must be examined by simulation and experiment. The reduced energy spread of each individual pencil beam compared to the spread-out Bragg Peak delivered by a passively scattered beam will minimize cross section averaging in the HTM, potentially improving the precision of the range measurement. Additionally, a reduced γ-ray and neutron background is expected during treatment compared with passive scattering systems. However, the statistics used in the range measurement might be significantly lower.

FLASH beam delivery is an up-and-coming modality for radiation therapy, in which the entire fraction dose is delivered at ultrahigh dose rates in the span of a few seconds or less (97). It has been shown in conventional radiation therapy using X-rays to result in an improved therapeutic ratio. The first clinical trials for FLASH PT are underway (98), and FLASH with heavy ions is

being investigated (99). Due to the technical constraints associated with translating PBS delivery to the speeds required for FLASH dose rates, passive scattering systems are once again on an upward trend. Because the full treatment dose is delivered in only 1-3 practically instantaneous fractions, the room for error in the overlap of the treatment field with the CTV is even more limited than it was previously. HTM RV has the potential to pair well with FLASH PT, by performing a range measurement using only a small portion of the fraction dose as a test beam to ensure the dose will be delivered as predicted, and following a positive result with FLASH delivery of the remaining fraction dose. A range measurement using the statistics of the full fraction dose may also be performed afterwards. Due to the significant spike in γ and neutron background rates during a flash treatment, adequate shielding of detectors and electronics during beam delivery would be crucial in this application.

Chapter 7

Summary of Research to Date

In this work, we have proposed a novel technique for in-vivo proton therapy range verification, called HTM RV. The method consists of implanting a Hadron Tumour Marker (HTM) near the planned treatment volume, and measuring the γ-ray signals emitted as a result of activation by the proton beam. These signals are highly correlated with the energy of the beam impinging on the HTM and can provide an absolute measurement of the range of the beam relative to the position of the HTM, which is independent of any uncertainties in beam delivery. In order to determine the viability of this technique and to establish an experimental setup for future work, the Monte Carlo package GEANT4 was used in combination with ROOT to simulate a treatment scenario with the new method outlined in this work. The simulation uses ^{92}Mo as an HTM material, and uses the ^{92}Mo(p,n)^{92}Tc and ^{92}Mo(p,pn)$^{91\mathrm{m}}$Mo reaction channels as a basis for range verification. These simulations showed that the intensity of delayed γ rays produced from these competing reactions yields a precise measurement of the range of the proton beam relative to the marker, with sub-millimetre uncertainty. Following promising simulation results, HTM RV was experimentally demonstrated for the first time. The clinical feasibility of this method was investigated at the proton

therapy facility at TRIUMF with a proof-of-principle experiment which irradiated a naturally-abundant molybdenum foil at various proton beam energies, using the same reactions of interest identified in the simulation. Delayed characteristic γ rays were measured with two Compton-shielded $LaBr_3$ scintillators. The technique was successfully demonstrated by relating the relative intensity of two γ-ray peaks to the energy of the beam at the Mo target, opening the door to future clinical applications where the range of the beam can be verified in real time. A follow-up experiment was performed at TRIUMF, in which three candidate HTM materials (^{nat}Mo, ^{nat}Y, and ^{nat}Zn) were identified and combined into a single composite HTM, which makes use of the strongest reaction in each material. The reaction channels of interest were ^{89}Y(p,n)^{89}Zr, ^{92}Mo(p,n)^{92}Tc, and ^{64}Zn(p,n)^{64}Ga. The setup of the previous experiment was improved on by using High-Purity Germanium (HPGe) detectors to measure the γ-ray signal with a higher resolution than was previously achieved. A PMMA phantom was also used to simulate the γ-ray background from tissue activation. HTM range verification using the data collected in this study yielded range measurements whose average deviation from the expected value was 0.13(22) mm. Finally, the method of HTM RV was successfully extended to heavy-ion therapy in a proof-of-principle experiment with an ^{16}O ion beam and ^{nat}Ag foils as HTMs. The ^{107}Ag(^{16}O,x)^{112}Sb and the ^{107}Ag(^{16}O,x)^{114}Sb reaction channels were identified as suitable for the HTM technique. When only one γ-ray emission is measured, the resulting range-uncertainty estimation is at the 0.5 mm scale. When both channels are considered, a theoretical limit on the range uncertainty of a clinical fidical marker was found to be $\pm$290 µm. Range uncertainty in proton therapy limits the prescribed treatment plan for cancer patients with large safety margins and constrains the direction of the proton beam in relation to any organ at risk. An easy to implement range-verification technique which can be utilized during clinical treatment would allow treatment plans to take full advantage of the sharp fall-off of the Bragg peak without the risk of depositing excessive dose into healthy tissue. HTM RV can be performed in the treatment room, within the time scale of fraction delivery,

avoiding the drawbacks of large time-delays and providing real-time feedback on treatment without relying on complex MC simulations.

Bibliography

[1] E. Kasanda, C. Burbadge, V. Bildstein, J. Turko, A. Spyrou, C. Höhr, and D. Mücher, Phys. Med. Biol. **65**, 245047 (2020).

[2] C. Burbadge, E. Kasanda, V. Bildstein, G. Dublin, B. Olaizola, C. Höhr, and D. Mücher, Phys. Med. Biol. **66**, 025005 (2021).

[3] E. Kasanda, C. Burbadge, V. Bildstein, C. Bélanger-Champagne, H. Behnamian, C. Höhr, and D. Mücher, Phys. Med. Biol. (submitted) (2023).

[4] E. Kasanda, V. Bildstein, D. Hymers, A. Richards, A. Spyrou, C. Höhr, and D. Mücher, Phys. Med. Biol. (submitted) (2023).

[5] J. Ferlay *et al.*, "Global Cancer Observatory: Cancer Today," 2020.

[6] H. Wang *et al.*, The Lancet **388**, 1459 (2016).

[7] Canadian Cancer Statistics Advisory Committee, "Canadian Cancer Statistics 2017," 2017.

[8] M. B. Barton, S. Jacob, J. Shafiq, K. Wong, S. R. Thompson, T. P. Hanna, and G. P. Delaney, Radiother Oncol **112**, 140 (2014).

[9] S. Tyldesley, G. Delaney, F. Foroudi, L. Barbera, M. Kerba, and W. Mackillop, Int. J. Radiat. Oncol. Biol. Phys. **79**, 1507 (2011).

[10] M. Goitein, *Radiation oncology: A physicist's-eye view*Biological and Medical Physics, Biomedical Engineering, 2008 ed. (Springer, New York, NY, 2007).

[11] U. Linz, editor, *Ion beam therapy*Biological and Medical Physics, Biomedical Engineering, 2012 ed. (Springer, Berlin, Germany, 2011).

[12] A.-C. Knopf and A. Lomax, Phys. Med. Biol. **58**, R131 (2013).

[13] S. E. McGowan, N. G. Burnet, and A. J. Lomax, Br J Radiol **86**, 20120288 (2013).

[14] R. R. Wilson, Radiology **47**, 487 (1946) https://doi.org/10.1148/47.5.487, PMID: 20274616.

[15] H. Paganetti, editor, *Proton Therapy Physics* (CRC Press, 2016).

[16] H. Bethe, Annalen der Physik **397**, 325 (1930).

[17] R. C. Miller *et al.*, Semin. Radiat. Oncol. **23**, 127 (2013).

[18] R. Mohan and D. Grosshans, Adv. Drug Deliv. Rev. **109**, 26 (2017).

[19] B. Glimelius *et al.*, Acta Oncol. **44**, 836 (2005).

[20] T. Rackwitz and J. Debus, Seminars in Oncology **46**, 226 (2019).

[21] O. Sokol *et al.*, Physics in Medicine &amp Biology **62**, 7798 (2017).

[22] S. E. McGowan *et al.*, Brit. J. Radiol. **86**, 20120288 (2013).

[23] K. Parodi and J. C. Polf, Med. Phys. **45**, E1036 (2018).

[24] H. Paganetti, Phys. Med. Biol. **57**, R99 (2012).

[25] K. Parodi *et al.*, Int. J. Radiat. Oncol. Biol. Phys. **68**, 920 (2007).

[26] H. Paganetti and G. El Fakhri, Brit. J. Radiol. **88**, 20150173 (2015).

[27] C. Tobias, E. Benton, M. Capp, A. Chatterjee, M. Cruty, and R. Henke, International Journal of Radiation Oncology*Biology*Physics **3**, 35 (1977), Particles and Radiation Therapy Second International Conference.

[28] A.-C. Knopf *et al.*, Int. J. Radiat. Oncol. Biol. Phys. **79**, 297 (2011).

[29] W. Moses, Nucl. Instrum. Methods A **648**, S236 (2011).

[30] P. M. Martins, R. D. Bello, B. Ackermann, S. Brons, G. Hermann, T. Kihm, and J. Seco, Scientific Reports **10** (2020).

[31] C.-H. Min *et al.*, Appl. Phys. Lett. **89**, 183517 (2006).

[32] Y. Xie *et al.*, Int. J. Radiat. Oncol. Biol. Phys. **99**, 210 (2017).

[33] C. Richter *et al.*, Radiother. Oncol. **118**, 232 (2016).

[34] J. M. Verburg and J. Seco, Phys. Med. Biol. **59**, 7089 (2014).

[35] F. Hueso-González *et al.*, Frontiers in Oncology **6**, 80 (2016).

[36] E. Draeger *et al.*, Phys. Med. Biol. **63**, 035019 (2018).

[37] F. Hueso-González, M. Rabe, T. A. Ruggieri, T. Bortfeld, and J. M. Verburg, Physics in Medicine & Biology **63**, 185019 (2018).

[38] D. Hymers *et al.*, Phys. Med. Biol. **66**, 245022 (2021).

[39] S. van de Water, S. Safai, J. M. Schippers, D. C. Weber, and A. J. Lomax, Acta Oncologica **0**, 1 (2019) https://doi.org/10.1080/0284186X.2019.1627416, PMID: 31241377.

[40] OECD NEA Data Bank Report No., , 2012 (unpublished).

[41] W. D. Newhauser *et al.*, Phys. Med. Biol. **52**, 3979 (2007).

[42] Y. K. Lim *et al.*, International Journal of Radiation Oncology∗Biology∗Physics **74**, 1609 (2009).

[43] J. Cho *et al.*, Phys. Med. Biol. **61**, 2162 (2016).

[44] A. Koning and D. Rochman, Nucl. Data Sheets **113**, 2841 (2012).

[45] S. Watanabe, Nucl. Phys A **8**, 484 (1958).

[46] A. J. Koning and J. P. Delaroche, Nucl. Phys A **713**, 231 (2003).

[47] W. Dilg *et al.*, Nucl. Phys A **217**, 269 (1973).

[48] J. Kopecky and M. Uhl, Phys. Rev. C **41**, 1941 (1990).

[49] E. Lamere *et al.*, Physical Review C **100** (2019).

[50] C. M. Baglin, Nucl. Data Sheets **113**, 2187 (2012), Data extracted from the ENSDF database (2019-08-15).

[51] C. M. Baglin, Nucl. Data Sheets **114**, 1293 (2013), Data extracted from the ENSDF database (2019-08-15).

[52] D. Salehi, D. Sardari, and M. S. Jozani, Journal of Radiation Research and Applied Sciences **8**, 439 (2015).

[53] R. Biswas, H. Sahadath, A. S. Mollah, and M. F. Huq, Journal of Radiation Research and Applied Sciences **9**, 26 (2016).

[54] K. Szymańska *et al.*, Nucl. Instrum. Methods A **592**, 486 (2008).

[55] S. Agostinelli *et al.*, Nuclear Instruments and Methods in Physics Research Section A: Accelerators, Spectrometers, Detectors and Associated Equipment **506**, 250 (2002).

[56] A. Lourenço *et al.*, **62**, 3883 (2017).

[57] Z. Wang *et al.*, Int J Clin Exp Pathol **7**, 6985 (2014).

[58] R. Brun and F. Rademakers, "ROOT - An Object Oriented Data Analysis Framework," in *AIHENP'96 Workshop, Lausane* volume 389 pp. 81–6 1996.

[59] Geant4 Collaboration, "Geant4 Physics List Guide," 2018.

[60] Ametek Advanced Measurement Technology Report No., , 2003 (unpublished).

[61] D. M. Martinez *et al.*, Sci. Rep. **9**, 17599 (2019).

[62] J. Y. Huang *et al.*, Phys. Med. Biol. **56**, 5287 (2011).

[63] J. Cheung *et al.*, Phys. Med. Biol. **55**, 7135 (2010).

[64] A. Giebeler *et al.*, J. Appl. Clin. Med. Phys. **10**, 2875 (2009).

[65] D. Habermehl *et al.*, J. Radiat. Res. **54**, i61 (2013).

[66] J. Saini *et al.*, Biomed. Phys. Eng. Express. **3**, 027003 (2017).

[67] E. Tran *et al.*, Int. J. Radiat. Oncol. Biol. Phys. **83**, 1425 (2012).

[68] M. Uddin *et al.*, Appl. Radiat. Isotopes **60**, 911 (2004).

[69] M. S. Uddin and M. Baba, Appl. Radiat. Isotopes **66**, 208 (2008).

[70] S. Takács *et al.*, Nucl. Instrum. Methods B **198**, 183 (2002).

[71] M. Khandaker *et al.*, Nucl. Instrum. Methods B **262**, 171 (2007).

[72] A. A. Alharbi *et al.*, Radiochim. Acta **99**, 763 (2011).

[73] J. K. Tuli, "Nuclear Wallet Cards. 8th Edition, National Nuclear Data Center,", https://www.nndc.bnl.gov/wallet/wall47.pdf Brookhaven National Laboratory, New York 2011.

[74] I. Bylinskii and M. Craddock, Hyperfine Interact. **225**, 9 (2014).

[75] E. W. Blackmore, "Operation of the TRIUMF (20-500 MeV) proton irradiation facility," in *IEEE Radiation Effects Data Workshop* pp. 1–5 2000.

[76] J. F. Ziegler *et al.*, Nucl. Instrum. Methods B **268**, 1818 (2010).

[77] S. Ritt and P. Amaudruz, "The MIDAS Data Acquisition System," in *Proc. 10th IEEE Real Time Conf.* p. 309 1997.

[78] P. C. Bender, "GRSISort,", https://github.com/GRIFFINCollaboration/GRSISort/wiki 2019.

[79] J. Theuerkauf *et al.*, "Program Tv,", Institute for Nuclear Physics, Cologne 1993.

[80] Saint-Gobain, "BrilLanCe 380 Data Sheet,", https://www.crystals.saint-gobain.com/ 2012.

[81] A. Knopf *et al.*, Med. Phys. **35**, 2918 (2008).

[82] F. Hueso-González *et al.*, Phys. Med. Biol. **63**, 185019 (2018).

[83] Gavron A, Phys. Rev.C21 (1980).

[84] Tarasov, O.B.and Bazin, D, NIM B **266** (2008).

[85] Kinsey, R et al., "The NUDAT/PCNUDAT Program for Nuclear Data,", "paper submitted to the 9th International Symposium of Capture Gamma-Ray Spectroscopy and Related Topics, Budapest, Hungary, October 1996. Data extracted from the NUDAT database, version 2.8 (March 2020)" 1996.

[86] A. Sonzogni, "NNDC Chart of Nuclides," in *ND2007* EDP Sciences 2007.

[87] A. Garnsworthy *et al.*, Nuclear Instruments and Methods in Physics Research Section A: Accelerators, Spectrometers, Detectors and Associated Equipment **853**, 85 (2017).

[88] E. Blackmore, B. Evans, and M. Mouat, "Operation of the TRIUMF Proton Therapy Facility," in *Proceedings of the 1997 Particle Accelerator Conference (Cat. No.97CH36167)* volume 3 pp. 3831–3833 1997.

[89] T. Tessonnier, A. Mairani, S. Brons, T. Haberer, J. Debus, and K. Parodi, Phys. Med. Biol. **62**, 3958 (2017).

[90] R. Ladbury *et al.*, IEEE Trans. Nucl. Sci. **51**, 3664 (2004), Conference Name: IEEE Transactions on Nuclear Science.

[91] A. Gade and B. M. Sherrill, Phys. Scr. **91**, 053003 (2016).

[92] O. B. Tarasov and D. Bazin, Nucl. Instrum. Meth. B **376**, 185 (2016).

[93] "SRIM-2013 - The Stopping and Range of Ions in Matter,", http://www.srim.org/.

[94] K. Ohta *et al.*, CardioVasc. Interv. Radiol. **38**, 1288 (2015).

[95] C. Onal, editor, *Prostate Cancer* (IntechOpen, 2018).

[96] C. Bergom *et al.*, Frontiers in Oncology **8**, 87 (2018).

[97] M.-C. Vozenin, J. Bourhis, and M. Durante, Nature Reviews Clinical Oncology **19**, 791 (2022).

[98] A. E. Mascia *et al.*, JAMA Oncology (2022).

[99] U. A. Weber, E. Scifoni, and M. Durante, Medical Physics **49**, 1974 (2021).